Draft Manuscript for Review

Petrogenesis and assembly of the Don Manuel igneous complex, Miocene-Pliocene porphyry copper belt, Central Chile

Journal:	*Journal of Petrology*
Manuscript ID	Draft
Manuscript Type:	Original Manuscript
Date Submitted by the Author:	n/a
Complete List of Authors:	Gilmer, Amy; University of Bristol, School of Earth Sciences Sparks, R. S.; University of Bristol, School of Earth Sciences Blundy, Jon; University Of Bristol, School of Earth Sciences Rust, Alison; University of Bristol, School of Earth Sciences Hauff, Folkmar; Helmholtz-Zentrum fur Ozeanforschung Kiel Hoernle, Kaj; Helmholtz-Zentrum fur Ozeanforschung Kiel Spencer, Christopher; NERC Isotope Geosciences Facilities, British Geologic Survey; Curtain University, The Institute of Geoscience Research, Department of Applied Geology Tapster, Simon; NERC Isotope Geosciences Facilities, British Geologic Survey
Keyword:	Arc magmatism, magma mixing, porphyry copper deposit, magma-mush system, polybaric differentiation

Petrogenesis and assembly of the Don Manuel igneous complex, Miocene-Pliocene porphyry copper belt, Central Chile

Amy K. Gilmer[1*], R. Stephen J. Sparks [1], Jon D. Blundy[1], Alison C. Rust[1], Folkmar Hauff[2], Kaj Hoernle[2], Christopher J. Spencer[3,4], and Simon Tapster[3]

[1]*School of Earth Sciences, University of Bristol, Wills Memorial Building, Bristol, BS8 1RJ UK*

[2]*GEOMAR Helmholtz Centre for Ocean Research Kiel, 24148 Kiel, Germany*

[3]*NERC Isotope Geosciences Facilities, British Geological Survey, Keyworth, Nottingham, NG12 5GG*

[4]*The Institute of Geoscience Research, Department of Applied Geology, Curtin University, Perth, Australia*

***Corresponding author**. Email: agilmer@usgs.gov*

ABSTRACT

The 4.0-3.6 Ma Don Manuel igneous complex (DMIC), central Chile, provides a window into igneous processes involved in magma genesis associated with porphyry copper-style mineralization. This study uses petrographic, petrologic, geochemical and isotopic data to examine the evolution of magmas from the mid- to lower-crustal source region to shallow emplacement. The data provide evidence of progressive oxidation of magma during differentiation and ascent, fractionation of Cl from S through degassing, and the late-stage, near-solidus removal of Cl from the system. Magmas of basaltic andesite to rhyolite composition were produced by polybaric differentiation of hydrous parental mafic magmas. Variations in crustal differentiation depths led to variable suppression of plagioclase saturation that is recorded in distinctive strontium-anorthite evolution patterns. Hydrous, derivative magmas generated over a wide range of pressures were episodically emplaced into the shallow crust at depths between 3.5 and 5 km. Intermediate porphyry dikes closely associated with copper mineralization contain diverse crystal cargoes indicating significant igneous mixing. These crystal cargoes represent samples of crystal mush entrained from different depths, as well as crystals originating in different magmas and crystals grown in-situ from hybridized magmas. Mafic enclaves, containing plagioclase and amphibole compositions that match those of the basaltic andesites, occur within biotite tonalite testifying to magma mingling during ascent. Sulfur and chlorine contents of apatite within the different DMIC units record variable degassing and decoupling of volatile components with sulfur showing variations of three orders of magnitude compared with one order of magnitude for chlorine. The hypabyssal nature of the DMIC affords a detailed, integrated record of magmatic differentiation processes occurring within trans-crustal magmatic systems of the sort thought to characterize many crustal arc settings and play a fundamental role in driving porphyry-style copper mineralization.

KEY WORDS: Arc magmatism; magma mixing; porphyry copper deposit; magma-mush system; polybaric differentiation

INTRODUCTION

The Miocene-Pliocene porphyry copper belt of the Chilean Andes hosts some of the world's largest porphyry copper-molybdenum deposits. The silicic, calc-alkaline magmas associated with porphyry-type mineralization in subduction settings are generally acknowledged to be oxidized and hydrous (Candela & Piccoli, 2005; Loucks, 2014; Richards, 2011; Seedorff *et al.*, 2005; Sillitoe, 2010). Crustal processes including the role of water during differentiation, the effects of the oxidation state of the magma, and the source of the metals and sulfur required for mineralization have been the focus of recent research (Blundy *et al.*, 2015; Nadeau *et al.*, 2010, 2016, Richards, 2016, 2011; Tattitch & Blundy, 2017). Equally important to understanding mineralization is how associated intrusions are assembled and how they relate to deeper regions of the magmatic system. Understanding the igneous processes that shape the magmatic systems hosting these deposits may be key to distinguishing what makes one system mineralized while another remains barren. Igneous processes can be, however, difficult to investigate due to the pervasive and destructive alteration commonly associated with mineralization.

The term "porphyry" for hypabyssal intrusions associated with these large copper deposits derives from the presence of larger crystals in a finer-grained groundmass. Porphyritic texture is commonly attributed to a two-stage crystallization history whereby phenocrysts grow slowly in a magma body with subsequent rapid groundmass crystallization driven by decompression or cooling. However, much of the crystal content in intermediate igneous rocks is commonly the product of igneous mixing, a term used here for the spectrum of mixing processes where one or more magmas are combined physically. This mixing has been widely documented in many arc magmatic systems and may include magma mixing (hybridization), magma mingling (Clynne, 1999; Humphreys *et al.*, 2009; Murphy *et al.*, 1998; Pallister *et al.*, 1996; Tepley III *et al.*, 2000) & interactions of magma with igneous mushes, cumulates and restite. These processes are significant in the petrogenesis of intermediate magmas as true liquids of andesitic composition are uncommon (Melekhova *et al.*, 2013; Reubi & Blundy, 2009), and thus a mixing origin has been proposed by many (e.g. Clynne, 1999; Dungan & Davidson, 2004;

Eichelberger, 1975; Hildreth & Moorbath, 1988; Özdemir *et al.*, 2011; Reubi & Blundy, 2009; Portnyagin *et al.*, 2015).The crystal cargo in porphyritic rocks commonly consists of entrained solids or antecrysts (Annen *et al.*, 2005; Bergantz *et al.*, 2015; Charlier *et al.*, 2004; Cooper & Reid, 2003; Davidson *et al.*, 2005, 2007; Dungan & Davidson, 2004; Gill *et al.*, 2006; Hildreth & Wilson, 2007; Jerram & Martin, 2008; Zhang *et al.*, 2015), possibly including remobilized cumulate crystals picked up during ascent of melts through the trans-crustal mush. Antecrysts are crystals that did not crystallize directly from the magma in which they are hosted, but were grown within ancestral magmas from the same system (Charlier *et al.*, 2004; Gill *et al.*, 2006; Hildreth & Wilson, 2007; Jerram & Martin, 2008). Xenocrysts, by contrast, are crystals entrained from unrelated, older magmatic systems (Streck *et al.*, 2007). Thus many phenocrysts are actually antecrysts, or possibly xenocrysts. Note that neither antecrysts nor xenocrysts need be in equilibrium with the groundmass that surrounds them.

An emerging concept in igneous petrology envisages trans-crustal magmatic systems (Cashman *et al.*, 2017; Christopher *et al.*, 2015; Edmonds *et al.*, 2016; Sparks & Cashman, 2017) consisting of multiple magma bodies embedded in low melt-fraction magmatic mush (Annen *et al.*, 2015; Bachmann & Bergantz, 2006; Bergantz *et al.*, 2015; Cashman & Giordano, 2014; Hildreth, 2004) that extends throughout the crust and even into the upper mantle. In many ways this concept is complementary to the interpretation of porphyritic volcanic and hypabyssal rocks being mixtures of crystals and melts derived from different parts of such a large-scale trans-crustal igneous system (Annen *et al.*, 2015; Christopher *et al.*, 2015; Hildreth & Moorbath, 1988; Solano *et al.*, 2012, 2014). The implications of these concepts for the relationship of igneous processes to associated mineralization have yet to be fully explored.

In this paper, we present the detailed petrology of the Pliocene Don Manuel igneous complex (DMIC) associated with porphyry copper mineralization in central Chile. Our study offers a look at an arc magmatic system from the hypabyssal perspective. Commonly studies of arc magmatic systems are either centered on extrusive (volcanic) products or on intrusions (plutons or batholiths) associated with larger magma reservoirs. By examining the hypabyssal rocks, we provide insight into the processes that

may affect porphyry-type ore formation, but also into what is sampled from the trans-crustal magmatic system and subsequently emplaced into the subvolcanic system, but not erupted. We use petrographic observations, whole rock and mineral chemistries, as well as isotopic compositions to constrain storage conditions and pathways, and provide insight into the evolution of the magma reservoirs that generated the DMIC.

GEOLOGICAL BACKGROUND

Regional Geology

The Don Manuel igneous complex (DMIC) and associated porphyry copper system are located in central Chile in the Cordillera Principal of the Andes (Fig. 1), approximately 25 km east of the giant El Teniente porphyry copper-molybdenum deposit and 20 km southwest from Maípo volcano within the northern Southern Volcanic Zone (NSVZ) (33°S -34.5°S). The study area is just south of the Chilean-Pampean flat slab segment (28°S-33°S) (Kay *et al.*, 2005; Marot *et al.*, 2014; Stern & Skewes, 1995), where the Nazca plate is subducting below the South American plate at an angle of ~10° (Farías *et al.*, 2010; Marot *et al.*, 2014; Pardo *et al.*, 2002; Stern, 2004; Yáñez *et al.*, 2002). At the latitude of the DMIC, the subducted slab lies at ~120 km depth with a dip angle of ~27° (Nacif *et al.*, 2015; Pardo *et al.*, 2002).

Like El Teniente, the Don Manuel porphyry copper system is part of the Miocene-Pliocene Porphyry Copper-Molybdenum belt. This belt includes the Río Blanco-Los Bronces and Los Pelambres-El Pachón deposits which, along with El Teniente, are some of the largest porphyry copper deposits in the world. These three deposits are aligned roughly N-S in the central part of Western Cordillera Principal, whereas Don Manuel lies farther east (Fig. 1a), along the boundary of the Western and Eastern Cordillera Principal near the Chile-Argentina border (Gilmer *et al.*, 2017).

Subduction along the western margin of the South American plate has been ongoing since the Jurassic (Mpodozis *et al.*, 1990). Flattening of the Nazca plate is thought to have begun in the early

Miocene (~18 Ma) with the onset of subduction of the Juan Fernandez Ridge (JFR) (Yáñez *et al.*, 2002, 2001). Magmatism in the flat-slab segment ceased ~10 Ma (Kay *et al.*, 2005). Accelerated convergence from plate reconfiguration and the subduction of the JFR, as well as subsequent flat-slab subduction, have resulted in increased compression. These events also led to the inversion of structures related to late Eocene to late Oligocene extension, such as the Abanico Basin (Farías *et al.*, 2010; Giambiagi *et al.*, 2003a, 2003b; Giambiagi & Ramos, 2002; Godoy *et al.*, 1999; Ramos *et al.*, 2004), and to crustal thickening and development of the Aconcagua Fold and Thrust Belt (Giambiagi *et al.*, 2003a, 2003b; Giambiagi & Ramos, 2002; Godoy *et al.*, 1999). Increased crustal thickening from ~30 km to ~50 km is reflected in the geochemistry of intrusive and volcanic units in the region (Kay *et al.*, 1991, 2005).

Cenozoic arc magmatism in the region began with the eruption and deposition of the Oligocene to early Miocene Abanico Formation, which is equivalent to the Coya Machali Formation in the study area (Charrier *et al.*, 1996, 2002) into which the DMIC was emplaced (Fig. 1b). This formation consists of tholeiitic basaltic andesite and andesite, ignimbrite, volcaniclastics and lacustrine sediments (Charrier *et al.*, 1996, 2002; Godoy *et al.*, 1999; Kay *et al.*, 2005) that were deposited in the Abanico/Coya Machali extensional basin. During basin inversion between 21 and 15 Ma, the volcanics of the Miocene Farellones Formation were deposited unconformably on top of the Abanico/Coya Machali Formation (Charrier *et al.*, 2002; Kay *et al.*, 2005; Vergara *et al.*, 1988). The main axis of the volcanic arc migrated eastwards during the Late Miocene and Pliocene as a result of the shallowing of the subducting Nazca plate (Kay *et al.*, 2005; Stern, 2004; Stern & Skewes, 1995). Arc migration was associated with geographical broadening of the volcanic belt with magmas becoming increasingly calc-alkaline (Kay *et al.*, 2005, Kay & Mpodozis, 2001).

Structurally, the DMIC and associated porphyry copper system were emplaced in a compressive tectonic regime on the eastern edge of the inverted Coya Machalí extensional basin along the reactivated El Fierro fault system (Fig.1a), a major décollement surface (Farías *et al.*, 2010; Godoy *et al.*, 1999). This north-striking, high-angle fault system has been interpreted to mark the eastern margin of the Coya

Machalí/Abanico extensional/transtensional basin (Charrier *et al.*, 2002; Farías *et al.*, 2010; Godoy *et al.*, 1999).

Don Manuel Igneous Complex

The DMIC formed through a series of episodic intrusive pulses from ~4.0 to 3.6 Ma and consists of six intrusive units described in detail in Gilmer *et al.* (2017). Four of these units occur in the Don Manuel Principal (DMP) area and two crop out in the Paredones area (Fig. 1b; Table 1). The DMIC, along with the Coya Machalí Formation into which it was emplaced, hosts porphyry-style copper and molybdenum mineralization. Magmatic activity began at ca. 4.0 Ma with the emplacement of quartz monzonite dikes in the DMP area. Magmatism shifted a few km to the north about 95 kyrs later, when the Paredones rhyolitic stock was emplaced. The quartz monzonite and rhyolite have similar compositions (Fig. 2 and Fig. 3). Following a lull of ~50 kyr, an equigranular biotite tonalite intruded in the DMP area. Another compositionally similar, but texturally distinct and less extensive, pulse of porphyritic biotite tonalite followed ~100 kyr later. At ~3.73 Ma the DMIC was intruded by a series of intermediate porphyry dikes ranging in composition from dacite to andesite and displaying disequilibrium textures, variable phenocryst assemblages and a wide array of phenocryst compositions (Table 1). The dikes are the principal hosts of mineralization. The most mafic units in the DMIC are two types of basaltic andesite dikes: hornblende basaltic andesite dikes that cross cut the units in the DMP area; and clinopyroxene-bearing basaltic andesite dikes which crop out in the Paredones area. Two of the hornblende basaltic andesite dikes have been dated by $^{40}Ar/^{39}Ar$ at 3.85 ± 0.19 Ma and 3.60 ± 0.06 Ma (Gilmer *et al.*, 2017). The Paredones clinopyroxene-bearing basaltic andesite dikes have not been dated. The presence of mafic enclaves in the rhyolite, biotite tonalite and intermediate porphyry dikes, as well as late mafic dikes cross-cutting DMP lithologies, testify to episodic emplacement of mafic magma.

SAMPLES AND ANALYTICAL TECHNIQUES

Alteration associated with the DMIC and porphyry copper system is localized and heterogeneous, making it possible to identify primary igneous textures and compositions through careful sampling. K-silicate alteration is the prevalent alteration style in the DMIC, which may have enriched the rocks in alkalis. Samples chosen for this study were selected from the least altered intervals and come from eight drill cores and from field outcrops in the Paredones area (Gilmer *et al.*, 2017). Samples were examined petrographically using transmitted and reflected light, as well as by scanning electron microscopy (SEM) at the University of Bristol. Modal analysis was completed on only the freshest samples from each unit (Table 1). Where minor alteration was encountered primary mineralogy was interpreted and counted.

Radiogenic isotopes

Sr, Nd and Pb isotope ratios of whole rock samples were determined by thermal ionization mass spectrometry (TIMS) at GEOMAR in Kiel, Germany. Sample powders were leached in 2 N HCl at 70°C for one hour and repeatedly rinsed in 18.2 MΩ/cm H_2O prior to digestion in a hot HF:HNO_3 mixture at 150°C over 48 hours. Chromatography followed routine methods described in Hoernle *et al.* (2008). Pb isotope ratios were measured on a Finnigan MAT262 RPQ2+ in static multi-collection and mass bias correction used the ^{207}Pb-^{204}Pb double spike (DS) technique of Hoernle *et al.* (2011). DS corrected NBS981 values (n=17) and associated 2σ external errors (2SD) yielded $^{206}Pb/^{204}Pb = 16.9427 \pm 0.0021$, $^{207}Pb/^{204}Pb = 15.5005 \pm 0.0021$, $^{208}Pb/^{204}Pb = 36.7278 \pm 0.0064$, $^{207}Pb/^{206}Pb = 0.914877 \pm 0.000032$ and $^{208}Pb/^{206}Pb = 2.167765 \pm 0.000063$ over the period the sample data was generated. Sr and Nd isotopic ratios were measured on a Thermo Scientific TRITON Plus in static multi-collection mode and $^{86}Sr/^{88}Sr = 0.1194$ and $^{146}Nd/^{144}Nd = 0.7219$ applied for within-run mass bias correction. Sample data are reported relative to the standards NBS987 with $^{87}Sr/^{86}Sr = 0.710250 \pm 0.000009$ (2SD, n = 102) and La Jolla with $^{143}Nd/^{144}Nd = 0.511850 \pm 0.000006$ (2SD; n = 114) obtained on the instrument since its 2014 installation. Replicate Sr and Nd analyses by means of a separate digest of basaltic andesite sample

DM5AG07 were reproduced within 2SD obtained for the above-mentioned standards for Sr and Nd but very slightly outside 2SD for Pb.

Hf isotope analyses were conducted on zircon from the DMIC using the zircon dissolution washes from the ID-TIMS U-Pb dating (see Gilmer *et al.*, 2017) at the NERC Isotope Geosciences Facilities of the British Geological Survey in Keyworth, UK. Analytical methods are presented in Supplementary Materials S13.

Electron microprobe analysis

Plagioclase, amphibole, pyroxene, biotite, and Fe-Ti oxide compositions were analyzed on a five-spectrometer Cameca SX-100 electron microprobe at the University of Bristol calibrated against a range of mineral, oxide, and metal standards. Silicate analyses were run at 20 KeV with a focused 10 nA beam. Strontium in plagioclase was measured with a 100 nA beam for 200s. Counting times for most elements were 30s on peak and 15s on the background. Sodium mobility was not observed when Na was measured first. Minor and trace elements in plagioclase were analyzed using counting times of 40-200s for Ba, 90-150s for Fe, and 50-300s for Mg. A diopside standard and amphibole standard were run three times as unknowns at the beginning of each session. The results for these analyses are presented in Supplementary data.

Apatite electron microprobe analysis

Apatites from twelve samples were analyzed using the JEOL JXA8530F field emission gun electron microprobe at University of Bristol operating at 15 KeV, 10 nA, and utilizing a 10 µm and 5 µm spot size. Counting times were as follows: for Ca, Fe, and P were 10s on peak and 5s on the background; for Na, Si, F 30s on peak, 15s on background; for Nd, La, and Y 40s on peak, 20s on background; and for S, Mn, and Ce 60s on peak and 30s on background. Durango apatite standard was analyzed three times as an unknown at the beginning and end of each session.

ICP-MS zircon trace element analysis

Trace element and REE data were acquired for zircon separates from twelve samples using a New Wave Research 20 UP193-FX 193 nm ArF excimer laser on an Agilent 7500 series mass spectrometer at the NIGL of the British Geological Survey in Keyworth, UK. Prior to analysis, zircons were imaged using a Cathodoluminescence (CL) detector and SEM in order to assess internal zoning. Zircons were ablated at 65% laser power with a repetition rate of 5 Hz and a 30 s dwell time. Data were processed with the Iolite software package. A 30 µm analytical spot size was used, making it difficult to avoid inclusions in some cases. REE detection limits are in the vicinity of 0.01 ppm for analysis spots that are 30 µm across and a few microns deep. Results were screened to remove analyses that contained apatite and/or Fe-Ti oxide inclusions by monitoring P, Ti, and LREEs. Two glass standards, NIST-610 and NIST-612, and a zircon standard 91500 were analyzed at the beginning and end for each session; 91500 was also analyzed between each sample separate.

RESULTS

Whole Rock Chemistry and Radiogenic Isotopes

The DMIC constitutes a typical calc-alkaline suite with 53 to 74 wt. % SiO_2 (Fig. 2). Whole rock compositions for the DMIC are presented in Gilmer *et al.* (2017). Variation diagrams for major elements show that the rocks of the DMIC approximate linear trends similar to the Miocene to Pliocene shallow intrusions of the nearby El Teniente porphyry copper system and the Pleistocene volcanics of Maipo (Fig. 2 and Fig. 3) (Sruoga *et al.*, 2005, 2012; Stern *et al.*, 2011b).

Whole rock $^{87}Sr/^{86}Sr$ and $^{143}Nd/^{144}Nd$ isotopic compositions range between 0.7039 – 0.7045 and 0.51264 – 0.51280 (εNd = +0.1 to +3.1) respectively (Table 2; Fig. 4; Supplementary Materials Table S1). The lowest $^{87}Sr/^{86}Sr$ and highest $^{143}Nd/^{144}Nd$ ratios for DMIC samples correspond to three basaltic andesite dikes, one from the Paredones area and two from the DMP drill core. The other samples from DMIC form a tight cluster at higher $^{87}Sr/^{86}Sr$ and lower $^{143}Nd/^{144}Nd$. Together with previous data and

from other nearby intrusive complexes and volcanic centers (Hildreth & Moorbath, 1988; Holm *et al.*, 2014; Kay *et al.*, 2005; Kurtz *et al.*, 1997; Muñoz *et al.*, 2006; Nyström *et al.*, 2003; Skewes & Stern, 1995; Stern *et al.*, 2011a, 2011b) the DMIC data are consistent with a broad regional temporal trend of increasing $^{87}Sr/^{86}Sr$ and decreasing $^{143}Nd/^{144}Nd$.

$^{207}Pb/^{204}Pb$ and $^{206}Pb/^{204}Pb$ compositions for the DMIC units have a positive correlation and range from 15.6026-15.6262 and 18.5692-18.6631, respectively (Table 2; Supplementary Materials Table S1). The samples from the two field areas group together with the Paredones rhyolite and basaltic andesite having lower ratios. Further assessment of the Pb isotopic data is not discussed in this paper, but the data is provided for completeness.

Initial εHf values of zircon washes range from -0.3 (±0.3) to 2.8 (±0.7) (2SD; Table 3; Fig. 5). Within the DMIC there is no correlation of initial εHf values with SiO_2 (Supplementary Materials Table S2, Fig. 5). The three inherited zircons with ages ca. 8 Ma have initial εHf values within the range of the other DMIC zircons. These values are similar to those of Miocene-Pliocene intrusions in the eastern Principal Cordillera (Fig. 1a), such as Cerro Catedral, Cruz de Piedra, Jeria, and Río Negro (Fig. 5) (Muñoz *et al.*, 2013). However, they are much more enriched than the initial εHf values for El Teniente intrusions, intrusive units near Río Blanco-Los Bronces, and other western Principal Cordillera Oligocene-Miocene intrusions and volcanics (Deckart *et al.*, 2010; Montecinos *et al.*, 2008; Munoz *et al.*, 2012; Muñoz *et al.*, 2013).

Petrography and Mineral Compositions

Petrographic features of each of the DMIC units are summarized in Table 1 of Gilmer *et al.* (2017). The quartz monzonite is fine- to medium-grained and composed of plagioclase, microcline, quartz, and minor biotite with accessory apatite, anhydrite, magnetite, rutile, and zircon. Both equigranular and porphyritic biotite tonalites contain subhedral to anhedral plagioclase, tabular biotite, microcline, quartz,

± amphibole. Accessory phases include apatite, magnetite, ilmenite, titanite, and zircon. Anhydrite inclusions are observed in plagioclase in both variants of biotite tonalite.

The intermediate porphyry dikes (IPD) range in composition from andesite to dacite and have diverse phenocryst assemblages and textures, including abundant glomerocrysts and crystal clots that consist predominantly of plagioclase ± biotite and amphibole. The IPD are subdivided into three groups based on their mafic phenocryst content. IPD1 contain biotite phenocrysts; IPD2 contain both biotite and amphibole phenocrysts; and IPD3 contain amphibole phenocrysts. There is overlap in bulk rock SiO_2 among the three groups, but most IPD3s have lower SiO_2 content (Fig. 2). No definitive cross-cutting relationships were observed in the drill cores among the three IPD types. Accessory phases in the IPDs include quartz, apatite, magnetite, ilmenite, titanite, and zircon. Anhydrite inclusions in plagioclase were observed in all three IPD types. Andesitic mafic enclaves are common and the main mineralization and hydrothermal alterations are associated with the three types of IPD (Gilmer *et al.*, 2017).

Within the drill core, the aforementioned units are intruded by numerous aphanitic to porphyritic basaltic andesite dikes containing phenocrysts of plagioclase and amphibole with accessory magnetite, ilmenite and apatite. The dikes contain occasional crystal clots and gabbroic xenoliths that consist of interlocking amphibole and plagioclase with inclusions of magnetite.

The porphyritic Paredones rhyolite stock, exposed north of the DMP area (Fig. 1b) contains phenocrysts of plagioclase, biotite, and occasional quartz “eyes”. Porphyritic basaltic andesite dikes in the Paredones area contain phenocrysts of plagioclase and clinopyroxene with minor amphibole, magnetite and ilmenite.

Plagioclase

Plagioclase is the most abundant phenocryst and groundmass phase in all units of the DMIC. Examples of DMIC plagioclase phenocrysts[1] are shown in Fig. 6. Five different groups of phenocrysts have been recognized in the IPDs based on optical, SEM and electron microprobe analyses (Table 4) (Gilmer *et al.*, 2017) and Supplementary Materials Table S3. These include: (1) reversely zoned phenocrysts with broad cores separated from sieve-textured rims by sharp intermediate transitions; (2) oscillatory-zoned phenocrysts with high-amplitude, high-frequency variations in An content; (3) patchy-zoned phenocrysts containing anorthite-rich cores showing significant resorption and infilled with later albitic domains; (4) largely unzoned, euhedral grains; and (5) patchy zoned phenocrysts, commonly in glomerocrysts. The assemblage of multiple populations of plagioclase phenocrysts with complex zoning, commonly recognized in a single thin section, testifies to conspicuous hybridization and magma mixing (Gilmer *et al.*, 2017). The plagioclase phenocrysts within the quartz monzonite, rhyolite, biotite tonalite, and the two types of basaltic andesite contain uniform, normal- or oscillatory-zoned phenocryst populations.

Fig. 6g summarizes the anorthite compositional ranges of plagioclase cores, rims, and microphenocrysts in each of the DMIC units. In general, the most silicic units in the DMIC have the most albitic plagioclase and the most mafic units the most anorthitic plagioclase (Fig. 6g). The rhyolite, quartz monzonite, DMP basaltic andesite, Paredones basaltic andesite, and, to a certain extent, the biotite tonalite show the expected progression of decreasing anorthite content from cores to rims to microphenocrysts. By contrast, IPD plagioclase compositions range widely by location and show no overall decrease in An content from cores to rims to microphenocryts. Plagioclase phenocrysts in IPD1 and IPD2 have similar An ranges for cores, rims and microphenocrysts. In comparison plagioclases from IPD3 contain more calcic cores and microphenocrysts (Fig.6g).

[1] "Phenocryst" is used in a non-genetic sense to denote any crystal larger than 0.5 mm set in a finer grained groundmass. Phenocrysts may have been directly crystallized from their host magma, transferred from other magmas upon mixing or sourced from disrupted crystal mush or cumulates.

Sr concentrations in plagioclase

The trace element content of igneous plagioclases reflects the trace element content of the melt from which they grew, the plagioclase-melt partition coefficient at those conditions, and the extent of any subsequent diffusive re-equilibration during cooling, (Blundy & Shimizu, 1991; Dohmen & Blundy, 2014; Ginibre & Wörner, 2007). DMIC plagioclases span a wide range in Sr content, with the maximum Sr (3000 ppm) observed at around An_{50}. Two distinct trends in Sr versus An concentrations are observed (Fig. 7a). Plagioclase in the silicic units (quartz monzonite, biotite tonalite and rhyolite) defines a trend of decreasing Sr with decreasing An concentration below An_{50}, whereas plagioclases in the more mafic units (DMP and Paredones basaltic andesite dikes, mafic enclaves, and gabbroic xenolith) define a trend of relatively uniform Sr with decreasing An concentration (Fig. 7a). Similar high Sr and low Sr plagioclase phenocryst assemblages have been observed at Parinacota volcano in northern Chile and at Mount Mazama in Oregon (Druitt & Bacon, 1989; Ginibre *et al.*, 2002; Ginibre & Wörner, 2007).

The IPD plagioclases demonstrate significantly more variability (Fig. 7b), effectively filling the gap between the two trends described above (Fig. 7a). IPD1 plagioclases, like the rhyolite, quartz monzonite and biotite tonalite, generally plot along the trend of decreasing Sr concentration with decreasing An content. IPD2 plagioclases also show an overall similar but scattered trend. Sr contents are highly variable (1000-4000 ppm) again with a maximum near An_{50}. There is some clustering into high and low Sr populations. The majority of the IPD3 plagioclases overlap the lower IPD2 Sr cluster but extend to higher An.

Biotite

Both primary (magmatic) and secondary (hydrothermal) biotite occur in DMIC units. Primary biotite is present in rhyolite, quartz monzonite, biotite tonalite, and in IPD1 and IPD2. Euhedral to subhedral, phenocrysts and microphenocrysts are light to dark brown in color (Fig. 8a). By contrast, light brown to green hydrothermal biotite occurs as fine-grained aggregates ("shreddy biotite") replacing amphibole or

primary biotite, and occurring as disseminated clots (Fig. 8b). Primary biotite phenocrysts commonly contain inclusions of plagioclase, Fe-Ti oxides, rutile needles, sulfides, and apatite.

Representative analyses of primary and secondary biotite are presented in Table 5 with further analyses in Supplementary Data Table S4. Biotites that showed significant alteration, including frayed edges, hydrothermal biotite replacement, and chloritization, were not analyzed. There is considerable scatter and overlap in biotite compositions (Fig. 8). IPD1 has notably higher Mg-number (Fig. 8c) and IPD2 shows high and low-Cl content clusters (Fig. 8e). Secondary biotites are mostly lower in Ti than primary biotites and also show high and low-Cl populations (Fig. 8d and Fig. 8f).

Clinopyroxene

Calcic augite phenocrysts within the Paredones basaltic andesite dikes are euhedral to subhedral and commonly contain plagioclase inclusions (Fig. 9a) or may have a poikilitic texture. Representative compositions are summarized in Table 6 with additional analyses available in Supplementary Data Table S5. Compositions are uniform ($En_{43}Wo_{42}Fs_{15}$) with Mg-number ranging from 70 to 76.

Amphibole

Amphibole phenocrysts are present in the DMP and Paredones basaltic andesite dikes, the IPD suite (IPD2 and IPD3), mafic enclaves, gabbroic xenolith and the equigranular and porphyritic biotite tonalite (Fig. 9b, c, d). Amphibole phenocrysts in IPD2 and IPD3 are subhedral to euhedral, occasionally prismatic and make up 25-45% of phenocrysts with a size range from 0.04 to 2 mm (Fig. 9c). Amphibole (3 to 5% of the mode) in the biotite tonalite occurs mainly in the porphyritic phase as phenocrysts (1-4 mm) (Fig. 9d). Amphibole occurs as euhedral to subhedral phenocrysts (0.13-2 mm) in a mafic enclave hosted by an IPD1 and in the gabbro xenolith (Fig. 9b). Amphiboles in the DMP basaltic andesite dikes comprise 6-8% of the phenocrysts (0.05-1.6 mm). The Paredones basaltic andesite dike contains <1% amphibole phenocrysts (0.2-0.4 mm) displaying breakdown rims. Amphiboles from all samples contain inclusions, including apatite, plagioclase, and Fe-Ti oxides.

Representative compositions are given in Table 6 with additional analyses in Supplementary Data Table S6. All DMIC amphiboles are calcic and magnesium-rich; in the classification scheme of Leake *et al.* (2003) most are magnesio-hornblendes, tschermakite, and magnesiohastingsites, and less commonly edenite.

Amphibole compositions show prominent trends and groupings in plots involving alkalis $(Na + K)_A$, Mg-number $(Mg^{2+}/(Mg^{2+}+Fe^{2+})$ and Al_{TOT} (Fig. 10a and Fig. 10b). There are two trends of increasing alkalis with increasing Al_{TOT}, one with relatively high Al_{TOT} and one with lower Al_{TOT} (Fig. 10a). The low Al_{TOT} trend consists predominantly of amphiboles from the biotite tonalite, mafic enclaves and IPD2s. The high Al_{TOT} trend consists of the IPD3, the gabbroic xenolith, DMP basaltic andesite and the Paredones basaltic andesite. A few low Al_{TOT} amphibole analyses in IPD3 rim higher Al_{TOT} cores. The biotite tonalite shows both high and low Al_{TOT} amphibole analyses.

The predominant Mg-number trend shows a negative correlation between Al_{TOT} and Mg-number (Fig. 10b). This trend includes analyses from the biotite tonalite, mafic enclaves, gabbroic xenolith, IPD2 and IPD3. Offset from this trend is a group of amphibole analyses with high Al_{TOT} and a range of Mg-numbers. This group includes analyses from the two types of basaltic andesites and IPD3. The DMP and Paredones basaltic andesites contain amphiboles with some of the highest Al_{TOT} values, but fall into two separate Mg-number clusters (Fig. 10b). The DMP basaltic andesite amphiboles also have a wide range of Mg-numbers, whereas the Paredones basaltic andesite amphiboles are more tightly clustered. The biotite tonalite shows both high and low Mg-number clusters.

Chlorine in amphiboles shows a marked peak (0.16 wt. %) at intermediate Al_{TOT} (1.5 apfu). Within the DMIC, amphibole Cl content is lowest in the basaltic andesites, gabbroic xenolith and one of the IPD3 samples (Fig. 10c). Amphiboles of the IPD3 high Al_{TOT} group with high Mg-number have low Cl-contents. Low Al_{TOT} amphiboles in the biotite tonalite, IPDs and mafic enclave contain the highest Cl concentrations. For amphiboles with Al_{TOT} <1.5 Cl concentrations decrease with decreasing Al_{TOT},

describing well-defined trends in the biotite tonalite and mafic enclaves (Fig. 10c). With the exception of the IPD3 samples, amphiboles within a given sample have decreasing Cl content with increasing Mg-number. The IPD3 samples show no systematic correlation between Cl content and Mg-number.

Apatite

Apatite is ubiquitous in DMIC and occurs as inclusions within plagioclase, biotite and amphibole phenocrysts and as subhedral to anhedral grains within the matrix (Fig. 11a and Fig. 11b). Apatites in DMIC range in size from 10 μm to 200 μm, although an IPD2 (DM5AG27) and a quartz monzonite (DM6AG45) contain apatites up to 0.7 cm. Apatites in the DMP basaltic andesite are acicular (<100 μm in length) (Fig. 11c).

Apatite compositions are given in Table 8 and in Supplementary Data Table S7. No systematic differences in apatite compositions were found for different host crystals or apatite textures, or between apatite cores and rims in any of the DMIC units with the exception of the biotite tonalite. DMIC apatites are predominantly fluorapatite, with Cl contents consistently above detection limit (~150 ppm Cl). Apatites in the basaltic andesites have the highest Cl contents (Fig. 11d). Sulfur shows a much greater overall range than Cl. Apatite sulfur content is highest in the biotite tonalite and lowest in the basaltic andesite for which most analyses were below detection limit (~90 ppm S) (Fig. 11d). Data below detection limit are included in Figure 11d to demonstrate that many of the basaltic andesite analyses have very little S while still containing appreciable Cl. Although there is significant scatter, some clustering of high and low Cl contents in the IPD3s can be discerned over a range of S contents (Fig. 11d). Apatite inclusions in plagioclase in the biotite tonalite are, on average, higher in S than microphenocryst apatite.

Fe-Ti minerals

Magnetite, ilmenite, titanite, and rutile occur as inclusions in amphibole and biotite, as matrix grains, and, in hydrothermally altered samples, as replacements of amphibole and biotite. Within the quartz

monzonite, rhyolite and some equigranular biotite tonalites, magnetite and ilmenite display exsolution textures. In the porphyritic biotite tonalite and the intermediate porphyry dikes such exsolution textures are rare. Fe-Ti oxides are intergrown or in contact with apatite in many samples. Within the quartz monzonite, ilmenite occurs as inclusions within plagioclase phenocrysts whereas magnetite can be found both within phenocrysts and in the matrix. Rutile is common in the matrix of the quartz monzonite and in IPD1. In all mineralized samples pyrite is commonly in contact with the Fe-Ti oxides. Compositions for magnetite and ilmenite pairs are in Supplementary Data Table S8.

Zircon

Zoning and resorption textures

Zircon crystals are more abundant in the rhyolite, quartz monzonite, and biotite tonalite than in the IPD suite. No zircons were recovered from the basaltic andesite dikes. All zircon separates contain some zircons with mineral inclusions such as apatite and titanite as well as ovoid to irregularly shaped glassy melt inclusions up to 35 μm across. Representative images of zircon zoning and textures from CL imaging are provided in Fig. 12 and Supplementary Materials Figure S1.

Zircons from the rhyolite are typically ~100-300 μm in length and contain a mixed population of elongate or prismatic crystals with a few multifaceted crystals. CL imaging reveals oscillatory and strong sector zoning. Zircons from quartz monzonite are ~50-300 μm in length. Most are multifaceted crystals with large, rounded and resorbed cores with late-stage discordant rim overgrowths, but there are also elongate prismatic zircons with patchy zoned cores and oscillatory rims. Zircons from equigranular biotite tonalite and the porphyritic biotite tonalite are ~75-175 μm with two populations, namely euhedral, multifaceted crystals and prismatic crystals. Both populations contain zircons with oscillatory and/or sector zoning. Complex resorption features and abundant melt inclusions are observed in both populations. The zircons from the porphyritic biotite tonalite commonly contain darker, less luminescent cores and lighter, oscillatory-zoned rims than their equigranular biotite tonalite

counterparts. Sparse zircons from the IPD suite are ~40-150 μm and include both multifaceted and elongate prismatic morphologies. Elongate prismatic crystals show very few resorption surfaces and strong oscillatory zoning. The multifaceted crystals have large, rounded and resorbed cores with late-stage discordant rim overgrowths.

Trace element composition

Zircon trace element compositions and analysis locations are reported in Supplementary Data Table S9 and Fig. S1. Chondrite-normalized zircon REE concentrations within a sample may vary by approximately one order of magnitude and by as much as two across the entire DMIC (Fig. 12). All analyses show a prominent positive Ce anomaly although the magnitude of this anomaly is uncertain in samples where the concentration of La is below detection limit. A modest negative Eu anomaly is observed in almost all zircon analyses (Fig. 12). The more silicic units, the quartz monzonite, rhyolite, and the porphyritic biotite tonalite phases, show the highest total REE content (Fig. 12). There is no clear distinction between the total REE content of the three types of IPD.

The zircons from DMIC units have Hf contents that range from 8000-15000 ppm Hf. The Eu/Eu* and Hf show no correlation, and Eu/Eu* values vary widely from 0.15 to 0.93 with no clear discrimination between different DMIC units. Yb/Gd ratios (Fig. 13) also show a similar range for all DMIC units. Th/U values range widely, with the porphyritic biotite tonalite having the widest range (Fig. 13). Almost all DMIC negative Eu/Eu* anomalies are correlated with positive Ce anomalies, consistent with zircon geochemistry from other porphyry copper systems, and plot in the fertile field of Lu *et al.*, (2016). Tracking intra-grain variability in trace elements from core to rim in the IPDs was not possible due to the lack of zircons large enough for multiple analyses. However, in the more silicic units with larger zircons no systematic trends from cores to rims were observed.

INTENSIVE PARAMETERS FOR MAGMA STORAGE CONDITIONS

Amphibole-plagioclase temperatures

Thermometric calculations for the amphibole-bearing units of the DMIC, including the gabbroic xenolith and an IPD2-hosted mafic enclave (Table 9, Fig. 14a, and Supplementary Data Table S10) were made on touching amphibole-plagioclase pairs using thermometer B of Holland & Blundy (1994). The highest temperatures (950-970°C) from the Paredones basaltic andesite are based on plagioclase inclusions within amphiboles. The two DMP basaltic andesite samples, DM4AG28 and DM5AG34, have contrasted temperature ranges of 890-920°C and 650-710°C respectively. Two of the IPD3 samples recorded higher temperatures (790-850°C) than the IPD2 sample (720-800°C); however, a third IPD3 sample overlapped significantly (840-710°C) the IPD2 sample. The mafic enclave records temperatures over a wide range (840-675°C). The gabbroic xenolith also yields a large range (760-900°C) that overlaps with the IPD3s. Many of the biotite tonalite amphibole-plagioclase pairs yielded low temperatures (<680°C) (Fig. 14a) that lie just below or within error of the 100 MPa, water-saturated granite solidus (Johannes & Holtz, 2012). The wide range of calculated temperatures reflects compositional variation in amphibole due to the temperature-sensitive edenite exchange (Fig. 10a).

Ti-in-zircon temperatures

Ti-in-zircon thermometry was applied to eight DMIC samples using the calibration of Ferry & Watson (2007) (Fig. 14b; Supplementary Data Table S9). This thermometer requires estimates of the activities of SiO_2 and TiO_2 in the melt. Following the recommendations of Ferry & Watson (2007) $a SiO_2 = 1$ and $a TiO_2 = 0.7$ were assumed on the basis of the presence of quartz and Ti-bearing phases, such as titanite and/or titanomagnetite, in each of the units. Uncertainty in $a TiO_2$ may result in temperature variations of ~30˚C (Ferry and Watson, 2007). For some large crystals both core and rim measurements of Ti were made, but most DMIC zircons were only of sufficient size for a single, central 35 µm-spot measurement (see Supplementary Materials Fig. S1).

Although the majority of analyses shows no clear correlation between Ti concentration or Ti-in-zircon temperature with Hf concentration (a measure of differentiation), analyses with the highest Hf values

have low Ti and thus lower Ti-in-zircon temperatures. There is no clear pattern between estimated core and rim temperature values in any of the DMIC units. The range of temperatures for most of the DMIC units is wide (661-959°C), but for the mafic and intermediate units is in broad agreement with the range of amphibole-plagioclase temperatures (Fig. 14b). The biotite tonalite zircons yielded the greatest range of temperatures (689-959°C). The lowest temperatures in all of the DMIC units are near-solidus, with the quartz monzonite and rhyolite units having the lowest overall temperatures. For the IPDs the lowest calculated temperatures (672°C and 685°C) were from high-Hf resorbed cores in IPD3 sample DM6AG21.

The DMIC felsic units all have Ti-in-zircon temperatures that are at or above the granite solidus (680°-700°C) whereas the amphibole-plagioclase temperatures for the biotite tonalite (the only felsic unit with amphibole) are at or close to the solidus. These results suggest that the zircons are recording the temperature of the magmatic system, and the amphibole-plagioclase pairs are susceptible to re-equilibration during slow cooling of the intrusions. The IPDs and basaltic andesite dikes, by contrast, (with the exception of DM5AG34) cooled too quickly for re-equilibration and thus have amphibole-plagioclase temperatures that record magmatic conditions.

Redox constraints

There are several lines of evidence to constrain the redox state of DMIC magmas. The presence of primary anhydrite inclusions in plagioclase phenocrysts in the quartz monzonite, biotite tonalite, and in all three types of IPDs indicates a minimum oxidation state of NNO+1 (Carroll & Rutherford, 1987; Luhr, 1990; Matjuschkin *et al.*, 2016; Scaillet *et al.*, 1998). However, the oxidation state of the DMIC magmas must have varied during differentiation and ascent. The trend in DMIC amphiboles of increasing in Mg-number with decreasing Al_{TOT} (and temperature) is consistent with oxidation during cooling and fluid exsolution, as observed elsewhere (e.g. Czamanske & Wones, 1973; Blundy &

Holland, 1990). Also the lack of ilmenite in the groundmass of the DMIC units is consistent with oxidation during cooling (Wones, 1981).

Some constraints on the change in redox state that occurs during cooling can be made by assuming that the increase in amphibole Mg-number results solely from an increase in the ratio of Fe^{3+}/Fe_{tot} in the melt from which the amphiboles grew. In this way, an increase in Mg-number can be equated to a requisite change in Fe^{3+}/Fe_{tot}, which in turn can be related to a change in fO_2. This exercise requires information on the variation of melt Fe^{3+}/Fe_{tot} with fO_2 and the exchange coefficient KdFe-Mg for amphibole. For the former we use the algorithm of Kress & Carmichael; for the latter we adopt a value of 0.53 from the experimental study of Nandekar *et al.* (2014). Taking the biotite tonalite as an example, at an initial fO_2 = NNO+1 and a typical temperature of 800°C, the calculated Fe^{3+}/Fe_{tot} is 0.19. For amphibole KdFe-Mg of 0.53 this corresponds to Mg-number of 0.73, consistent with high Al_{TOT} amphiboles from the biotite tonalite (Fig. 10b). To increase the Mg-number to 0.80, for the same KdFe-Mg and temperature, would require an increase in Fe^{3+}/Fe_{tot} of 0.36, corresponding to increase in fO_2 to NNO+3. Rutherford & Devine (1988) show increasing amphibole Mg-number with increasing fO_2 for a fixed temperature for experiments based on Mount St. Helens dacite. In the Pinatubo experiments of Prouteau and Scaillet (2003) amphibole Mg-numbers are insensitive to temperature for the range of fO_2 investigated, and high experimental fO_2 resulted in high amphibole Mg-number for pressures of both 400 and 960 MPa.

Our calculations assume a constant KdFe-Mg over the relevant temperature and melt compositional range. Changing KdFe-Mg from 0.53 to 0.35 could also produce the range of amphibole Mg-number observed in the DMIC biotite tonalite at a fixed fO_2 of NNO+1. Nandekar *et al.* (2014) showed that KdFe-Mg for amphibole can change with temperature, 0.53 at 830°C and 0.27 at 730°C, for a nominally fixed fO_2 in a series of fractional crystallization experiments based on a starting composition from the Adamello batholith. While it is unlikely that the DMIC experienced a fixed fO_2, it is possible that a combination of cooling (which serves to increase increase Kd) and oxidation (which

serves to increase Fe^{3+}/Fe_{tot}), are responsible for increase Mg-number in the biotite tonalite amphiboles. We suggest that the tendency for Mg-number to increase as Al(iv) decreases (e.g. Blundy & Holland, 1990) is a cooling and oxidation phenomenon that is quite widespread in plutons as they approach their solidi.

Oxygen fugacity estimated by Fe-Ti oxide barometry was limited to IPD and porphyritic biotite tonalite magnetite-ilmenite pairs. Exsolution textures, indicative of slow cooling, were ubiquitous in the quartz monzonite, rhyolite and equigranular biotite tonalite, so no estimates were acquired for these units. The Andersen & Lindsley (1985) oxythermobarometer was applied to adjacent pairs in an IPD2, IPD3 and porphyritic biotite tonalite sample to estimate the final, re-equilibrated oxidation state of the magmas using the ILMAT program of Lepage (2003) (Supplementary Data Table S8). All three samples yielded near- to sub-solidus temperatures. The magnetite-ilmenite temperatures range from 533 to 697°C (Fig. 14a), with mean temperatures of 592° ± 38°C for the IPD2, 585° ± 28°C for the IPD3, and 618° ± 18°C for the porphyritic biotite tonalite. The corresponding oxygen fugacities for these samples ranged from NNO+2 to NNO+5 with an average for each sample of NNO+3 (Supplementary Data Table S8). This is consistent with the observed increase in amphibole Mg-number and suggests strongly that in their near- to subsolidus state DMIC magmas were very oxidized.

Pressure Constraints

Emplacement pressures

To estimate emplacement pressures at Don Manuel, we applied the Al-in-hornblende barometer of (Mutch *et al.*, 2016). This barometer requires a low thermodynamic variance mineral assemblage and petrographic evidence that this assemblage is in equilibrium (Anderson *et al.*, 2008; Blundy & Cashman, 2008). Uncertainty in pressure estimate is 15% relative (Mutch *et al.*, 2016). Only three samples in the biotite tonalite contained the complete equilibrium buffering assemblage (amphibole, biotite, plagioclase, potassium feldspar, quartz, magnetite, titanite, and apatite) required for barometry. The

barometer cannot be applied to amphiboles in the IPDs, basaltic andesites, mafic enclave, or the gabbroic xenolith.

Samples DM4AG14, DM4AG08, and DM4AG16 recorded mean pressure estimates of 118 ± 10 MPa, 120 ± 19 MPa, and 125 ± 10 MPa, respectively (Supplementary Materials Data Table S11). The amphibole-plagioclase thermometry temperatures calculated for these samples (Table 9) are consistent with the wet granite solidus at this pressure. These pressures are in line with the minimum pressure constraints placed on the DMIC by overburden thickness. Sample (borehole) elevations range from 2760-2836 m (a.s.l.), and the DMP area is adjacent to a ridge of Coya Machali/Farellones Formations that reaches 5100 m (a.s.l.). This means overburden pressure would have originally been ≥60 MPa.

Pressures inferred from experimental petrology

We attempted to estimate pressures from DMIC samples using experiments performed on natural systems with similar phase assemblages and bulk compositions. Since experimental and natural bulk compositions do not match exactly and some DMIC magmas are themselves the products of magma mixing, the inferred pressures should be viewed as indicative.

The 1991 Pinatubo eruption produced amphibole and biotite-bearing dacites with similar composition to those of the IPDs and biotite tonalite. Experiments by Scaillet & Evans (1999) and Prouteau & Scaillet (2003) produced amphibole compositions very similar to those of the IPDs. The temperatures of the Pinatubo experiments range from ~750°-900°C at 220 MPa, ~780°-950°C at 400 MPa and ~750°-995°C at 960 MPa (Prouteau & Scaillet, 2003; Scaillet & Evans, 1999). We have plotted the fields of the experimental amphiboles in Fig. 15 along with the DMIC amphibole compositions. The experimental amphiboles for a given pressure describe trends of decreasing Altot with decreasing Mg-number and $(Na+K)_A$ consistent with isobaric cooling. With decreasing pressure each isobaric trend is displaced to lower Altot, reflecting the temperature and pressure sensitivity of

Altot. In general, the comparison suggests that the spread of DMIC amphiboles records a combination of decompression and cooling driving amphiboles to lower Al_{TOT}.

Amphiboles in the biotite tonalite are commonly closely associated with or intergrown with phases such as plagioclase, biotite, and titanite. Their low plagioclase-amphibole temperatures and overall low Al_{TOT} contents in amphibole suggest that the tonalite evolved in a shallow crustal magmatic reservoir. This inference is consistent with amphiboles in the high Al_{TOT} and $(Na + K)_A$ population in the biotite tonalite overlapping in composition with those of the 220 MPa Pinatubo experiments (Fig. 15a and Fig. 15b). Amphiboles in the biotite tonalite include a population with lower values of Al_{TOT} and $(Na + K)_A$ (Fig. 15a) and higher Mg-numbers (Fig. 15b), which likely reflects lower temperatures (544-769°C) and lower pressures than in the experiments, consistent with application of the Al-in-hornblende barometer to these samples. The increasing Mg-number with decreasing Al_{TOT} is ascribed above to oxidation during cooling and decompression.

The IPD2s and mafic enclave have a few amphibole compositions that overlap with the 220 MPa experiments. However, most of the amphiboles have lower Al_{TOT} than the field defined by the Pinatubo experiments (Fig. 15a), suggesting that they formed at lower temperatures. The majority of the IPD3 high-Al_{TOT} amphiboles overlap with the 400 and 960 MPa amphibole compositions in Fig. 15a. However, many analyses extend to lower $(Na+K)_A$ and Al_{TOT} values than the Pinatubo experimental amphiboles at those pressures, much like the 1991 Pinatubo dacite amphiboles. The IPD3 low Al_{TOT} amphiboles overlap with the 220 and 400 MPa amphibole compositions (Fig. 15b). Both the Paredones and DMP basaltic andesite amphiboles, as well as a few analyses from the gabbroic xenolith, have compositions similar to the Pinatubo 960 MPa experimental amphiboles (Fig. 15a and Fig. 15b), although the basaltic andesite units are less evolved than the starting compositions used in the Prouteau & Scaillet (2003) experiments. Overall the comparison indicates polybaric crystallization of amphibole in the magmatic system supplying the DMIC. The influence of changing pressure is allied to cooling and oxidation.

Volatiles in the DMIC system

High initial H_2O content in primitive basalt magmas is common in arc magmatic systems, commonly being 4% or more (Plank *et al.*, 2013). The H_2O content of derivative silicic magmas will be even higher by factors of 2 to 3 (Annen *et al.*, 2005). The magmas of the DMIC likely had relatively high magmatic H_2O content as all units stabilize a texturally-early hydrous phase of either amphibole or biotite or both. Experimental data from Scaillet & Evans (1999) and Prouteau & Scaillet (2003) for Pinatubo volcano and from Costa *et al.* (2004) for Volcan San Pedro provide constraints on the range of possible H_2O contents for the IPDs of the DMIC. Experiments with run product mineral assemblages similar to that of IPD1 (plagioclase + biotite + Fe-Ti oxides), IPD2 (plagioclase + amphibole + biotite + Fe-Ti oxides), and IPD3 (plagioclase + amphibole + Fe-Ti oxides) for the temperature ranges calculated from plagioclase-amphibole thermometry suggest H_2O contents in the range of 5-10 wt. %. The pressure estimates presented above also enable constraints. For example between 120 and 200 MPa the saturated H_2O content of the biotite tonalite magma would be 4.5-6 wt.% (e.g. VolatileCalc, Newman *et al.*, 2002; Liu *et al.*, 2005).

Apatite as a volatile monitor

Apatite reflects magmatic volatile evolution due to halogen, sulfate and hydroxyl anions within its structure (Boyce & Hervig, 2008, 2009; Dietterich & de Silva, 2010; Imai, 2004; Parat *et al.*, 2002; Parat & Holtz, 2004, 2005; Peng *et al.*, 1997; Scott *et al.*, 2015; Streck & Dilles, 1998; Van Hoose *et al.*, 2013). DMIC apatites display a wide range in Cl and S concentrations (Fig. 11d). Both variations in oxidation state with changed S speciation (Matjuschkin *et al.*, 2016) and mixing of fluids from different magmas (Christopher *et al.*, 2010) could result in these ranges in concentrations. Modeling the details of volatile degassing using apatites is therefore problematic (Scott *et al.* 2015). For Don Manuel we have no direct analysis of OH in the apatites and do not have any direct constraints on the compositions of the melt or coexisting fluids, precluding definitive interpretation. Nonetheless, we can use the covariation of

S and Cl in apatites, along with high-temperature experiments on degassing magmas to better understand volatile evolution in the DMIC.

In the biotite tonalite, early apatite inclusions in plagioclase phenocrysts have higher S contents than apatite microphenocrysts. This change may reflect S degassing or a more reduced system. The latter explanation is unlikely due to the evidence for oxidized magmas containing anhydrite (Carroll & Rutherford, 1987; Luhr, 2008; Matjuschkin *et al.*, 2016; Scaillet *et al.*, 1998) and the trend of increasing Mg-number in amphiboles discussed above. If the decrease in apatite S is simply due to anhydrite crystallization then the requisite temperature drop would reflect the changing solubility of anhydrite with temperature. A 1000x drop in apatite S would require cooling on the order several hundred degrees, which we consider implausible. Fractionation of apatite cannot drive the trend to low S, because the mass fraction of apatite crystallizing is simply too low. Higher S contents in apatite inclusions versus that of apatite microphenocrysts has also been observed in the La Huifa-La Negra prospect northeast of the El Teniente PCD (Hernandez & Rabbia, 2009), in andesites and dacites from Santiaguito Volcano in Guatemala (Scott *et al.*, 2015), and in the quartz diorite porphyry of the Dizon porphyry copper deposit in the Philippines (Imai, 2004). In the latter case, this observation was ascribed to degassing of oxidized sulfur.

For the DMP basaltic andesite dikes in the DMIC, the acicular, late stage apatites have the overall lowest S contents (Fig. 11c). The most likely explanation for the low S in the DMP basaltic andesite apatites is degassing of S prior to apatite crystallization, as has been suggested for apatites in systems where degassing modeling replicates both S isotopic composition and concentration variation (e.g. Economos *et al.*, 2017). Alternatively, the mafic magmas could be more reduced at Don Manuel, perhaps enabling crystallization of a sulfide phase and therefore the melts contained less S^{6+}. Many of the IPD samples contain apatite grains that have very large ranges of S content. This may be the result of fluctuations in fS_2 / fO_2, changes in temperature or melt composition, perhaps associated with magma mixing.

We can address the latter possibilities by considering the covariation of Cl with S in DMIC apatites, where there is a clear decoupling of Cl and S. For example, the DMP basaltic andesite dikes, which crystallize apatite late have almost no S, but have some of the highest Cl contents. Chlorine in apatite is controlled by the Cl content of the system, melt composition, Cl solubility in the melt and pressure (Doherty *et al.*, 2014). Closed-system equilibrium experiments by Lesne *et al.* (2011) and Fiege *et al.* (2014) that simulate degassing in basalts and andesites, respectively, under oxidized conditions showed that the fluid/melt partition coefficient of S ($D_S^{fl/melt}$) increased sharply at around 100 MPa for basalts and 200 MPa for andesites; in contrast Cl remains in the melt even to very low pressures (Fig. 16a). Thus magma degassing leads, inevitably, to strong decoupling of S from Cl in the melt phase. This exact same pattern of decoupling is observed in the DMIC apatites (Fig. 11d) as well as apatites from Santiaguito and Pinatubo volcanoes and the Santa Rita porphyry copper deposit (Fig. 16b) (Audétat *et al.*, 2004; Scott *et al.*, 2015; Van Hoose *et al.*, 2013). Blundy *et al.* (2008) have previously noted the strong decoupling of S from Cl in melt inclusions from Mount St. Helens, where the driving force for crystallization in decompression-induced degassing. Late stage, silica-rich melts are enriched in Cl (up to 3000 ppm) but have negligible S (<100 ppm). Chlorine only appears to degas significantly at the lowest pressures, when melt compositions have become highly silicic. In the next section we explore whether near-solidus amphiboles from the DMIC testify to similar, late-stage Cl loss from the system.

Cl in Amphibole

For a given temperature and Al_{TOT}, amphiboles in DMIC biotite tonalite and mafic enclave commonly have higher Cl than those in the IPDs or basaltic andesite, which may be explained by the degree of differentiation that serves to increase Cl in the melt (Fig. 10c and Fig. 17a). When Cl-content is plotted versus the temperatures estimated from the plagioclase-hornblende thermometry (Fig. 17a), there is a striking peak in amphibole Cl-content at temperatures just above the solidus. From this peak, Cl content decreases with declining temperature consistent with its efficient extraction from the system. The trend of increasing Cl with decreasing Al_{TOT} may be explained by the fact that early on during differentiation

any fluid lost is likely water-rich with little Cl, such that Cl becomes increasingly enriched in the melt. At lower pressures the Cl content of the fluid increases, as does the overall amount of fluid degassed, and thus bulk $D_{Cl}^{fl/melt}$>1. Consequently, Cl content in the amphiboles declines. This peak may represent a larger $D_{Cl}^{fl/melt}$ or the point at which a fluid is exsolved, either as a high-salinity, single-phase fluid or as a brine (cf. Cline & Bodnar, 1991). This conclusion is supported by the experimental study of amphiboles from the 1991-1995 Unzen dacite by Sato *et al.* (2005) who show that, despite the dependency of amphibole-melt Cl partitioning on amphibole Mg-number, significant Cl loss to fluid is required to explain the observed three-fold drop in Unzen amphibole Cl content.

To explore further the fall in Cl in the melt during the final stages of crystallization we have calculated the Cl content of the melt coexisting with amphibole using the Cl/OH exchange coefficient ($Kd_{Cl\text{-}OH}$) of Sato *et al.* (2005) $Kd_{Cl\text{-}OH}$ depends on temperature and amphibole Mg-number. We calculate the Cl/OH ratio of amphiboles using stoichiometry and convert this to Cl_{melt} using $Kd_{Cl\text{-}OH}$ at the amphibole-plagioclase temperature and the OH content of a water saturated melt at a notional pressure of 100 MPa using VolatileCalc (Newman *et al.*, 2002). Results are plotted in Fig 17b. Our calculations show a decline in Cl_{melt} from ~600 ppm at 850°C to less than 100 ppm below 600°C. Higher pressures of calculation would increase the OH content of the water-saturated melt and increase Cl_{melt} pro rata.

DISCUSSION

Our observations of mineral assemblages, textures, mineral chemistry, geochronology and geochemistry are now used to discuss the petrogenesis and evolution of the DMIC. Broadly, the story is one of polybaric fractionation of magmas in an extensive, trans-crustal magmatic system. Igneous mixing is prominent and is associated with episodic emplacement of magmas into the shallow crust, but does not drive the overall chemical evolution of magmas. The DMIC also shows evidence of degassing due to decompression. Finally, implications of the inferred igneous processes, temporal evolution of the system, and episodic character of the emplacement for porphyry copper mineralization are discussed.

Polybaric Fractionation

Although many DMIC units exhibit evidence of igneous mixing processes, there is information, particularly in the mineral chemistry, to elucidate differentiation processes. The broad range of compositions in the units of the DMIC, from basaltic andesite to rhyolite, and their closely spaced ages suggest that they could be related to one another by differentiation of a single parent. However, we infer below that parental magmas differentiated at different pressures resulting in a range of pH_2O and water contents as the magmas evolved.

Plagioclase crystals in the DMIC show large variations in An-content and Sr concentrations that provide evidence for changing magma compositions and conditions during crystallization. Importantly, trends of decreasing Sr with decreasing An in the DMIC (Fig. 7) indicates differentiation (because Sr is a compatible element in plagioclase). Such trends are not consistent with diffusive equilibrium which drive Sr to the low An parts of a crystal leading to negative correlations in Sr-An space (Dohmen & Blundy, 2014). The lack of such correlations in the DMIC indicates plagioclase crystals cannot be very old in terms of their growth before they were quenched during emplacement. Dohmen *et al.* (2017) show that for a 300 μm crystal positive correlations in Sr-An space can be effectively eliminated in ~1 year at temperatures of 1200 °C. For temperatures more appropriate to DMIC (e.g. 950 °C) the timescale to eliminate positive Sr-An correlations is approximately 100 years using the diffusion coefficients of Cherniak & Watson (1994). Thus, DMIC plagioclase crystals record a crystallization trend that can be used to interpret melt evolution.

The two main trends observed in Sr concentration in plagioclase (Fig. 7a, 7b and Fig. 18a) are interpreted to result from variation in the point at which plagioclase saturates during magma differentiation. The trend of relatively constant plagioclase Sr concentration with changing An content (Trend 1 of Fig. 18a), can be explained by abundant early plagioclase crystallization, with a bulk $D_{Sr} \approx 1$ (i.e. $D_{Pl\,Sr} * xPl \approx 1$). The trend of decreasing Sr with decreasing An concentration (Trend 2;

Fig. 18a) requires crystallization of plagioclase from melts that have become significantly enriched in Sr prior to plagioclase saturation. This enrichment is attributed to the absence of plagioclase in the fractionation assemblage during early differentiation. Subsequent plagioclase crystallization then reduces Sr in the melt (bulk D_{Sr}>1). Plagioclase crystallization is known to be suppressed in magmas with high H_2O content at high pressure resulting in crystallization of lower silica phases, such as clinopyroxene and amphibole, instead (Matjuschkin *et al.*, 2016; Moore & Carmichael, 1998; Müntener *et al.*, 2001). Trend 1 (Fig. 18), represented by the mafic DMIC units (Fig. 7a) and plagioclase populations (An>45) in the IPD2 and IPD3 dikes (Fig. 7b), are interpreted to be related to differentiation of shallower, perhaps less wet magmas in which plagioclase crystallizes from the onset. By contrast, trend 2 (Fig. 18), represented by the silicic DMIC units, is the trend of magmas crystallizing at higher pressures and higher pH_2O in which early plagioclase crystallization is suppressed. The lower An content of plagioclase at the moment of saturation is consistent with prior crystallization of calcic amphibole and/or clinopyroxene, that sequester Ca, but not Sr. This is indicated schematically by the negative slope on the vector labelled Xpl≈0 in Fig. 18a.

The differences in H_2O content could either reflect differences in the H_2O content of primitive basalts from the mantle or more likely differences in the amount of H_2O-undersaturated crystallization that precedes plagioclase saturation. The latter effect could arise due to different pressures of differentiation, leading to different pH_2O at the point of plagioclase saturation. In general, for H_2O-saturated mafic to intermediate magmas, the liquidus of plagioclase increases with decreasing pressure while the amphibole liquidus remains almost constant over a large pressure range (Blundy & Cashman, 2001; Prouteau & Scaillet, 2003; Riker *et al.*, 2015): trends 1 and 2 are thus favored by low and high pH_2O respectively. Plagioclases in IPD1 dikes and the high Sr population in IPD2 dikes (Fig. 7a) are consistent with trend 2. Although there are overlaps between the groupings in Fig. 7a and Fig. 7b, they are also displaced from one another indicating differences in differentiation conditions. Despite following the same overall Sr versus An content trend, the plagioclases in DMP basaltic andesite dikes

and IPD3s have higher Sr values for a given An content than do those of the Paredones basaltic andesite dikes (Fig. 7a and 7b). This difference could be attributed to the DMP basaltic andesite parent magma containing more H_2O than the Paredones basaltic andesite, or their respective parental magmas having had different Sr contents. The former interpretation is supported by the fact that the DMP basaltic andesite and IPD3 contain only amphibole as mafic phenocrysts whereas the Paredones basaltic andesite has abundant clinopyroxene but only minor amphibole. This observation alone, however, does not rule out differences in initial Sr concentrations in the respective parental magmas.

In order to address the question of how much water and at what pressure is plagioclase suppressed in DMIC magmas, crystallization modeling of the magmatic system was conducted using the Rhyolite-MELTS thermodynamic modeling software of Gualda *et al.* (2012). Simulations were carried out to assess the impact of magma H_2O content and pressure on plagioclase crystallization. The calculations provide a framework for interpreting the plagioclase compositional trends of the Don Manuel magmatic system. We used one of the least evolved basaltic andesite dikes, DM5AG34 (53 wt. % SiO_2; Supplementary Materials Data Table 12), as the end-member starting composition. Isobaric simulations were run for various pressures (200, 400, and 600 MPa) and initial H_2O contents (2, 4, and 6 wt. %). A fixed oxygen fugacity of NNO was assumed. For all pressures, the onset of plagioclase crystallization was suppressed to higher crystallinities with increasing H_2O content and increasing pressure as anticipated. For example, for 200 MPa plagioclase joins the crystallizing assemblage at ~9% crystallinity at 2 wt. % H_2O, but not until ~29% crystallinity at 6 wt. % H_2O. As crystallization pressure is increased, significant prior crystallization of clinopyroxene means that liquidus plagioclase is displaced to lower initial An content at the point of saturation, due to preferential depletion of the melt in Ca versus Na. Thus at 200 MPa and 6wt% H_2O the first plagioclase to saturate is An_{78} at 29% crystallinity, whereas at 600 MPa and 6wt. % H_2O it is An_{46} at 45% crystallinity. Compared to crystallization pressure, the effect of initial H_2O content is less pronounced due to the counteracting effects of pH_2O and prior clinopyroxene crystallization on plagioclase liquidus compositions. For

example, the difference in plagioclase composition at the point of saturation at 600 MPa is An_{46} with 6 wt% H_2O and An_{50} with 4 wt% H_2O. The corresponding dissolved H_2O contents in the melt are 10.2 and 6.7 wt% respectively.

The same Rhyolite-MELTS calculations can be used to model Sr content in plagioclase. Figure 18b shows the resulting calculations of Sr in plagioclase for the initial H_2O contents of 2, 4, and 6 wt. % and pressures of 200, 400, and 600 MPa using An initial Sr melt concentration of 500 ppm and Sr partition coefficients estimated from the plagioclase An content using the equation of Blundy & Wood (1991). Simulations with H_2O contents greater than 4 wt. % at pressures of 400 MPa and higher have plagioclase with significantly higher Sr contents that match trend 2 in Fig. 18a and similar to the DMIC data for the biotite tonalite and rhyolite in Fig 7a. Lower pressure calculations (200 MPa) and lower H_2O content calculations that result in earlier plagioclase saturation have lower Sr contents in plagioclase and result in much flatter trends like that of trend 1 in Fig. 18a and that of the basaltic andesites and mafic enclave in Fig. 7a. Thus, variations in the crystallization pressure of magmas with similar initial Sr and H_2O content can account for the observed Sr-An systematics of DMIC plagioclases. Our calculations support a model of polybaric ponding and differentiation of broadly similar parental magmas within the crust, rather than discrete batches of magmas with different H_2O and Sr contents.

Amphibole-rich gabbroic xenoliths and the abundance of amphibole in the mafic and intermediate units of the DMIC indicate the importance of amphibole as a fractionating phase during differentiation. The DMIC units show characteristic concave-upwards REE patterns and depletions in Nb and Ta, consistent with amphibole fractionation (Gilmer *et al.*, 2017). The high Al_{TOT} amphiboles of the gabbroic xenolith, IPD3, DMP basaltic andesite, and the Paredones basaltic andesite indicate that amphibole crystallization began perhaps at pressures as high as 960 MPa (Fig. 15a and 15b) corresponding to depths on the order of 40 km. Current crustal thickness in this area of ~45-50 km has been interpreted to have been reached around 4 Ma (Farías *et al.*, 2008; Farías *et al.*, 2010; Gilbert *et al.*, 2006; Marot *et al.*, 2014). Amphibole likely continued to crystallize at different pressures and depths

throughout the trans-crustal magmatic system as indicated by the wide range in Al_{TOT} in the amphibole-bearing units of the DMIC (Fig. 15a and 15b).

Crustal assimilation and mantle source heterogeneity

Isotopically, DMIC magmas are consistent with the other Sr, Nd, and Hf isotopic studies within this section of the Andes that have identified a temporal evolution to more enriched compositions with time since the Oligocene/Early Miocene (Figs. 4 and 5) (e.g. Holm *et al.*, 2014; Kay *et al.*, 2005; Stern *et al.*, 2011b). Several different models have been proposed to explain the evolution to more enriched compositions in the NSVZ compared with compositions of rocks further south in the SVZ. Hildreth and Moorbath (1988) first proposed that along-strike isotopic signatures in the SVZ were controlled by MASH (Mixing, Assimilation, Storage, and Homogenization) processes with crustal assimilation being more significant in the NSVZ where the crust is thickest. By contrast, Stern (1991), Kay *et al.* (2005), Stern *et al.* (2011b) and Holm *et al.* (2014) argued that isotopic variability had to arise from the mantle due to the lack of isotopic variation with increased silica content. They invoked subduction erosion of the Paleozoic Chilenia crust as the source of contamination in mantle. A third model invokes mantle heterogeneity to explain the enriched composition in the NSVZ with little to no involvement of the crust (Jacques *et al.*, 2013; and Turner *et al.* 2017). Alternatively, some combination of the models presented above could be at play.

There is broad regional trend of enrichment of Sr, Nd, and Hf with age (Fig. 4 and Fig. 5). The most depleted Sr and Nd compositions in NSVZ are those of the Coya Machali/Abanico Formation and the older Teniente rocks (34-15 Ma) (purple field on Fig. 4). The Teniente rocks with ages of 15-7 Ma (blue field on Fig. 4) are more enriched. The Teniente and DMIC samples with ages between ~7 to 3 Ma overlap somewhat with the 15-7 Ma samples, but mostly extend to more enriched Sr and Nd isotopic compositions including the most mafic DMIC sample analyzed, DM7AG26, with 5.7 wt. % MgO. Rocks of the NSVZ that are <1 Ma have the most enriched compositions.

The compiled DMIC zircon Hf data (Fig. 5) suggest continued crustal contamination for the past 15 Myr. By projecting along an average continental crustal evolution trajectory ($^{176}Lu/^{177}Hf$), it can be assumed that the present day εHf of the Cuyania terrane is ~15 (Jones *et al.*, 2015; Muñoz *et al.*, 2013; Pepper *et al.*, 2016). Simple bivariate mixing implies the DMIC has incorporated 3-4% of the Cuyania terrane, which is in slight contrast to 1-2% mixing of the Cuyania terrane estimated from the Sr and Nd isotopes (Fig. 19). It is difficult to truly assess the origin of this enriched whole rock Sr and Nd isotopic composition of the DMIC since the most mafic samples are all basaltic andesite with MgO<5.8 wt.% (Supplementary Data Table S1). Aside from the three outlier basaltic andesites, Sr and Nd isotopic compositions within the DMIC do not vary with SiO_2, suggesting little crustal assimilation during differentiation or little isotopic leverage from a crustal assimilant (Fig. 4).

Mixing of magmas, mushes, and cumulates

Igneous mixing in the DMIC encompasses a range of possible processes. Magma mingling, one variety of igneous mixing, is documented by the presence of mafic enclaves and their crenulated contacts in the rhyolite, biotite tonalite, and intermediate porphyry dikes. The assemblage of multiple populations of plagioclase phenocrysts (Fig. 7) with complex anorthite zoning and disequilibrium textures indicates a significant degree of hybridization and thermal mixing in the IPDs of the DMIC. The crystal cargo observed in the IPDs could include phenocrysts which grew in the magma itself; antecrysts from earlier, related pulses in the magmatic system; and/or xenocrysts from previous, unrelated magma. The distinction between antecrysts and phenocryst becomes blurred when one considers that crystals in a trans-crustal magmatic system could be remobilized multiple times. Numerous glomerocrysts and crystal clots occur in these dikes, suggesting entrainment from crystal mushes and cumulates disturbed during magma ascent. When recharge magma pulses remobilize these crystals, new rims can grow

around preexisting cores. Consequently, the mixing process in the DMIC could have taken place across the entire length of the trans-crustal reservoir.

Mixing evidence from plagioclase

Three types of IPD were identified based on the hydrous mafic phase(s) present, IPD1 having only biotite, IPD2 having biotite and amphibole, and IPD3 having only amphibole. The IPDs show a large variability in Sr for a given plagioclase An content (Fig. 7b) and the compositions fall between and overlap the two end-member Sr-An trends. Such a mixture of compositions requires mixing the high-Sr melt and crystals with low-Sr melt and crystals, as well as growth of new crystals with intermediate compositions (Fig. 7b). The majority of plagioclase analyses for the IPD1 and IPD2 plot from the higher Sr trend to the middle, with the IPD2 containing the widest range of Sr for a given An content, whereas IPD3 has Sr compositions that predominantly plot along the lower, relatively constant, Sr trend as well as a few compositions extending all the way to the upper trend (Fig. 7b). These results indicate variability in Sr concentration in the melt at the point of plagioclase saturation (Fig. 18), which can be explained by mixing of magmas with different crystal cargo and melt lenses with variable storage pressures and pH_2O content. We infer that mixing reflects deeply fractionated magmas interacting with shallower magma bodies of broadly similar heritage.

Assembly of the DMIC

The most important factors controlling the petrogenesis and assembly of the DMIC are depth of differentiation (Annen *et al.*, 2005), initial H_2O content of the magmas (Jagoutz *et al.*, 2011; Sisson & Grove, 1993), and igneous mixing processes. Here we present a petrogenetic model based on age constraints from Gilmer *et al.* (2017) for the formation of the DMIC, illustrated in Fig. 20.

Mafic parental magmas for the DMIC are attributed to flux melting of the mantle wedge caused by slab-derived hydrous fluids. These wet magmas then migrated to the base of the crust where they stalled in a deep crustal hot zone (Annen *et al.*, 2005). H_2O contents become enriched in the deep crustal

hot zone during early differentiation (Annen *et al.*, 2005; Loucks, 2014; Richards, 2011). Early fractionation of hydrous primitive basaltic magmas is expected to be dominated by silica-poor minerals, such as olivine, clinopyroxene and amphibole, resulting in silica enrichment of the residual liquids. Our data provide direct evidence for amphibole fractionation, although other mafic phases are implicated by the low Mg numbers of the mafic rocks. Comparison of high Al_{TOT} amphibole "antecryst" compositions in DMIC rocks with experimental data at pressures of 960-400 MPa (Fig. 11) indicates fractionation in the lower or middle crust (current crustal thickness ~45-50 km) with equivalent depth range of 40 to 15 km. The abundance of amphibole and/or biotite in the DMIC units suggests all were derived from hydrous parental melts. However, the parental magmas likely differentiated at different pressures resulting in different pH_2O with consequences for plagioclase saturation and composition.

As magmas periodically detached from their solid residues and rose through the magmatic plumbing system, magma lenses that were compositionally similar, but variably evolved, likely amalgamated and mixed at different depths in the trans-crustal reservoir (Blundy *et al.*, 2015; Christopher *et al.*, 2015). In the case of the ~3.975 Ma quartz monzonite and ~3.879 Ma rhyodacitic magmas, the earliest and most silicic units recognized in the DMIC, some of the melt produced in the crustal hot zone migrated into the upper crust with limited interaction with more mafic melt or cumulate material. Ti-in-zircon temperatures in these units show a range of temperatures recording the magmatic range of crystallization in the upper magma reservoir (Fig. 14b). Resorbed zircon cores in these units are less common than in other units, but may reflect crystallization processes in the upper crustal magma bodies that supplied the hypabyssal intrusions.

The equigranular biotite tonalite magma was emplaced in the upper crust (at 3.5 to 5 km from Al-in-hornblende geobarometry) and solidified at ~3.83 Ma. The porphyritic biotite tonalite, emplaced at ~3.73 Ma, contains more amphibole than the equigranular tonalite. Although resorption features are common in the biotite tonalite zircons, we did not find zircon fractions that fell outside the analytical age uncertainties. The lack of overlap in the zircon ages of these units requires that the equigranular and

porphyritic biotite tonalites are distinct intrusive pulses. This observation suggests zircon resorption events occurred within the timeframe of the weighted mean ages plus/minus their uncertainty. The pulsed nature of the intrusive units suggests that protracted crystallization in the upper crustal reservoir was minimal. In the biotite tonalite there is no evidence of upper crustal protracted magma mush storage at zircon-saturated conditions.

Both types of biotite tonalite contain mafic enclaves, but in each case the phenocryst assemblages are much less heterogeneous than that of the IPDs, suggesting the biotite tonalite crystallized from a more homogeneous magma. Ti-in-zircon temperatures for the biotite tonalites record the wide range of magmatic temperatures whereas amphibole-plagioclase temperature estimates for the equigranular and porphyritic biotite tonalites record near-solidus temperatures and post-emplacement subsolidus reequilibration temperatures (Fig.14a and Fig. 14b). Recharge into the cooler, more crystalline tonalite mush made hybridization rheologically difficult resulting in mingling, as the mafic input crystallized quickly (Sparks & Marshall, 1986). The mingling end-member variety of igneous mixing in the biotite tonalite likely took place during emplacement and temperatures may have been too low to sustain more thorough hybridization.

Accumulation of magma in the upper crust waned after the emplacement of the biotite tonalite. Although basaltic andesite dikes periodically intruded the system (Gilmer *et al.*, 2017), the dominance of intermediate to felsic rocks suggests that very little mafic magma reached the upper crust without hybridizing. These hybrid magmas crystallized further in the upper crust as indicated by their low Al_{TOT} amphiboles.

The complexity of the phenocryst assemblages in the suite of hybridized IPDs and zoning patterns in those phenocrysts requires an open system with multiple stages of polybaric differentiation as well as entrainment of crystal residues. Both the textures and chemistry of the phenocrysts suggest that within the plumbing system batches of magma variously disrupt cumulates and crystal mush, entrain

crystals, and mix with pockets of melt that have variable fO_2, composition and volatile contents, as they ascended to shallow crustal depths during episodes of destabilization (Cashman *et al.*, 2017). Gabbroic crystal clots and glomerocrysts found in IPDs are similar to the gabbroic xenolith hosted by a basaltic andesite dike. This suggests that other cumulate crystals may also be entrained in the upward migration through the trans-crustal system. Lenses of melt that are remobilized may be the products of magmas that have already differentiated and hybridized multiple times within crustal hot zones.

Zircon age ranges within particular samples indicate that the IPDs with different phenocryst contents (e.g. with or without amphibole or biotite or high-Al amphibole versus low-Al amphibole) crystallized late-stage zircons within a narrow time period during shallow crustal emplacement (Gilmer *et al.*, 2017). This observation can be explained if the magmas were zircon-undersaturated throughout most of their evolution. The preservation of glassy melt inclusions without daughter crystals in zircons also implies rapid emplacement.

Magmatic volatiles and degassing: implications for mineralization

Magmatic volatiles play a key role in the mineralization of porphyritic intrusions. Metals such as copper, complexed with chlorine, along with sulfur necessary for ore formation are transported and concentrated by magmatic volatiles (Candela, 1997; Candela & Piccoli, 2005; Cline & Bodnar, 1991; Heinrich, 2005; Redmond *et al.*, 2004; Tattitch *et al.*, 2015; Ulrich *et al.*, 2002, Tattitch & Blundy 2017). The DMIC is a clear example of the strong association of wet magmas with PCD formation (Chiaradia, 2015; Loucks, 2014; Richards, 2011; Williamson *et al.*, 2016). The adakitic character of the DMIC magmas, here attributed to amphibole fractionation, is consistent with other wet magmatic systems associated with porphyries and cryptic amphibole fractionation (Castillo, 2012; Chiaradia, 2015; Richards & Kerrich, 2007).

Several models have been proposed for magmatic fluids that source mineralization. The majority of models envisage a single composition fluid derived from a large-volume, shallow, usually felsic

magma reservoir (Candela & Holland, 1984; Candela & Piccoli, 2005; Cline & Bodnar, 1991; Cloos, 2001; Cooke *et al.*, 2015; Huber *et al.*, 2012; Landtwing *et al.*, 2005; Seedorff *et al.*, 2005; Sillitoe, 2010; Weis *et al.*, 2012). Some models have also implicated the role of more mafic magma in supplying sulfur-rich volatiles (Audétat *et al.*, 2004; Blundy *et al.*, 2015; De Hoog *et al.*, 2004; Halter *et al.*, 2005; Heinrich, 2005; Keith *et al.*, 1997; Maughan *et al.*, 2002; Nadeau *et al.*, 2010; Pollard *et al.*, 2005; Sinclair, 2007; Tapster *et al.*, 2016; Zajacz *et al.*, 2009). Blundy *et al.*, (2015) have invoked mixing of two different fluids, one being a metal-bearing brine precursor derived from felsic magma which accumulates in the ore zone over a long period and the other a sulfur-rich fluid which is derived from deeper-seated mafic magmas. Another model, favored by Streck & Dilles (1998) and Chambefort *et al.*, (2008), emphasizes the oxidized character of the magma and suggests that while sulfur may be sourced from mafic magmas initially, it is stored in the felsic magma as anhydrite crystals. Because anhydrite's solubility in H_2O increases with decreasing temperature, sulfur will be remobilized.

Our observations at DMIC provide some constraints on these models. The DMIC data, particularly from apatites, are consistent with decoupling of S and Cl during degassing. In wet magmas, H_2O may begin degassing in the mid-crust if crystallization is sufficient to drive residual melts to the point of saturation; degassing continues as the magma moves upward through the crust until emplacement. The melt and volatiles are likely decoupled physically and different volatile species degas at different depths (Christopher *et al.*, 2015). Apatites in DMP basaltic andesites have little S, but high Cl contents. The S contents of apatites from the biotite tonalite and IPD2s, however, can be much higher, up to ~3700 and ~2600 ppm S, respectively (Fig. 11). The depth at which sulfur begins to degas is a function of the exsolved fluid fraction and the pressure for a particular oxygen fugacity (Keppler, 2010). Thus, H_2O solubility in magma has a profound influence on the depth at which sulfur begins to degas. Degassing of S from mafic magmas may represent the ultimate source of S required for copper sulfides (Blundy *et al.*, 2015).

The rapid decline in Cl content in DMIC amphiboles at temperatures around the granite solidus (680°-700°C) for water-saturated haplogranite system (Johannes & Holtz, 2012) (Fig. 17a) and the lower Cl content of apatite microphenocrysts compared with apatite inclusions in the biotite tonalite suggest the possibility of late-stage exsolution of a hypersaline fluid. The biotite tonalite and the other DMIC silicic units show evidence of storage at temperatures at or near the granite solidus. The development of this "proto-ore" fluid may have been essential for porphyry copper mineralization. Because brines can persist long after crystallization has ceased, mineralization may occur later during subsequent fluxing of S-rich gasses (sourced from the mafic magmas) through the system (Blundy *et al.*, 2015) or remobilization of SO_2 from dissolution of anhydrite (Dilles *et al.*, 2015, Streck & Dilles, 1998).

CONCLUSIONS

(1) High initial H_2O content is suggested for the DMIC magmas (H_2O > 4%). The DMIC silicic magmas likely originated from parental magmas with the deepest differentiation depths. Plagioclase was likely suppressed in these magmas resulting in a high-Sr trend observed in plagioclase. Shallower differentiation depths for the parental magmas of the more mafic DMIC units resulted in a low-Sr trend observed in the plagioclase from these units.

(2) Polybaric differentiation in the DMIC is documented by the wide range of amphibole compositions and geochemical signatures consistent with cryptic amphibole fractionation. Comparison with experimental data suggests that amphibole in the DMIC system may have begun crystallizing in the mid- to lower crust and continued to shallow levels.

(3) Detailed study of plagioclase and amphibole from the DMIC indicates the magmas related to IPDs formed due to hybridization, magma mingling, and decompression crystallization of magma sources that stalled and differentiated at different depths within the crust. In addition, disruption and entrainment of mush and cumulate crystals, like the gabbroic xenolith, contributes to the overall petrological

heterogeneity observed in these rocks. The DMIC demonstrates the level of complexity resulting from open system behavior in vertically extensive magmatic systems.

(4) The isotopic signature for the DMIC is consistent with other rocks in this segment of the Andes.

(5) Variable degassing and decoupling of volatile components is inferred for the different DMIC units based on apatite S and Cl contents. Since sulfur may begin degassing deep, this decoupling provides evidence that mafic magmas may have been the source of sulfur for DMIC copper mineralization, whereas shallow-exsolved, near-solidus, Cl-rich fluids provided the transport mechanism for copper.

(6) Finally, the coherent petrologic story of the DMIC may be uniquely preserved because it is hypabyssal. In the hypabyssal environment the protracted cooling and complete reequilibration of plutonic systems is avoided, as is the premature quenching observed in volcanic products. The hypabyssal environment thus captures the intrusive to eruptive transition in unprecedented detail.

ACKNOWLEDGEMENTS

This work was conducted as part of the senior author's Ph.D. research at the University of Bristol, which was funded by BHP as part of the Bristol PCD Project. The U-Pb geochronology and zircon trace element work was funded by a NERC NIGL/AIF grant IP-1415-1113. BHP is also thanked for providing logistical support in the field and access to the samples. We thank Stuart Kearns and Ben Buse (University of Bristol) and Iain McDonald (University of Cardiff) for help with the microprobe data acquisition. Simon Chenery at the NERC Isotope Geosciences Laboratory, British Geological Survey are thanked for their assistance during LA-ICP-MS zircon trace element analyses at the BGS, Keyworth. Marit van Zalinge, Vladimir Matjuschkin and Bob Loucks are thanked for their insightful conversations and detailed critiques. The manuscript has benefited greatly from the thorough and constructive reviews by James Mungall, Cam McCuaig and an anonymous reviewer.

FUNDING

Funding for this research comes from BHP as part of the Bristol PCD Project grant. The trace element and Hf isotope zircon work was funded by a NERC NIGL/AIF grant IP-1415-1113.

REFERENCES

Andersen, D. J. & Lindsley, D. H. (1985). New (and final!) models for the Ti-magnetite/ilmenite geothermometer and oxygen barometer. *Abstracts of American Geophysical Union 1985 Spring Meeting*. American Geophysical Union.

Anderson, J. L., Barth, A. P., Wooden, J. L. & Mazdab, F. (2008). Thermometers and thermobarometers in granitic systems. *Reviews in Mineralogy and Geochemistry*. Mineralogical Society of America **69**, 121–142.

Annen, C., Blundy, J. D., Leuthold, J. & Sparks, R. S. J. (2015). Construction and evolution of igneous bodies: Towards an integrated perspective of crustal magmatism. *Lithos*. Elsevier **230**, 206–221.

Annen, C., Blundy, J. D. & Sparks, R. S. J. (2005). The genesis of intermediate and silicic magmas in deep crustal hot zones. *Journal of Petrology*. Oxford University Press **47**, 505–539.

Audétat, A., Pettke, T. & Dolejš, D. (2004). Magmatic anhydrite and calcite in the ore-forming quartz-monzodiorite magma at Santa Rita, New Mexico (USA): genetic constraints on porphyry-Cu mineralization. *Lithos*. Elsevier **72**, 147–161.

Bach, W., Hegner, E., Erzinger, J. & Satir, M. (1994). Chemical and isotopic variations along the superfast spreading East Pacific Rise from 6 to 30 S. *Contributions to Mineralogy and Petrology*. Springer **116**, 365–380.

Bachmann, O. & Bergantz, G. W. (2006). Gas percolation in upper-crustal silicic crystal mushes as a mechanism for upward heat advection and rejuvenation of near-solidus magma bodies. *Journal of Volcanology and Geothermal research*. Elsevier **149**, 85–102.

Bacon, C. R. & Hirschmann, M. M. (1988). Mg/Mn partitioning as a test for equilibrium between coexisting Fe-Ti oxides. *American Mineralogist* **73**, 57–61.

Bergantz, G. W., Schleicher, J. M. & Burgisser, A. (2015). Open-system dynamics and mixing in magma mushes. *Nature Geoscience*. Nature Research **8**, 793–796.

Blundy, J. & Cashman, K. (2001). Ascent-driven crystallisation of dacite magmas at Mount St Helens, 1980-1986. *Contributions to Mineralogy and Petrology*. Springer **140**, 631–650.

Blundy, J. & Cashman, K. (2008). Petrologic reconstruction of magmatic system variables and processes. *Reviews in Mineralogy and Geochemistry*. Mineral Soc America **69**, 179–239.

Blundy, J. D. & Wood, B. J. (1991). Crystal-chemical controls on the partitioning of Sr and Ba between plagioclase feldspar, silicate melts, and hydrothermal solutions. *Geochimica et Cosmochimica Acta*. Elsevier **55**, 193–209.

Blundy, J., Mavrogenes, J., Tattitch, B., Sparks, S. & Gilmer, A. (2015). Generation of porphyry copper

deposits by gas-brine reaction in volcanic arcs. *Nature Geoscience*. Nature Research **8**, 235–240.

Boyce, J. W. & Hervig, R. L. (2008). Magmatic degassing histories from apatite volatile stratigraphy. *Geology*. Geological Society of America **36**, 63–66.

Boyce, J. W. & Hervig, R. L. (2009). Apatite as a monitor of late-stage magmatic processes at Volcán Irazú, Costa Rica. *Contributions to Mineralogy and Petrology*. Springer **157**, 135.

Candela, P. A. (1997). A review of shallow, ore-related granites: textures, volatiles, and ore metals. *Journal of petrology*. Oxford University Press **38**, 1619–1633.

Candela, P. A. & Holland, H. D. (1984). The partitioning of copper and molybdenum between silicate melts and aqueous fluids. *Geochimica et Cosmochimica Acta*. Elsevier **48**, 373–380.

Candela, P. A. & Piccoli, P. M. (2005). Magmatic processes in the development of porphyry-type ore systems. *Economic Geology* **100**, 25–37.

Candia, W., Oviedo, O. & Nuñez, E. (2009). *Don Manuel Project Seasonal Report 2009*. .

Carroll, M. R. & Rutherford, M. J. (1987). The stability of igneous anhydrite: experimental results and implications for sulfur behavior in the 1982 El Chichon trachyandesite and other evolved magmas. *Journal of Petrology*. Oxford University Press **28**, 781–801.

Cashman, K. V & Giordano, G. (2014). Calderas and magma reservoirs. *Journal of Volcanology and Geothermal Research*. Elsevier **288**, 28–45.

Cashman, K. V, Sparks, R. S. J. & Blundy, J. D. (2017). Vertically extensive and unstable magmatic systems: A unified view of igneous processes. *Science* **355**.

Castillo, P. R. (2012). Adakite petrogenesis. *Lithos*. Elsevier **134**, 304–316.

Chambefort, I., Dilles, J. H. & Kent, A. J. R. (2008). Anhydrite-bearing andesite and dacite as a source for sulfur in magmatic-hydrothermal mineral deposits. *Geology*. Geological Society of America **36**, 719–722.

Charlier, B. L. A., Wilson, C. J. N., Lowenstern, J. B., Blake, S., Van Calsteren, P. W. & Davidson, J. P. (2004). Magma generation at a large, hyperactive silicic volcano (Taupo, New Zealand) revealed by U–Th and U–Pb systematics in zircons. *Journal of Petrology*. Oxford University Press **46**, 3–32.

Charrier, R., Baeza, O., Elgueta, S., Flynn, J. J., Gans, P., Kay, S. M., Muñoz, N., Wyss, A. R. & Zurita, E. (2002). Evidence for Cenozoic extensional basin development and tectonic inversion south of the flat-slab segment, southern Central Andes, Chile (33–36 SL). *Journal of South American Earth Sciences*. Elsevier **15**, 117–139.

Charrier, R., Wyss, A., Flynn, J. J., Swisher, C. C., Norell, M. A., Zapatta, F., McKenna, M. C. & Novacek, M. J. (1996). New evidence for late Mesozoic-early Cenozoic evolution of the Chilean Andes in the upper Tinguiririca valley (35 S), central Chile. *Journal of South American Earth Sciences*. Elsevier **9**, 393–422.

Cherniak, D. J. & Watson, E. B. (1994). A study of strontium diffusion in plagioclase using Rutherford backscattering spectroscopy. *Geochimica et Cosmochimica Acta*. Elsevier **58**, 5179–5190.

Chiaradia, M. (2015). Crustal thickness control on Sr/Y signatures of recent arc magmas: an Earth scale perspective. *Scientific reports*. Nature Publishing Group **5**.

Christopher, T. E., Blundy, J., Cashman, K., Cole, P., Edmonds, M., Smith, P. J., Sparks, R. S. J. & Stinton, A. (2015). Crustal-scale degassing due to magma system destabilization and magma-gas

decoupling at Soufrière Hills Volcano, Montserrat. *Geochemistry, Geophysics, Geosystems*. Wiley Online Library **16**, 2797–2811.

Claiborne, L. L., Miller, C. F., Walker, B. A., Wooden, J. L., Mazdab, F. K. & Bea, F. (2006). Tracking magmatic processes through Zr/Hf ratios in rocks and Hf and Ti zoning in zircons: an example from the Spirit Mountain batholith, Nevada. *Mineralogical Magazine* **70**, 517–543.

Claiborne, L. L., Miller, C. F. & Wooden, J. L. (2010). Trace element composition of igneous zircon: a thermal and compositional record of the accumulation and evolution of a large silicic batholith, Spirit Mountain, Nevada. *Contributions to Mineralogy and Petrology*. Springer **160**, 511–531.

Cline, J. S. & Bodnar, R. J. (1991). Can economic porphyry copper mineralization be generated by a typical calc-alkaline melt? *Journal of Geophysical Research: Solid Earth*. Wiley Online Library **96**, 8113–8126.

Cloos, M. (2001). Bubbling magma chambers, cupolas, and porphyry copper deposits. *International Geology Review*. Taylor & Francis **43**, 285–311.

Clynne, M. A. (1999). A complex magma mixing origin for rocks erupted in 1915, Lassen Peak, California. *Journal of Petrology*. Oxford University Press **40**, 105–132.

Cooke, D. R., Braxton, D. P., White, N. C. & Rinne, M. (2015). Metal transport and ore deposition in porphyry copper±gold±molybdenum deposits-contrasting behaviour between deep and shallow environments. *Society for Geology Applied to Mineral Deposits Conference 2015*, 275–278.

Cooper, G. F. & Wilson, C. J. N. (2014). Development, mobilisation and eruption of a large crystal-rich rhyolite: The Ongatiti ignimbrite, New Zealand. *Lithos*. Elsevier **198**, 38–57.

Cooper, K. M. & Reid, M. R. (2003). Re-examination of crystal ages in recent Mount St. Helens lavas: implications for magma reservoir processes. *Earth and Planetary Science Letters*. Elsevier **213**, 149–167.

Costa, F., Scaillet, B. & Pichavant, M. (2004). Petrological and experimental constraints on the pre-eruption conditions of Holocene dacite from Volcán San Pedro (36 S, Chilean Andes) and the importance of sulphur in silicic subduction-related magmas. *Journal of Petrology*. Oxford University Press **45**, 855–881.

Czamanske, G. K. & Wones, D. R. (1973). Oxidation during magmatic differentiation, Finnmarka complex, Oslo area, Norway: Part 2, the mafic silicates1. *Journal of Petrology*.

Davidson, J. P., Hora, J. M., Garrison, J. M. & Dungan, M. A. (2005). Crustal forensics in arc magmas. *Journal of Volcanology and Geothermal Research*. Elsevier **140**, 157–170.

Davidson, J., Turner, S., Handley, H., Macpherson, C. & Dosseto, A. (2007). Amphibole "sponge" in arc crust? *Geology*. Geological Society of America **35**, 787–790.

De Hoog, J. C. M., Hattori, K. H. & Hoblitt, R. P. (2004). Oxidized sulfur-rich mafic magma at Mount Pinatubo, Philippines. *Contributions to Mineralogy and Petrology*. Springer **146**, 750–761.

Deckart, K., Godoy, E., Bertens, A., Jerez, D. & Saeed, A. (2010). Barren Miocene granitoids in the Central Andean metallogenic belt, Chile: Geochemistry and Nd-Hf and U-Pb isotope systematics. *Andean Geology*. Servicio Nacional de Geología y Minería **37**.

Dietterich, H. & de Silva, S. (2010). Sulfur yield of the 1600 eruption of Huaynaputina, Peru: Contributions from magmatic, fluid-phase, and hydrothermal sulfur. *Journal of Volcanology and Geothermal Research*. Elsevier **197**, 303–312.

Dilles, J. H., Kent, A. J. R., Wooden, J. L., Tosdal, R. M., Koleszar, A., Lee, R. G. & Farmer, L. P. (2015). Zircon compositional evidence for sulfur-degassing from ore-forming arc magmas. *Economic Geology*. SecG **110**, 241–251.

Doherty, A. L., Webster, J. D., Goldoff, B. A. & Piccoli, P. M. (2014). Partitioning behavior of chlorine and fluorine in felsic melt–fluid (s)–apatite systems at 50MPa and 850–950° C. *Chemical Geology*. Elsevier **384**, 94–111.

Dohmen, R. & Blundy, J. (2014). A predictive thermodynamic model for element partitioning between plagioclase and melt as a function of pressure, temperature and composition. *American Journal of Science*. American Journal of Science **314**, 1319–1372.

Dohmen, R., Faak, K. & Blundy, J. D. (2017). Chronometry and speedometry of magmatic processes using chemical diffusion in olivine, plagioclase and pyroxenes. *Reviews in Mineralogy and Geochemistry*. GeoScienceWorld **83**, 535–575.

Douglass, J., Schilling, J. & Fontignie, D. (1999). Plume-ridge interactions of the Discovery and Shona mantle plumes with the southern Mid-Atlantic Ridge (40°-55° S). *Journal of Geophysical Research: Solid Earth*. Wiley Online Library **104**, 2941–2962.

Druitt, T. H. & Bacon, C. R. (1989). Petrology of the zoned calcalkaline magma chamber of Mount Mazama, Crater Lake, Oregon. *Contributions to Mineralogy and Petrology*. Springer **101**, 245–259.

Dungan, M. A. & Davidson, J. (2004). Partial assimilative recycling of the mafic plutonic roots of arc volcanoes: An example from the Chilean Andes. *Geology*. Geological Society of America **32**, 773–776.

Economos, R., Boehnke, P. & Burgisser, A. (2017). Sulfur isotopic zoning in apatite crystals: A new record of dynamic sulfur behavior in magmas. *Geochimica et Cosmochimica Acta*. Elsevier **215**, 387–403.

Edmonds, M., Kohn, S. C., Hauri, E. H., Humphreys, M. C. S. & Cassidy, M. (2016). Extensive, water-rich magma reservoir beneath southern Montserrat. *Lithos*. Elsevier **252**, 216–233.

Eichelberger, J. C. (1975). Origin of andesite and dacite: evidence of mixing at Glass Mountain in California and at other circum-Pacific volcanoes. *Geological Society of America Bulletin*. Geological Society of America **86**, 1381–1391.

Farías, M., Charrier, R., Carretier, S., Martinod, J., Fock, A., Campbell, D., Caceres, J. & Comte, D. (2008). Late Miocene high and rapid surface uplift and its erosional response in the Andes of central Chile (33–35 S). *Tectonics*. Wiley Online Library **27**.

Farías, M., Comte, D., Charrier, R., Martinod, J., David, C., Tassara, A., Tapia, F. & Fock, A. (2010). Crustal-scale structural architecture in central Chile based on seismicity and surface geology: Implications for Andean mountain building. *Tectonics*. Wiley Online Library **29**.

Ferry, J. M. & Watson, E. B. (2007). New thermodynamic models and revised calibrations for the Ti-in-zircon and Zr-in-rutile thermometers. *Contributions to Mineralogy and Petrology*. Springer **154**, 429–437.

Fiege, A., Behrens, H., Holtz, F. & Adams, F. (2014a). Kinetic vs. thermodynamic control of degassing of H_2O–S±Cl-bearing andesitic melts. *Geochimica et Cosmochimica Acta*. Elsevier **125**, 241–264.

Fiege, A., Holtz, F. & Cichy, S. B. (2014b). Bubble formation during decompression of andesitic melts. .

Futa, K. & Stern, C. R. (1988). Sr and Nd isotopic and trace element compositions of Quaternary volcanic centers of the southern Andes. *Earth and Planetary Science Letters*. Elsevier **88**, 253–262.

Giambiagi, L. B., Alvarez, P. P., Godoy, E. & Ramos, V. A. (2003a). The control of pre-existing extensional structures on the evolution of the southern sector of the Aconcagua fold and thrust belt, southern Andes. *Tectonophysics*. Elsevier **369**, 1–19.

Giambiagi, L. B. & Ramos, V. A. (2002). Structural evolution of the Andes in a transitional zone between flat and normal subduction (33 30′–33 45′ S), Argentina and Chile. *Journal of South American Earth Sciences*. Elsevier **15**, 101–116.

Giambiagi, L. B., Ramos, V. A., Godoy, E., Alvarez, P. P. & Orts, S. (2003b). Cenozoic deformation and tectonic style of the Andes, between 33 and 34 south latitude. *Tectonics*. Wiley Online Library **22**.

Gilbert, H., Beck, S. & Zandt, G. (2006). Lithospheric and upper mantle structure of central Chile and Argentina. *Geophysical Journal International*. Blackwell Publishing Ltd Oxford, UK **165**, 383–398.

Gill, J., Reagan, M., Tepley, F. & Malavassi, E. (2006). Arenal Volcano, Costa Rica: Magma genesis and volcanological processes-Introduction. ELSEVIER SCIENCE BV PO BOX 211, 1000 AE AMSTERDAM, NETHERLANDS.

Gilmer, A. K., Sparks, R. S. J., Rust, A. C., Tapster, S., Webb, A. D. & Barfod, D. N. (2017). Geology of the Don Manuel igneous complex, central Chile: Implications for igneous processes in porphyry copper systems. *Geological Society of America Bulletin*. Geological Society of America B31524-1.

Godoy, E., Yáñez, G. & Vera, E. (1999). Inversion of an Oligocene volcano-tectonic basin and uplifting of its superimposed Miocene magmatic arc in the Chilean Central Andes: first seismic and gravity evidences. *Tectonophysics*. Elsevier **306**, 217–236.

Gualda, G. A. R., Ghiorso, M. S., Lemons, R. V & Carley, T. L. (2012). Rhyolite-MELTS: a modified calibration of MELTS optimized for silica-rich, fluid-bearing magmatic systems. *Journal of Petrology*. Oxford University Press **53**, 875–890.

Haase, K. M. (2002). Geochemical constraints on magma sources and mixing processes in Easter Microplate MORB (SE Pacific): a case study of plume–ridge interaction. *Chemical Geology*. Elsevier **182**, 335–355.

Halter, W. E., Heinrich, C. A. & Pettke, T. (2005). Magma evolution and the formation of porphyry Cu–Au ore fluids: evidence from silicate and sulfide melt inclusions. *Mineralium Deposita*. Springer **39**, 845–863.

Harrington, R. (1989). The Diamante Caldera and Maipo Caldera complex in the southern Andes of Argentina and Chile (24 10'South). *Revista de la Asociación Geológica Argentina*. Asociación Geológica Argentina. **19**, 186–193.

Heinrich, C. A. (2005). The physical and chemical evolution of low-salinity magmatic fluids at the porphyry to epithermal transition: a thermodynamic study. *Mineralium Deposita*. Springer **39**, 864–889.

Hernandez, L. B. & Rabbia, O. M. (2009). Apatite Chemistry in a Felsic Magmatic System From the El Teniente District (Chile) as Monitor of an Early, Single-phase, Cl and S-rich Magmatic Volatile Phase Evolution. *AGU Spring Meeting Abstracts*.

Hildreth, W. (2004). Volcanological perspectives on Long Valley, Mammoth Mountain, and Mono

Craters: several contiguous but discrete systems. *Journal of Volcanology and Geothermal Research*. Elsevier **136**, 169–198.

Hildreth, W. & Moorbath, S. (1988). Crustal contributions to arc magmatism in the Andes of central Chile. *Contributions to mineralogy and petrology*. Springer **98**, 455–489.

Hildreth, W. & Wilson, C. J. N. (2007). Compositional zoning of the Bishop Tuff. *Journal of Petrology*. Oxford University Press **48**, 951–999.

Hoernle, K. *et al.* (2008). Arc-parallel flow in the mantle wedge beneath Costa Rica and Nicaragua. *Nature*. Nature Publishing Group **451**, 1094–1097.

Holm, P. M., Søager, N., Dyhr, C. T. & Nielsen, M. R. (2014). Enrichments of the mantle sources beneath the Southern Volcanic Zone (Andes) by fluids and melts derived from abraded upper continental crust. *Contributions to Mineralogy and Petrology*. Springer **167**, 1004.

Huber, C., Bachmann, O., Vigneresse, J., Dufek, J. & Parmigiani, A. (2012). A physical model for metal extraction and transport in shallow magmatic systems. *Geochemistry, Geophysics, Geosystems*. Wiley Online Library **13**.

Humphreys, M. C. S., Christopher, T. & Hards, V. (2009). Microlite transfer by disaggregation of mafic inclusions following magma mixing at Soufrière Hills volcano, Montserrat. *Contributions to Mineralogy and Petrology*. Springer **157**, 609–624.

Imai, A. (2004). Variation of Cl and SO3 contents of microphenocrystic apatite in intermediate to silicic igneous rocks of Cenozoic Japanese island arcs: Implications for porphyry Cu metallogenesis in the Western Pacific Island arcs. *Resource Geology*. Wiley Online Library **54**, 357–372.

Jagoutz, O., Müntener, O., Schmidt, M. W. & Burg, J.-P. (2011). The roles of flux-and decompression melting and their respective fractionation lines for continental crust formation: Evidence from the Kohistan arc. *Earth and Planetary Science Letters*. Elsevier **303**, 25–36.

Jerram, D. A. & Martin, V. M. (2008). Understanding crystal populations and their significance through the magma plumbing system. *Geological Society, London, Special Publications*. Geological Society of London **304**, 133–148.

Jochum, K. P., Hofmann, A. W. & Seufert, H. M. (1993). Tin in mantle-derived rocks: constraints on Earth evolution. *Geochimica et Cosmochimica Acta*. Elsevier **57**, 3585–3595.

Johannes, W. & Holtz, F. (2012). *Petrogenesis and experimental petrology of granitic rocks*. Springer Science & Business Media.

Kay, S. M., Godoy, E. & Kurtz, A. (2005). Episodic arc migration, crustal thickening, subduction erosion, and magmatism in the south-central Andes. *Geological Society of America Bulletin*. Geological Society of America **117**, 67–88.

Kay, S. M. & Mpodozis, C. (2001). Central Andean ore deposits linked to evolving shallow subduction systems and thickening crust. *GSA today*. Geological Society of America **11**, 4–9.

Keith, J. D., Whitney, J. A., Hattori, K., Ballantyne, G. H., Christiansen, E. H., Barr, D. L., Cannan, T. M. & Hook, C. J. (1997). The role of magmatic sulfides and mafic alkaline magmas in the Bingham and Tintic mining districts, Utah. *Journal of Petrology*. Oxford University Press **38**, 1679–1690.

Keppler, H. (2010). The distribution of sulfur between haplogranitic melts and aqueous fluids. *Geochimica et Cosmochimica Acta*. Elsevier **74**, 645–660.

Kress, V. C. & Carmichael, I. S. E. (1991). The compressibility of silicate liquids containing Fe_2O_3 and

the effect of composition, temperature, oxygen fugacity and pressure on their redox states. *Contributions to Mineralogy and Petrology*. Springer **108**, 82–92.

Kurtz, A. C., Kay, S. M., Charrier, R. & Farrar, E. (1997). Geochronology of Miocene plutons and exhumation history of the El Teniente region, Central Chile (34-35 8). *Andean Geology* **24**, 75–90.

Landtwing, M. R., Pettke, T., Halter, W. E., Heinrich, C. A., Redmond, P. B., Einaudi, M. T. & Kunze, K. (2005). Copper deposition during quartz dissolution by cooling magmatic–hydrothermal fluids: the Bingham porphyry. *Earth and Planetary Science Letters*. Elsevier **235**, 229–243.

Le Maitre, R. W. *et al.* (2002). Igneous rocks: A classification and glossary of terms; Recommendations of the International Union of Geological Sciences. *Subcommission on the Systematics of Igneous rocks*. Cambridge University Press.

Lepage, L. D. (2003). ILMAT: an Excel worksheet for ilmenite–magnetite geothermometry and geobarometry. *Computers & Geosciences*. Pergamon **29**, 673–678.

Lesne, P., Kohn, S. C., Blundy, J., Witham, F., Botcharnikov, R. E. & Behrens, H. (2011). Experimental simulation of closed-system degassing in the system basalt–H2O–CO2–S–Cl. *Journal of Petrology*. Oxford University Press **52**, 1737–1762.

Liu, Y., Zhang, Y. & Behrens, H. (2005). Solubility of H 2 O in rhyolitic melts at low pressures and a new empirical model for mixed H 2 O–CO 2 solubility in rhyolitic melts. *Journal of Volcanology and Geothermal Research*. Elsevier **143**, 219–235.

Loucks, R. R. (2014). Distinctive composition of copper-ore-forming arcmagmas. *Australian Journal of Earth Sciences*. Taylor & Francis **61**, 5–16.

Lu, Y.-J. *et al.* (2016). Zircon compositions as a pathfinder for porphyry Cu±Mo±Au deposits. *Economic Geology Special Publication* **19**, 329–347.

Luhr, J. F. (2008). Primary igneous anhydrite: Progress since its recognition in the 1982 El Chichón trachyandesite. *Journal of Volcanology and Geothermal Research*.

Luhr, J. F. (1990). Experimental phase relations of water-and sulfur-saturated arc magmas and the 1982 eruptions of El Chichón volcano. *Journal of Petrology*. Oxford University Press **31**, 1071–1114.

Macdougall, J. D. & Lugmair, G. W. (1985). Extreme isotopic homogeneity among basalts from the southern East Pacific Rise: mantle or mixing effect? *Nature*. Springer **313**, 209–211.

Marot, M., Monfret, T., Gerbault, M., Nolet, G., Ranalli, G. & Pardo, M. (2014). Flat versus normal subduction zones: a comparison based on 3-D regional traveltime tomography and petrological modelling of central Chile and western Argentina (29–35 S). *Geophysical Journal International*. Oxford University Press **199**, 1633–1654.

Matjuschkin, V., Blundy, J. D. & Brooker, R. A. (2016). The effect of pressure on sulphur speciation in mid-to deep-crustal arc magmas and implications for the formation of porphyry copper deposits. *Contributions to Mineralogy and Petrology*. Springer **171**, 1–25.

Maughan, D. T., Keith, J. D., Christiansen, E. H., Pulsipher, T., Hattori, K. & Evans, N. J. (2002). Contributions from mafic alkaline magmas to the Bingham porphyry Cu-Au-Mo deposit, Utah, USA. *Mineralium Deposita*. Springer **37**, 14–37.

Melekhova, E., Annen, C. & Blundy, J. (2013). Compositional gaps in igneous rock suites controlled by magma system heat and water content. *Nature Geoscience*. Nature Research **6**, 385–390.

Montecinos, P., Schärer, U., Vergara, M. & Aguirre, L. (2008). Lithospheric origin of Oligocene–

Miocene magmatism in Central Chile: U–Pb ages and Sr–Pb–Hf isotope composition of minerals. *Journal of Petrology*. Oxford University Press **49**, 555–580.

Moore, G. & Carmichael, I. S. E. (1998). The hydrous phase equilibria (to 3 kbar) of an andesite and basaltic andesite from western Mexico: constraints on water content and conditions of phenocryst growth. *Contributions to Mineralogy and Petrology*. Springer **130**, 304–319.

Mpodozis, C., Ramos, V. A., Ericksen, G. E., Cañas, M. T. & Reinemund, J. A. (1990). Geology of the Andes and its Relation to Hydrocarbon and Energy Resources. *Geology of the Andes and its Relation to Hydrocarbon and Energy Resources*. Circum-Pacific Council for Energy and Hydrothermal ResourcesAmerican Association of Petroleum Geologists Houston^ eTexas **11**.

Munoz, M., Charrier, R., Fanning, C. M., Maksaev, V. & Deckart, K. (2012). Zircon trace element and O–Hf isotope analyses of mineralized intrusions from El Teniente ore deposit, Chilean Andes: constraints on the source and magmatic evolution of porphyry Cu–Mo related magmas. *Journal of Petrology*. Oxford University Press **53**, 1091–1122.

Muñoz, M., Farías, M., Charrier, R., Fanning, C. M., Polvé, M. & Deckart, K. (2013). Isotopic shifts in the Cenozoic Andean arc of central Chile: Records of an evolving basement throughout cordilleran arc mountain building. *Geology*. Geological Society of America **41**, 931–934.

Muñoz, M., Fuentes, F., Vergara, M., Aguirr, L., Olov Nyström, J., Féraud, G. & Demant, A. (2006). Abanico East Formation: petrology and geochemistry of volcanic rocks behind the Cenozoic arc front in the Andean Cordillera, central Chile (33 50'S). *Revista geológica de Chile*. SciELO Chile **33**, 109–140.

Müntener, O., Kelemen, P. B. & Grove, T. L. (2001). The role of H2O during crystallization of primitive arc magmas under uppermost mantle conditions and genesis of ... The role of H 2 O during crystallization of primitive arc magmas under uppermost mantle conditions and genesis. *Contributions to Mineralogy and Petrology*.

Murphy, M. D., Sparks, R. S. J., Barclay, J., Carroll, M. R., Lejeune, A., Brewer, T. S., MacDonald, R., Black, S. & Young, S. (1998). The role of magma mixing in triggering the current eruption at the Soufriere Hills volcano, Montserrat, West Indies. *Geophysical Research Letters*. Wiley Online Library **25**, 3433–3436.

Mutch, E. J. F., Blundy, J. D., Tattitch, B. C., Cooper, F. J. & Brooker, R. A. (2016). An experimental study of amphibole stability in low-pressure granitic magmas and a revised Al-in-hornblende geobarometer. *Contributions to Mineralogy and Petrology*. Springer **171**, 85.

Nacif, S., Triep, E. G., Spagnotto, S. L., Aragon, E., Furlani, R. & Álvarez, O. (2015). The flat to normal subduction transition study to obtain the Nazca plate morphology using high resolution seismicity data from the Nazca plate in Central Chile. *Tectonophysics*. Elsevier **657**, 102–112.

Nadeau, O., Stix, J. & Williams-Jones, A. E. (2016). Links between arc volcanoes and porphyry-epithermal ore deposits. *Geology*. Geological Society of America **44**, 11–14.

Nadeau, O., Williams-Jones, A. E. & Stix, J. (2010). Sulphide magma as a source of metals in arc-related magmatic hydrothermal ore fluids. *Nature Geoscience*. Nature Publishing Group **3**, 501–505.

Newman, S. & Lowenstern, J. B. (2002). VolatileCalc: a silicate melt–H2O–CO2 solution model written in Visual Basic for excel. *Computers & Geosciences*. Elsevier **28**, 597–604.

Nyström, J. O., Vergara, M., Morata, D. & Levi, B. (2003). Tertiary volcanism during extension in the

Andean foothills of central Chile (33 15′–33 45′ S). *Geological Society of America Bulletin*. Geological Society of America **115**, 1523–1537.

Özdemir, Y., Blundy, J. & Güleç, N. (2011). The importance of fractional crystallization and magma mixing in controlling chemical differentiation at Süphan stratovolcano, eastern Anatolia, Turkey. *Contributions to Mineralogy and Petrology*. Springer **162**, 573–597.

Pallister, J. S., Hoblitt, R. P., Meeker, G. P., Knight, R. J. & Siems, D. F. (1996). Magma mixing at Mount Pinatubo: petrographic and chemical evidence from the 1991 deposits. *Fire and mud: eruptions and lahars of Mount Pinatubo, Philippines*. PHIVOLCS and University of Washington, Seattle 687–731.

Parat, F., Dungan, M. A. & Streck, M. J. (2002). Anhydrite, pyrrhotite, and sulfur-rich apatite: tracing the sulfur evolution of an Oligocene andesite (Eagle Mountain, CO, USA). *Lithos*. Elsevier **64**, 63–75.

Parat, F. & Holtz, F. (2004). Sulfur partitioning between apatite and melt and effect of sulfur on apatite solubility at oxidizing conditions. *Contributions to Mineralogy and Petrology*. Springer **147**, 201–212.

Parat, F. & Holtz, F. (2005). Sulfur partition coefficient between apatite and rhyolite: the role of bulk S content. *Contributions to Mineralogy and Petrology*. Springer **150**, 643–651.

Pardo, M., Comte, D. & Monfret, T. (2002). Seismotectonic and stress distribution in the central Chile subduction zone. *Journal of South American Earth Sciences*. Elsevier **15**, 11–22.

Peng, G., Luhr, J. F. & McGee, J. J. (1997). Factors controlling sulfur concentrations in volcanic apatite. *American Mineralogist* **82**, 1210–1224.

Plank, T., Kelley, K. A., Zimmer, M. M., Hauri, E. H. & Wallace, P. J. (2013). Why do mafic arc magmas contain~ 4wt% water on average? *Earth and Planetary Science Letters*. Elsevier **364**, 168–179.

Pollard, P. J., Taylor, R. G. & Peters, L. (2005). Ages of intrusion, alteration, and mineralization at the Grasberg Cu-Au deposit, Papua, Indonesia. *Economic Geology*. SecG **100**, 1005–1020.

Portnyagin, M., Duggen, S., Hauff, F., Mironov, N., Bindeman, I., Thirlwall, M. & Hoernle, K. (2015). Geochemistry of the late Holocene rocks from the Tolbachik volcanic field, Kamchatka: Quantitative modelling of subduction-related open magmatic systems. *Journal of Volcanology and Geothermal Research* **307**, 133–155.

Prouteau, G. & Scaillet, B. (2003). Experimental constraints on the origin of the 1991 Pinatubo dacite. *Journal of Petrology*. Oxford University Press **44**, 2203–2241.

Ramos, V. A., Zapata, T., Cristallini, E. & Introcaso, A. (2004). The Andean Thrust SystemLatitudinal Variations in Structural Styles and Orogenic Shortening. AAPG Special Volumes.

Redmond, P. B., Einaudi, M. T., Inan, E. E., Landtwing, M. R. & Heinrich, C. A. (2004). Copper deposition by fluid cooling in intrusion-centered systems: New insights from the Bingham porphyry ore deposit, Utah. *Geology*. Geological Society of America **32**, 217–220.

Reubi, O. & Blundy, J. (2009). A dearth of intermediate melts at subduction zone volcanoes and the petrogenesis of arc andesites. *Nature*. Nature Publishing Group **461**, 1269–1273.

Richards, J. (2016). Economic geology: Clues to hidden copper deposits. *Nature Geoscience* **9**, 195.

Richards, J. P. (2011). HIGH Sr/Y ARC MAGMAS AND PORPHYRY Cu ± Mo ± Au DEPOSITS:

JUST ADD WATER. *Economic Geology* **106**, 1075–1081.

Richards, J. P. & Kerrich, R. (2007). Special paper: adakite-like rocks: their diverse origins and questionable role in metallogenesis. *Economic geology*. SecG **102**, 537–576.

Riker, J. M., Blundy, J. D., Rust, A. C., Botcharnikov, R. E. & Humphreys, M. C. S. (2015). Experimental phase equilibria of a Mount St. Helens rhyodacite: a framework for interpreting crystallization paths in degassing silicic magmas. *Contributions to Mineralogy and Petrology*. Springer **170**, 1–22.

Sato, H., Holtz, F., Behrens, H., Botcharnikov, R. & Nakada, S. (2005). Experimental Petrology of the 1991–1995 Unzen Dacite, Japan. Part II: Cl/OH Partitioning between Hornblende and Melt and its Implications for the Origin of Oscillatory Zoning of Hornblende Phenocrysts. *Journal of Petrology* **46**, 339–354.

Scaillet, B., Clemente, B., Evans, B. W. & Pichavant, M. (1998). Redox control of sulfur degassing in silicic magmas. *Journal of Geophysical Research: Solid Earth*. Wiley Online Library **103**, 23937–23949.

Scaillet, B. & Evans, B. W. (1999). The 15 June 1991 eruption of Mount Pinatubo. I. Phase equilibria and pre-eruption P–T–f O2–f H2O conditions of the dacite magma. *Journal of Petrology*. Oxford University Press **40**, 381–411.

Scott, J. A. J., Humphreys, M. C. S., Mather, T. A., Pyle, D. M. & Stock, M. J. (2015). Insights into the behaviour of S, F, and Cl at Santiaguito Volcano, Guatemala, from apatite and glass. *Lithos*. Elsevier **232**, 375–394.

Seedorff, E., Dilles, J. H., Proffett, J. M., Einaudi, M. T., Zurcher, L., Stavast, W. J. A., Johnson, D. A. & Barton, M. D. (2005). Porphyry deposits: Characteristics and origin of hypogene features. *Economic Geology 100th anniversary volume*. Society of Economic Geologists Inc. Littleton, Colorado **29**, 251–298.

Sillitoe, R. H. (2010). Porphyry copper systems. *Economic geology*. SecG **105**, 3–41.

Sinclair, W. D. (2007). Porphyry deposits. *Mineral deposits of Canada: A synthesis of major deposit-types, district metallogeny, the evolution of geological provinces, and exploration methods: Geological Association of Canada, Mineral Deposits Division, Special Publication* **5**, 223–243.

Sisson, T. W. & Grove, T. L. (1993). Temperatures and H 2 O contents of low-MgO high-alumina basalts. *Contributions to Mineralogy and Petrology*. Springer **113**, 167–184.

Skewes, M. A. & Stern, C. R. (1995). Genesis of the giant late Miocene to Pliocene copper deposits of central Chile in the context of Andean magmatic and tectonic evolution. *International Geology Review*. Taylor & Francis **37**, 893–909.

Solano, J. M. S., Jackson, M. D., Sparks, R. S. J., Blundy, J. D. & Annen, C. (2012). Melt segregation in deep crustal hot zones: a mechanism for chemical differentiation, crustal assimilation and the formation of evolved magmas. *Journal of Petrology*. Oxford University Press **53**, 1999–2026.

Sparks, R. S. J. & Cashman, K. V (2017). Dynamic Magma Systems: Implications for Forecasting Volcanic Activity. *Elements* **13**, 35–40.

Sparks, R. S. J. & Marshall, L. A. (1986). Thermal and mechanical constraints on mixing between mafic and silicic magmas. *Journal of Volcanology and Geothermal Research*. Elsevier **29**, 99–124.

Sruoga, P., Etcheverría, M. P., Feineman, M., Rosas, M., Bukert, C. & Ibañes, O. (2012). Complejo

Caldera Diamante-volcán Maipo (34° 10'S, 69°50'O): Evolución volcanológica y geoquímica e implicancias en su peligrosidad. *Revista de la Asociación Geológica Argentina*. SciELO Argentina **69**, 508–530.

Sruoga, P., Llambías, E. J., Fauqué, L., Schonwandt, D. & Repol, D. G. (2005). Volcanological and geochemical evolution of the Diamante Caldera–Maipo volcano complex in the southern Andes of Argentina (34 10′ S). *Journal of South American Earth Sciences*. Elsevier **19**, 399–414.

Stern, C. R. (2004). Active Andean volcanism: its geologic and tectonic setting. *Revista geológica de Chile*. SciELO Chile **31**, 161–206.

Stern, C. R., Floody, R. & Espiñeíra, D. (2011a). Olivine-hornblende-lamprophyre dikes from Quebrada los Sapos, El Teniente, Central Chile (34° S): implications for the temporal geochemical evolution of the Andean subarc mantle. *Andean Geology*. Servicio Nacional de Geología y Minería **38**.

Stern, C. R. & Skewes, M. A. (1995). Miocene to present magmatic evolution at the northern end of the Andean Southern Volcanic Zone, Central Chile. *Andean Geology* **22**, 261–272.

Stern, C. R., Skewes, M. A. & Arévalo, A. (2011b). Magmatic Evolution of the Giant El Teniente Cu–Mo Deposit, Central Chile. *Journal of Petrology* **52**, 1591–1617.

Streck, M. J. & Dilles, J. H. (1998). Sulfur evolution of oxidized arc magmas as recorded in apatite from a porphyry copper batholith. *Geology*. Geological Society of America **26**, 523–526.

Streck, M. J., Leeman, W. P. & Chesley, J. (2007). High-magnesian andesite from Mount Shasta: A product of magma mixing and contamination, not a primitive mantle melt. *Geology*. Geological Society of America **35**, 351–354.

Sun, S.-S. & McDonough, W. (1989). Chemical and isotopic systematics of oceanic basalts: implications for mantle composition and processes. *Geological Society, London, Special Publications*. Geological Society of London **42**, 313–345.

Tapster, S., Condon, D. J., Naden, J., Noble, S. R., Petterson, M. G., Roberts, N. M. W., Saunders, A. D. & Smith, D. J. (2016). Rapid thermal rejuvenation of high-crystallinity magma linked to porphyry copper deposit formation; evidence from the Koloula Porphyry Prospect, Solomon Islands. *Earth and Planetary Science Letters*. Elsevier **442**, 206–217.

Tattitch, B. C. & Blundy, J. D. (2017). Cu-Mo partitioning between felsic melts and saline-aqueous fluids as a function of XNaCleq, fO2, and fS2. *American Mineralogist*. GeoScienceWorld **102**, 1987–2006.

Tattitch, B. C., Candela, P. A., Piccoli, P. M. & Bodnar, R. J. (2015). Copper partitioning between felsic melt and H 2 O–CO 2 bearing saline fluids. *Geochimica et Cosmochimica Acta*. Elsevier **148**, 81–99.

Tepley III, F. J., Davidson, J. P., Tilling, R. I. & Arth, J. G. (2000). Magma mixing, recharge and eruption histories recorded in plagioclase phenocrysts from El Chichon Volcano, Mexico. *Journal of Petrology*. Oxford University Press **41**, 1397–1411.

Ulrich, T., Günther, D. & Heinrich, C. A. (2002). The evolution of a porphyry Cu-Au deposit, based on LA-ICP-MS analysis of fluid inclusions: Bajo de la Alumbrera, Argentina. *Economic Geology*. SecG **97**, 1889–1920.

Van Hoose, A. E., Streck, M. J., Pallister, J. S. & Wälle, M. (2013). Sulfur evolution of the 1991 Pinatubo magmas based on apatite. *Journal of Volcanology and Geothermal Research*. Elsevier **257**, 72–89.

Vergara, M., Charrier, R., Munizaga, F., Rivano, S., Sepúlveda, P., Thiele, R. & Drake, R. (1988). Miocene volcanism in the central Chilean Andes (31 30′ S–34 35′ S). *Journal of South American Earth Sciences*. Elsevier **1**, 199–209.

Weis, P., Driesner, T. & Heinrich, C. A. (2012). Porphyry-copper ore shells form at stable pressure-temperature fronts within dynamic fluid plumes. *Science*. American Association for the Advancement of Science **338**, 1613–1616.

White, W. M. (1993). 238U/204Pb in MORB and open system evolution of the depleted mantle. *Earth and Planetary Science Letters*. Elsevier **115**, 211–226.

Williamson, B. J., Herrington, R. J. & Morris, A. (2016). Porphyry copper enrichment linked to excess aluminium in plagioclase. *Nature Geoscience*. Nature Research **9**, 237–241.

Wones, D. R. (1981). Mafic Silicates as Indicators of Intensive Variables in Granitic Magmas. *Mining Geology*.

Yáñez, G. A., Ranero, C. R., Huene, R. & Díaz, J. (2001). Magnetic anomaly interpretation across the southern central Andes (32–34 S): The role of the Juan Fernández Ridge in the late Tertiary evolution of the margin. *Journal of Geophysical Research: Solid Earth*. Wiley Online Library **106**, 6325–6345.

Yáñez, G., Cembrano, J., Pardo, M., Ranero, C. & Selles, D. (2002). The Challenger–Juan Fernández–Maipo major tectonic transition of the Nazca–Andean subduction system at 33–34 S: geodynamic evidence and implications. *Journal of South American Earth Sciences*. Elsevier **15**, 23–38.

Zajacz, Z., Hanley, J. J., Heinrich, C. A., Halter, W. E. & Guillong, M. (2009). Diffusive reequilibration of quartz-hosted silicate melt and fluid inclusions: Are all metal concentrations unmodified? *Geochimica et Cosmochimica Acta*. Elsevier **73**, 3013–3027.

Zhang, J., Davidson, J. P., Humphreys, M. C. S., Macpherson, C. G. & Neill, I. (2015). Magmatic Enclaves and Andesitic Lavas from Mt. Lamington, Papua New Guinea: Implications for Recycling of Earlier-fractionated Minerals through Magma Recharge. *Journal of Petrology*. Oxford University Press **56**, 2223–2256.

FIGURE CAPTIONS

Figure 1. (a) Geological map of central Chile showing the location of the DMIC study area, black box indicates the area of (b), major volcanoes, and Miocene-Pliocene PCDs. Map modified after Farías *et al.* (2010) and references therein. (b) Geological map of Don Manuel showing the Paredones and Don Manuel Principal areas. Map modified after (Candia *et al.*, 2009).

Figure 2. Total alkalis vs. silica (TAS) diagram after Le Maitre *et al.* (2002) of DMIC whole rock samples. DMIC samples range from basaltic andesite through to rhyolite (anhydrous normalized). For intermediate porphyry dike (IPD) samples characterized petrographically, the type of IPD has been

designated, the rest remain undivided. For regional context compositions of the El Teniente host rocks taken from Stern *et al.* (2011b) and compositions of Pleistocene and Holocene volcanic rocks from Maipo volcanic complex taken from (Futa & Stern, 1988; Harrington, 1989; Holm *et al.*, 2014; Sruoga *et al.*, 2005, 2012).

Figure 3. Selected major element vs. SiO_2 Harker diagrams for DMIC. Total Fe is plotted as FeO*. For intermediate porphyry dike (IPD) samples characterized petrographically, the type of IPD has been designated; the rest remain undivided. All symbols and the data sources for regional context compositions are the same as in Fig. 2.

Figure 4. Whole rock $^{143}Nd/^{144}Nd$ versus $^{87}Sr/^{86}Sr$ for the Coya Machali/Abanico and Farellones formations (Kay *et al.*, 2005; Kurtz *et al.*, 1997; Muñoz *et al.*, 2006; Nyström *et al.*, 2003), El Teniente volcanic and plutonic complex (Kay *et al.*, 2005; Kurtz *et al.*, 1997; Stern *et al.*, 2011b), Young plutonic complex, Jeria, Cruz de Piedra, Cerro Catedral (Kay *et al.*, 2005; Kurtz *et al.*, 1997), DMIC, NSVZ volcanics and field (Futa & Stern, 1988; Hildreth & Moorbath, 1988; Lopez-Escobar *et al.*, 1993), and Maipo volcanics (Holm *et al.*, 2014). Figure modified after (Holm *et al.*, 2014; Stern *et al.*, 2011b) with field of N-MORB from (Bach *et al.*, 1994; Douglass *et al.*, 1999; Haase, 2002; Jochum *et al.*, 1993; Macdougall & Lugmair, 1985; White, 1993). 2σ errors are smaller than symbol size.

Figure 5. Zircon initial εHf isotope ratios for the DMIC and other Miocene-Pliocene igneous rocks from central Chile. Data and locations (inset) for other Miocene-Pliocene intrusions from Deckart *et al.*, (2010) and Muñoz *et al.*, (2012).

Figure 6. Plagioclase phenocrysts of the DMIC. (a) Backscatter image of plagioclase from the rhyolite. (b) Backscatter image of plagioclase from an IPD1. (c) Backscatter image of plagioclase from an IPD 3. (d) Backscatter image of plagioclase from an IPD2. (e) Backscatter image of plagioclase from a mafic enclave. (f) Backscatter image of plagioclase from a basaltic andesite dike. (g) Anorthite content for plagioclase crystals in the various textural locations from the units of the DMIC. Yellow circles indicate

cores compositions; rim compositions are represented by blue circles, and matrix plagioclase by crosses. Overall the silica content of the units increases from the Paredones basaltic andesite to the Paredones rhyolite on the diagram. Mafic enclaves are hosted in the biotite tonalite and intermediate porphyry dike and the gabbroic xenolith is hosted in a basaltic andesite dike.

Figure 7. Trace element concentrations in DMIC plagioclase. (a) Sr content versus An content for plagioclase crystals in the quartz monzonite, rhyolite, biotite tonalite, mafic enclaves, gabbroic xenolith, DMP basaltic andesite, and Paredones basaltic andesite. (b) Sr content versus An content for plagioclase crystals in the three types of IPDs with the data from (a) shown in the background in gray.

Figure 8. (a) Photomicrograph of primary biotite phenocryst in one of the IPD1s (DM5AG13), cross-polarized light. (b) Secondary biotite clot in one of the IPD2s (DM1AG31), plane-polarized light. (c) Primary biotite compositions from the DMIC biotite tonalite and IPD, Mg-number versus TiO_2. (d) Mg-number versus TiO_2 for hydrothermal (secondary) biotite with primary biotite data from (c) show in gray in the background. (e) Mg-number versus Cl for primary biotite. (f) Mg-number = $(Mg/Mg+Fe_{tot})$ versus Cl for hydrothermal biotite with primary biotite data from (e) show in gray in the background.

Figure 9. (a) Clinopyroxene phenocryst in the Paredones basaltic andesite (DMN16), cross-polarized light. (b) Amphibole in the gabbro xenolith (DM7AG18), cross-polarized light. (c) Amphibole and plagioclase glomerocryst in an IPD3 (DM1AG23), plane polarized light. (d) Amphibole phenocryst in the biotite tonalite porphyry (DM4AG08), cross-polarized light.

Figure 10. (a) Al_{TOT} versus $(Na+K)_A$ graph for the amphibole-bearing DMIC units. (b) Al_{TOT} versus Mg-number graph of DMIC amphiboles showing two subgroups (1) high-Al_{TOT}, high Mg-number subgroup, and (2) a high Mg-number, low Al-total to low Mg-number = $(Mg/Mg+Fe^{2+})$, high Al_{TOT} trending subgroup.

Figure 11. Apatites of the DMIC. (a) Backscatter image of an apatite inclusion within a plagioclase phenocryst in an IPD2 (DM6AG11). (b) Backscatter image of an apatite microphenocryst in an IPD2

(DM6AG11). (c) Backscatter image of acicular needles of apatite within a basaltic andesite dike sample (DM5AG34). (d) Cl versus S content of DMIC apatites. Sulfur-poor apatites are plotted on the detection limit line (DL) with arrows to indicate concentrations may extend below the detection limit value of 90 ppm. DL for Cl = 80 ppm. Symbols as in Fig. 2.

Figure 12. DMIC zircon chondrite-normalized REE concentrations (Sun & McDonough, 1989) with representative zircon cathodoluminescence images of DMIC zircons. Locations of LA-ICPMS spots for trace element analyses are indicated by the white circles. Additional zircon cathodoluminescence images in Supplementary materials Fig. S1.

Figure 13. Zircon Yb/Gd versus Th/U concentration plot for the biotite tonalite, rhyolite, quartz monzonite, and intermediate porphyry dikes. Symbols as in Fig. 2.

Figure 14. (a) Calculated hornblende-plagioclase temperatures for the DMIC based on Holland & Blundy (1994). Granite solidus (680°-700°C) for H_2O-saturated haplogranite system from Johannes & Holtz (2012). Temperature range for magnetite-ilmenite pairs from samples DM3AG38 (IPD2), DM6AG21 (IPD3), and DM4AG27 (porphyritic biotite tonalite) based on the thermometer of Andersen & Lindsley (1985). (b) Calculated temperatures based on the Ti-in-zircon thermometer of Ferry & Watson, (2007) using values of $a\mathrm{TiO_2}$=0.7 and $a\mathrm{SiO_2}$=1.0. Circles indicate cores temperatures; rim temperatures are represented by crosses, and interior whole grain (for grains too small for separate core and rim measurements) temperatures are triangles. Symbols as in Fig. 2.

Figure 15. (a) Al_{TOT} versus $(Na+K)_A$ graph for the amphibole-bearing DMIC units. Gray fields show amphibole compositions for Pinatubo experimental amphiboles, with corresponding calculated pressures of crystallization (Prouteau & Scaillet, 2003; Scaillet & Evans, 1999) (b) Al_{TOT} versus Mg-number ($Mg/Mg+Fe_{tot}$) graph of DMIC amphiboles showing two subgroups (1) high-Al_{TOT}, high Mg-number subgroup, and (2) a high Mg-number, low Al-total to low Mg-number, high Al_{TOT} trending subgroup.

Figure 16. Volatile degassing trends. (a) Volatiles dissolved in quenched glasses from isothermal experiments by Lesne *et al.* (2011) based on Stromboli basalt starting composition and by Fiege *et al.*, (2014) on andesite starting composition as a function of pressure. For Lesne *et al.*, (2011) experiments were run at 1150ºC at NNO +1.6 to +2.4 with pressures ranging from 406 to 26 MPa; for Fiege *et al.*, (2014) experiments were run at 1030ºC at ~QFM+0.8 to ~QFM+4.2 and 500 to 70 MPa. Pressures for each experimental run are labeled in MPa. (b) Cl and S contents in apatites showing a fractionation pattern from Santiaguito and Pinatubo volcanoes and from the Santa Rita porphyry copper deposit and melt inclusions from Pinatubo (Audétat *et al.*, 2004; Scott *et al.*, 2015; Van Hoose *et al.*, 2013). The gray field represents the range of compositions from the Don Manuel apatites in this study.

Figure 17. (a) Cl content in amphibole versus hornblende-plagioclase temperatures for the amphibole-bearing units of the DMIC. (b) Cl_{melt} concentrations coexisting with amphibole using the Cl/OH exchange coefficient ($Kd_{Cl\text{-}OH}$) of Sato *et al.* (2005). Symbols as in Fig. 2.

Figure 18. (a) Plagioclase Sr as a function of anorthite trends observed in the DMIC. Trend 1 reflects early crystallization of plagioclase while Trend 2 suggests plagioclase is suppressed initially, likely due to high H_2O content. Slope of the dashed black line representing little to no plagioclase crystallizing would vary depending on the extent to which calcium-bearing phases (amphibole, clinopyroxene) crystallize prior to plagioclase saturation. (b) Results of rhyolite-MELTS-based modeling of Sr concentrations in plagioclase based on wt. % H_2O for different pressures using 500 ppm Sr as the initial magma content and partitioning coefficients from (Blundy & Wood, 1991). Unfilled circles indicate when sanidine is present for which Sr partitioning was not modeled. DMIC basaltic andesite (DM5AG34) was used as the magma composition. Gray fields represent the fields for the Sr content in the biotite tonalite and Paredones basaltic andesite. Note the stronger effect of crystallization pressure than initial H_2O content on the resulting Sr-An trends.

Figure 19. (a) One dimensional εHf plot of the DMIC showing hypothetical mixing proportions of depleted mantle and projected Cuyania terrane (assuming $^{176}Lu/^{177}Hf$ ratio of 0.015) with r = 0.037. R is calculated as the ratio between the ratio of the elemental concentration of Nd, Sr, and Hf between the end members (Deckart *et al.*, 2010; Kay *et al.*, 2005; Stern *et al.*, 2011b; Jones *et al.*, 2015; Muñoz *et al.*, 2013; Pepper *et al.*, 2016). The DMIC Hf data corresponds to ~3-4% mixing of Cuyania terrane. (b) εNd versus $^{87}Sr/^{86}Sr$ of the DMIC with a bivariate mixing line between depleted mantle and projected Cuyania terrane (r = 0.02). The DMIC Hf data corresponds to ~1-2% mixing of Chilenia terrane.

Figure 20. Petrogenetic model for the DMIC. (a) Emplacement of the quartz monzonite followed by rhyolite from an upper crustal magma reservoir. (b) Emplacement of the equigranular and porphyritic biotite tonalite from an upper crustal magma reservoir. Also during this time period pulses of mafic magma mingle with the biotite tonalite, and basaltic andesite dikes cut the biotite tonalite. (c) Injection of IPD magma batches sourced from various crustal magma reservoirs fed by residual melt from the deep crustal hot zone and hybridized by igneous mixing during ascent. Additional basaltic andesite dikes periodically ascend and cut the biotite tonalite and IPDs. Mineralization is most closely associated with the emplacement of the IPDs, although fluid exsolution and brine accumulation is likely protracted. Mafic magma associated with the magma mixing observed in the IPDs and with late basaltic andesite dikes may have sourced the sulfur required for mineralization. (d) Magma mingling end member of igneous mixing observed in the biotite tonalite. (e) Igneous mixing observed in the IPDs including mixing of magmas with various crystal cargo and entrainment of glomerocrysts and antecrysts.

1586

1587

1588

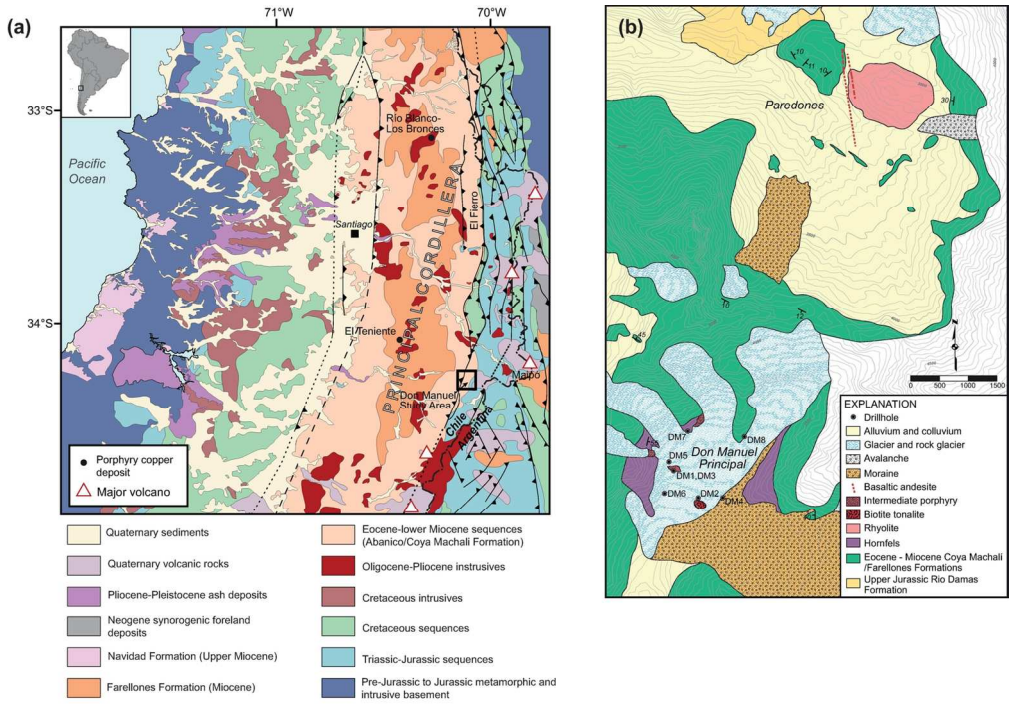

Figure 2. Total alkalis vs. silica (TAS) diagram after Le Maitre et al. (2002) of DMIC whole rock samples. DMIC samples range from basaltic andesite through to rhyolite (anhydrous normalized). For intermediate porphyry dike (IPD) samples characterized petrographically, the type of IPD has been designated, the rest remain undivided. For regional context compositions of the El Teniente host rocks taken from Stern et al. (2011b) and compositions of Pleistocene and Holocene volcanic rocks from Maipo volcanic complex taken from (Futa & Stern, 1988; Harrington, 1989; Holm et al., 2014; Sruoga et al., 2005, 2012).

142x100mm (300 x 300 DPI)

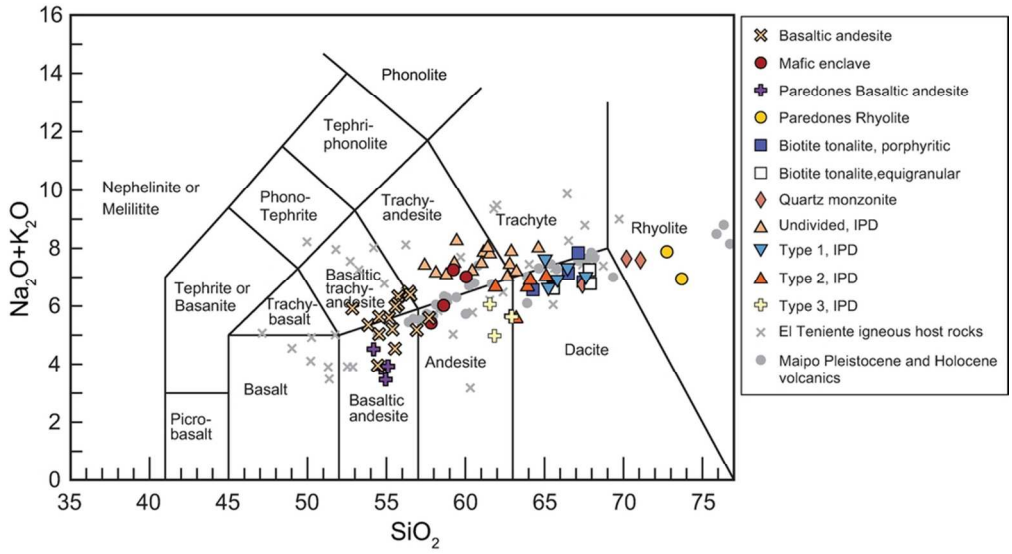

Figure 2. Total alkalis vs. silica (TAS) diagram after Le Maitre et al. (2002) of DMIC whole rock samples. DMIC samples range from basaltic andesite through to rhyolite (anhydrous normalized). For intermediate porphyry dike (IPD) samples characterized petrographically, the type of IPD has been designated, the rest remain undivided. For regional context compositions of the El Teniente host rocks taken from Stern et al. (2011b) and compositions of Pleistocene and Holocene volcanic rocks from Maipo volcanic complex taken from (Futa & Stern, 1988; Harrington, 1989; Holm et al., 2014; Sruoga et al., 2005, 2012).

87x48mm (300 x 300 DPI)

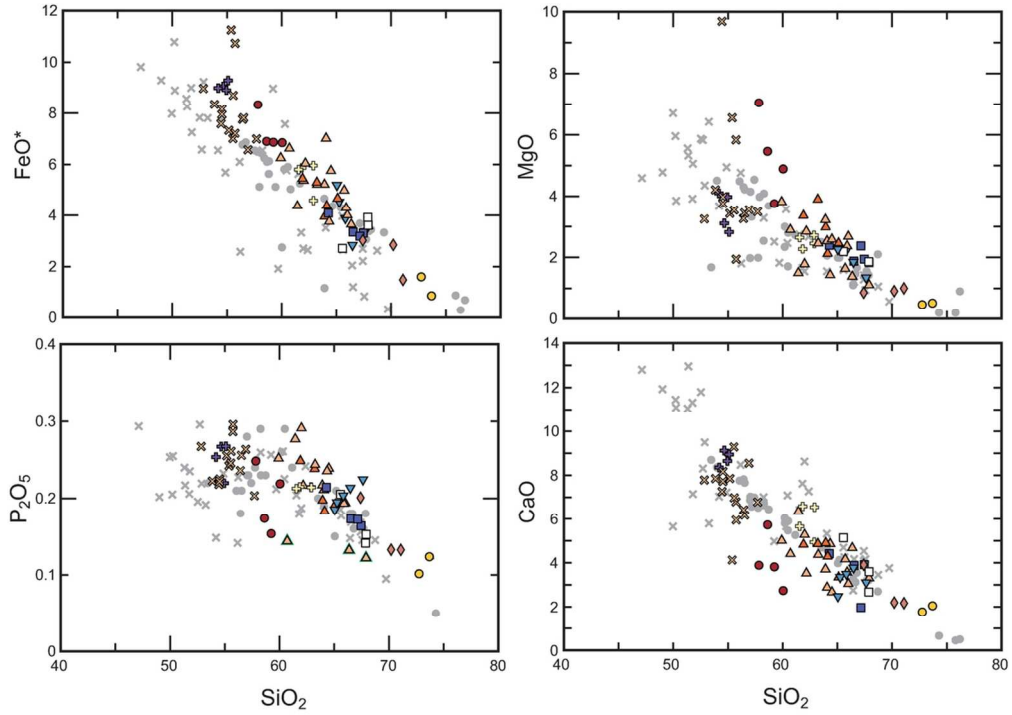

Figure 3. Selected major element vs. SiO2 Harker diagrams for DMIC. Total Fe is plotted as FeO*. For intermediate porphyry dike (IPD) samples characterized petrographically, the type of IPD has been designated; the rest remain undivided. All symbols and the data sources for regional context compositions are the same as in Fig. 2.

107x76mm (300 x 300 DPI)

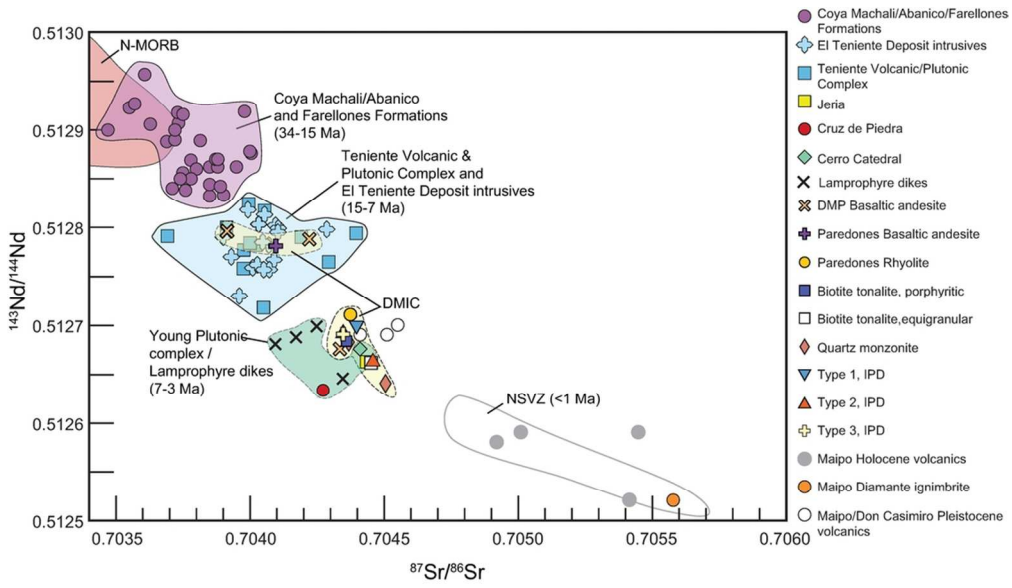

Figure 4. Whole rock 143Nd/144Nd versus 87Sr/86Sr for the Coya Machali/Abanico and Farellones formations (Kay et al., 2005; Kurtz et al., 1997; Muñoz et al., 2006; Nyström et al., 2003), El Teniente volcanic and plutonic complex (Kay et al., 2005; Kurtz et al., 1997; Stern et al., 2011b), Young plutonic complex, Jeria, Cruz de Piedra, Cerro Catedral (Kay et al., 2005; Kurtz et al., 1997), DMIC, NSVZ volcanics and field (Futa & Stern, 1988; Hildreth & Moorbath, 1988; Lopez-Escobar et al., 1993), and Maipo volcanics (Holm et al., 2014). Figure modified after (Holm et al., 2014; Stern et al., 2011b) with field of N-MORB from (Bach et al., 1994; Douglass et al., 1999; Haase, 2002; Jochum et al., 1993; Macdougall & Lugmair, 1985; White, 1993). 2σ errors are smaller than symbol size.

95x55mm (300 x 300 DPI)

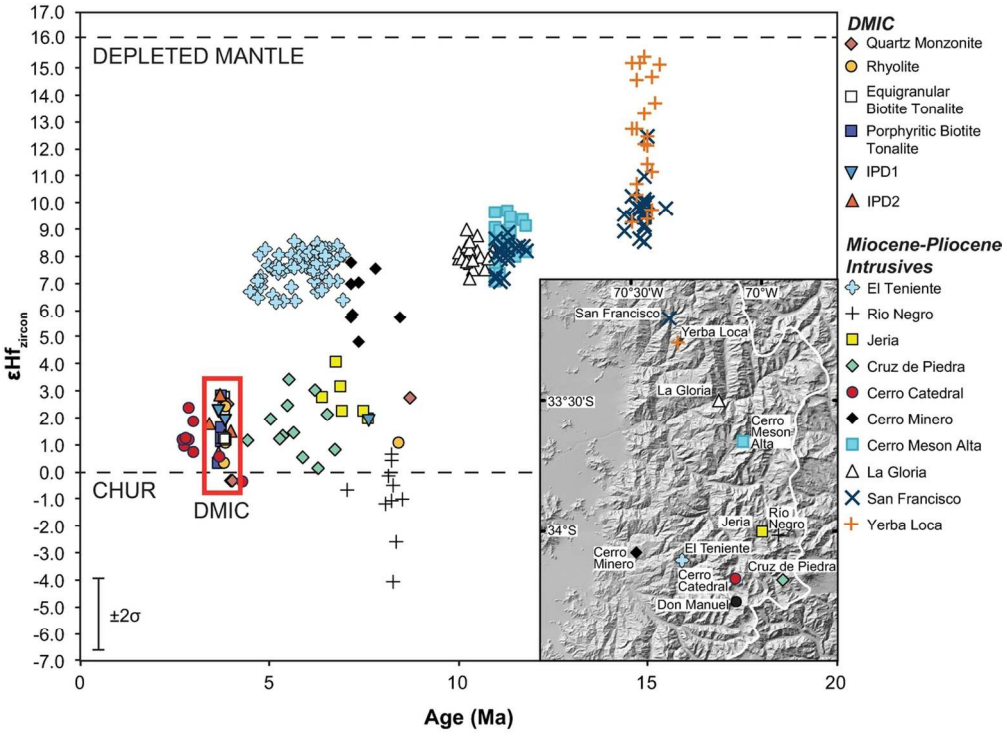

Figure 5. Zircon initial εHf isotope ratios for the DMIC and other Miocene-Pliocene igneous rocks from central Chile. Data and locations (inset) for other Miocene-Pliocene intrusions from Deckart et al., (2010) and Muñoz et al., (2012).

119x86mm (300 x 300 DPI)

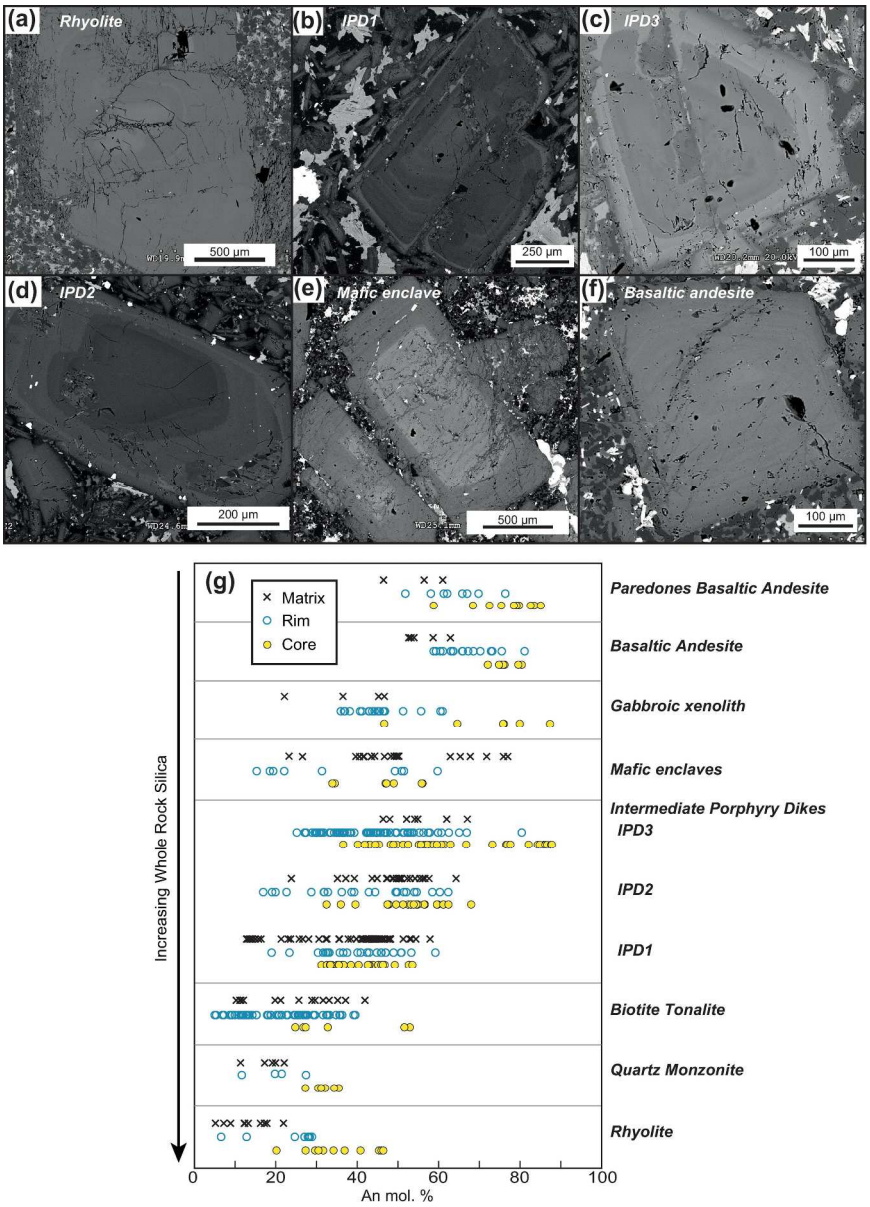

Figure 6. Plagioclase phenocrysts of the DMIC. (a) Backscatter image of plagioclase from the rhyolite. (b) Backscatter image of plagioclase from an IPD1. (c) Backscatter image of plagioclase from an IPD 3. (d) Backscatter image of plagioclase from an IPD2. (e) Backscatter image of plagioclase from a mafic enclave. (f) Backscatter image of plagioclase from a basaltic andesite dike. (g) Anorthite content for plagioclase crystals in the various textural locations from the units of the DMIC. Yellow circles indicate cores compositions; rim compositions are represented by blue circles, and matrix plagioclase by crosses. Overall the silica content of the units increases from the Paredones basaltic andesite to the Paredones rhyolite on the diagram. Mafic enclaves are hosted in the biotite tonalite and intermediate porphyry dike and the gabbroic xenolith is hosted in a basaltic andesite dike.

213x296mm (300 x 300 DPI)

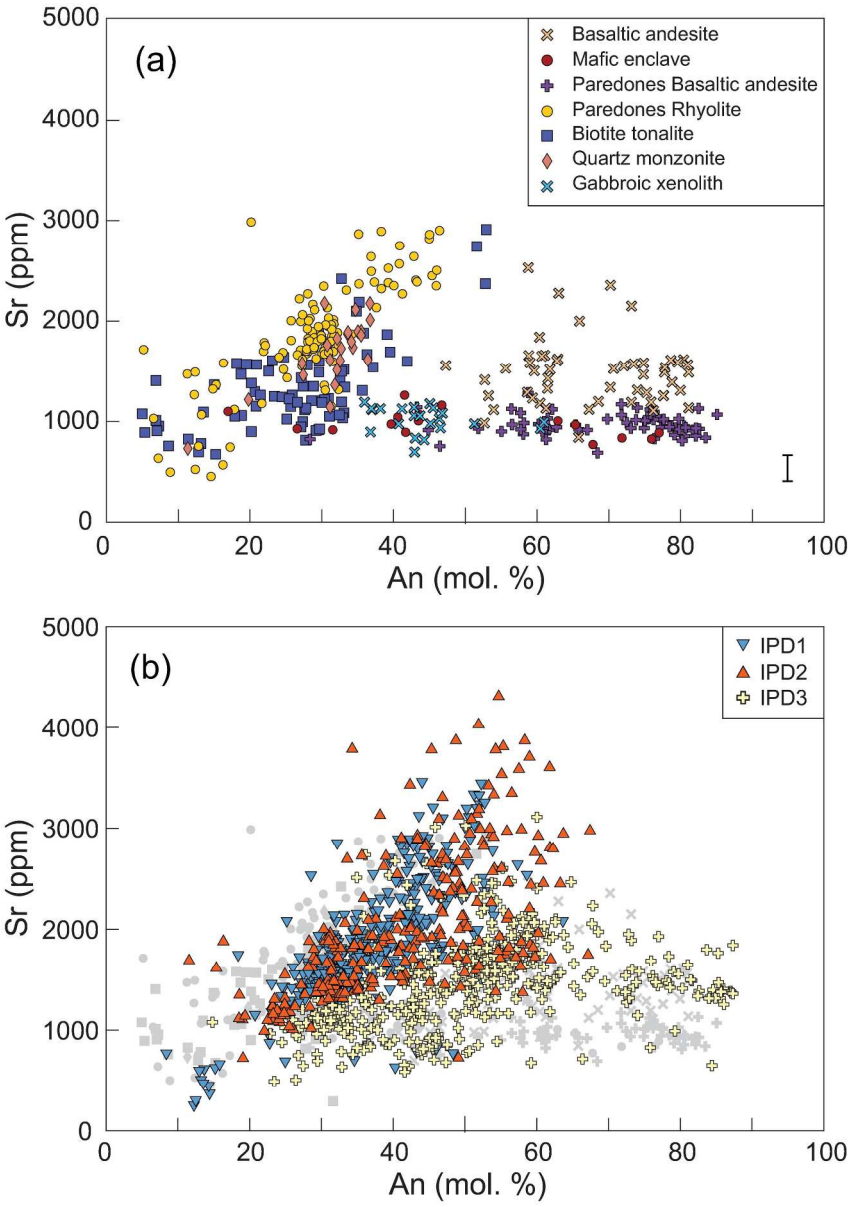

Figure 7. Trace element concentrations in DMIC plagioclase. (a) Sr content versus An content for plagioclase crystals in the quartz monzonite, rhyolite, biotite tonalite, mafic enclaves, gabbroic xenolith, DMP basaltic andesite, and Paredones basaltic andesite. (b) Sr content versus An content for plagioclase crystals in the three types of IPDs with the data from (a) shown in the background in gray.

196x278mm (300 x 300 DPI)

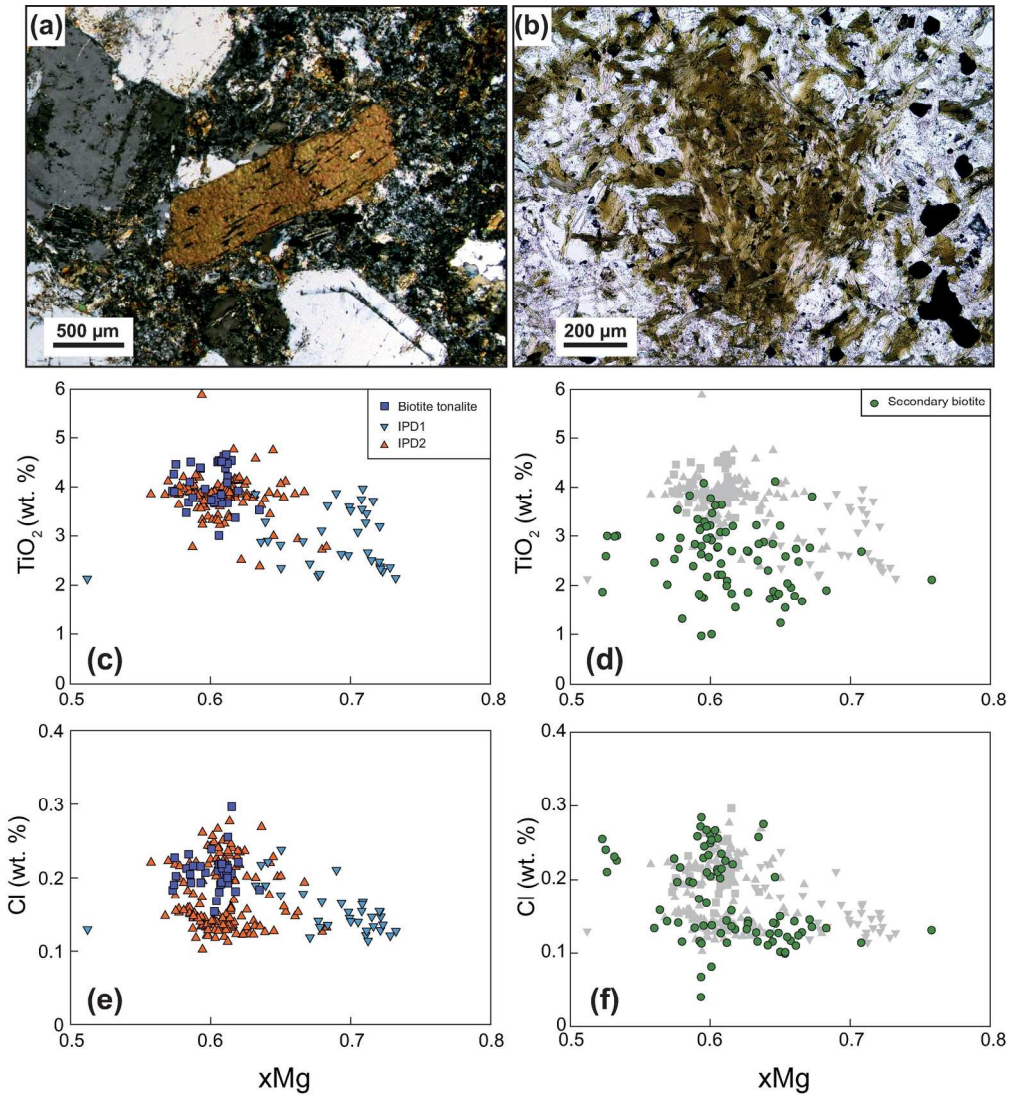

Figure 8. (a) Photomicrograph of primary biotite phenocryst in one of the IPD1s (DM5AG13), cross-polarized light. (b) Secondary biotite clot in one of the IPD2s (DM1AG31), plane-polarized light. (c) Primary biotite compositions from the DMIC biotite tonalite and IPD, Mg-number versus TiO2. (d) Mg-number versus TiO2 for hydrothermal (secondary) biotite with primary biotite data from (c) show in gray in the background. (e) Mg-number versus Cl for primary biotite. (f) Mg-number = (Mg/Mg+Fetot) versus Cl for hydrothermal biotite with primary biotite data from (e) show in gray in the background.

166x181mm (300 x 300 DPI)

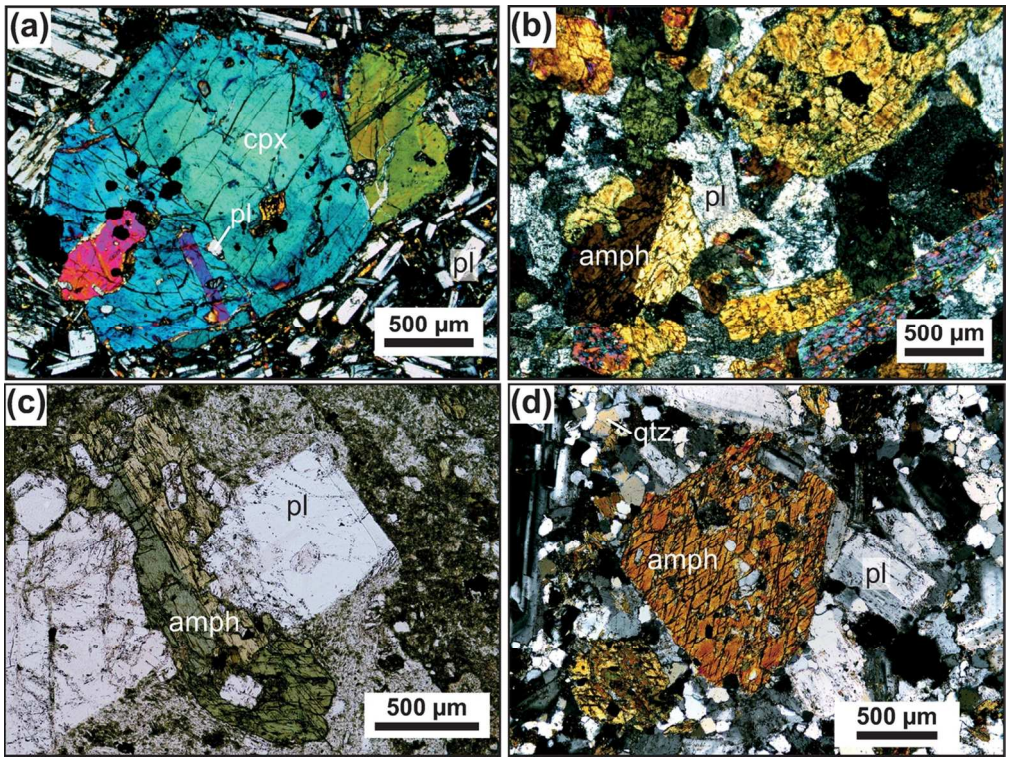

Figure 9. (a) Clinopyroxene phenocryst in the Paredones basaltic andesite (DMN16), cross-polarized light. (b) Amphibole in the gabbro xenolith (DM7AG18), cross-polarized light. (c) Amphibole and plagioclase glomerocryst in an IPD3 (DM1AG23), plane polarized light. (d) Amphibole phenocryst in the biotite tonalite porphyry (DM4AG08), cross-polarized light.

111x83mm (300 x 300 DPI)

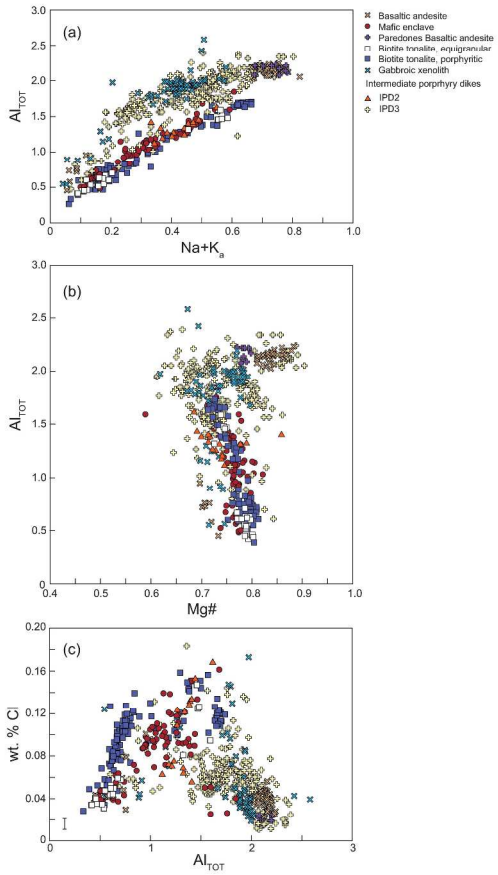

Figure 10. (a) AlTOT versus (Na+K)A graph for the amphibole-bearing DMIC units. (b) AlTOT versus Mg-number graph of DMIC amphiboles showing two subgroups (1) high-AlTOT, high Mg-number subgroup, and (2) a high Mg-number, low Al-total to low Mg-number = (Mg/Mg+Fe2+), high AlTOT trending subgroup.

279x361mm (300 x 300 DPI)

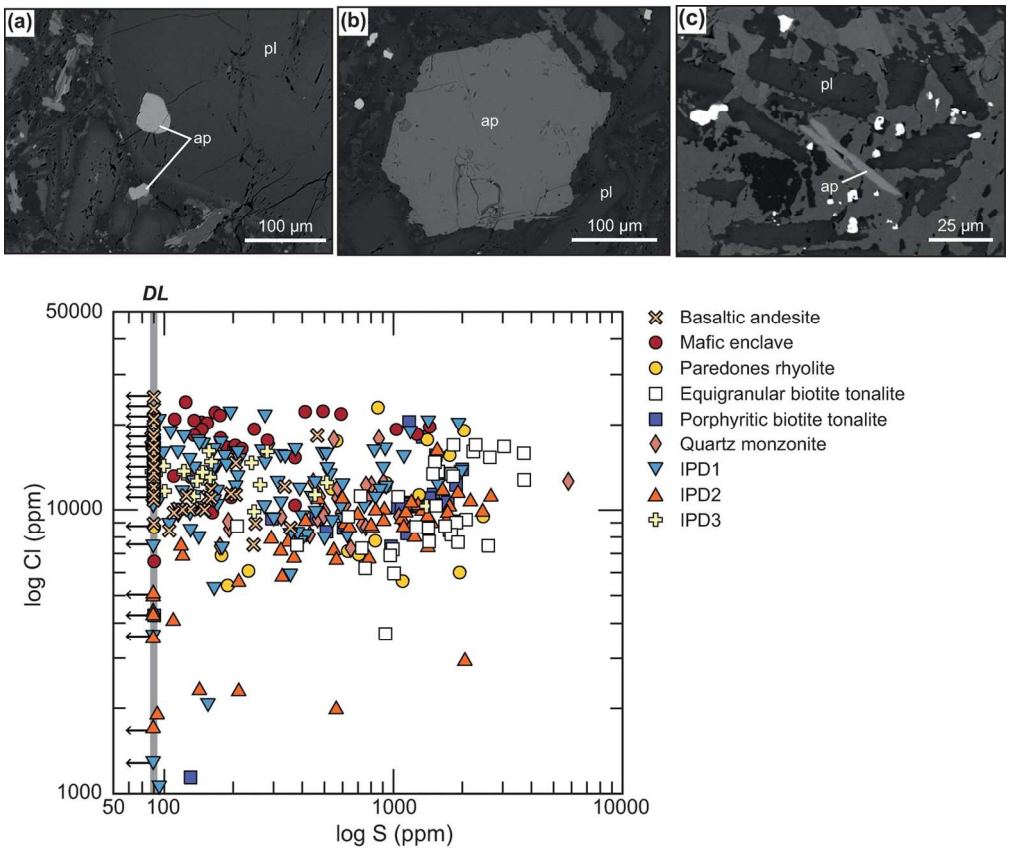

Figure 11. Apatites of the DMIC. (a) Backscatter image of an apatite inclusion within a plagioclase phenocryst in an IPD2 (DM6AG11). (b) Backscatter image of an apatite microphenocryst in an IPD2 (DM6AG11). (c) Backscatter image of acicular needles of apatite within a basaltic andesite dike sample (DM5AG34). (d) Cl versus S content of DMIC apatites. Sulfur-poor apatites are plotted on the detection limit line (DL) with arrows to indicate concentrations may extend below the detection limit value of 90 ppm. DL for Cl = 80 ppm. Symbols as in Fig. 2.

136x115mm (300 x 300 DPI)

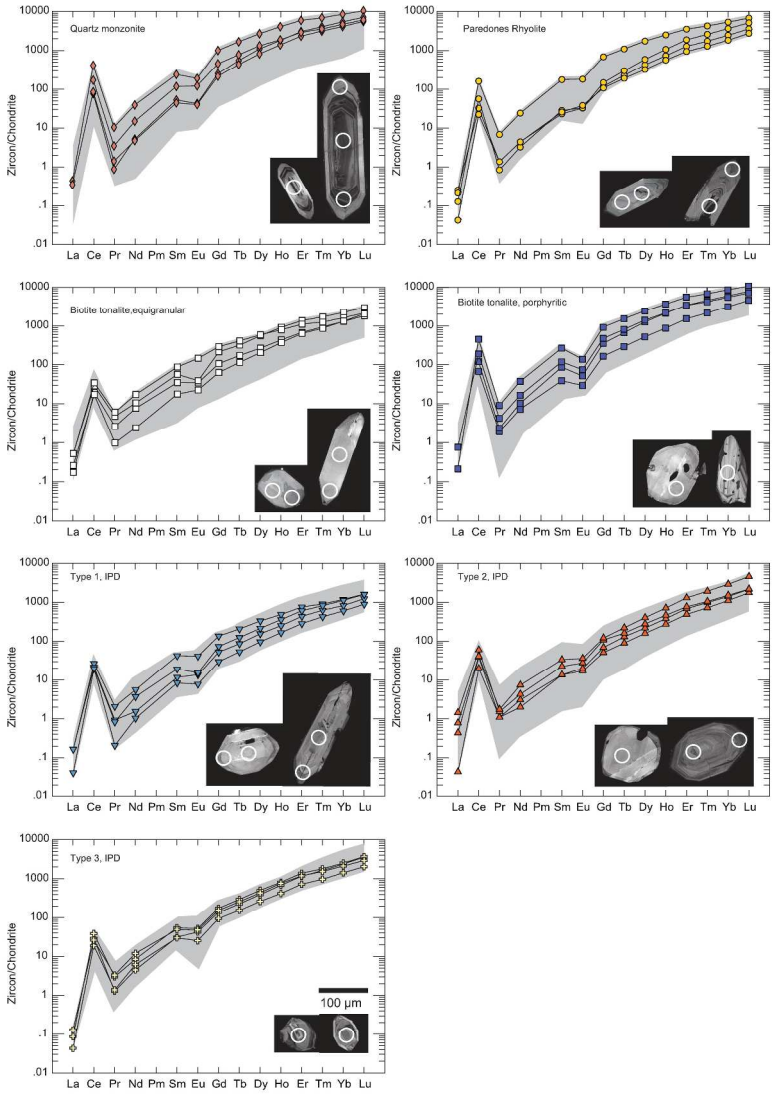

Figure 12. DMIC zircon chondrite-normalized REE concentrations (Sun & McDonough, 1989) with representative zircon cathodoluminescence images of DMIC zircons. Locations of LA-ICPMS spots for trace element analyses are indicated by the white circles. Additional zircon cathodoluminescence images in Supplementary materials Fig. S1.

297x420mm (300 x 300 DPI)

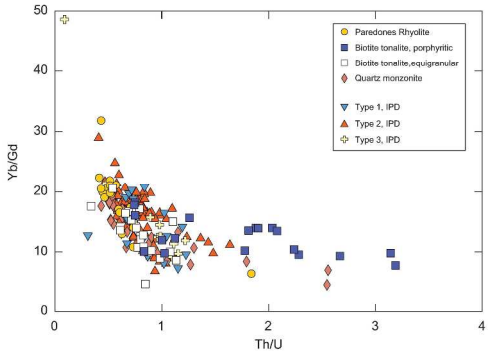

Figure 13. Zircon Yb/Gd versus Th/U concentration plot for the biotite tonalite, rhyolite, quartz monzonite, and intermediate porphyry dikes. Symbols as in Fig. 2.

297x420mm (300 x 300 DPI)

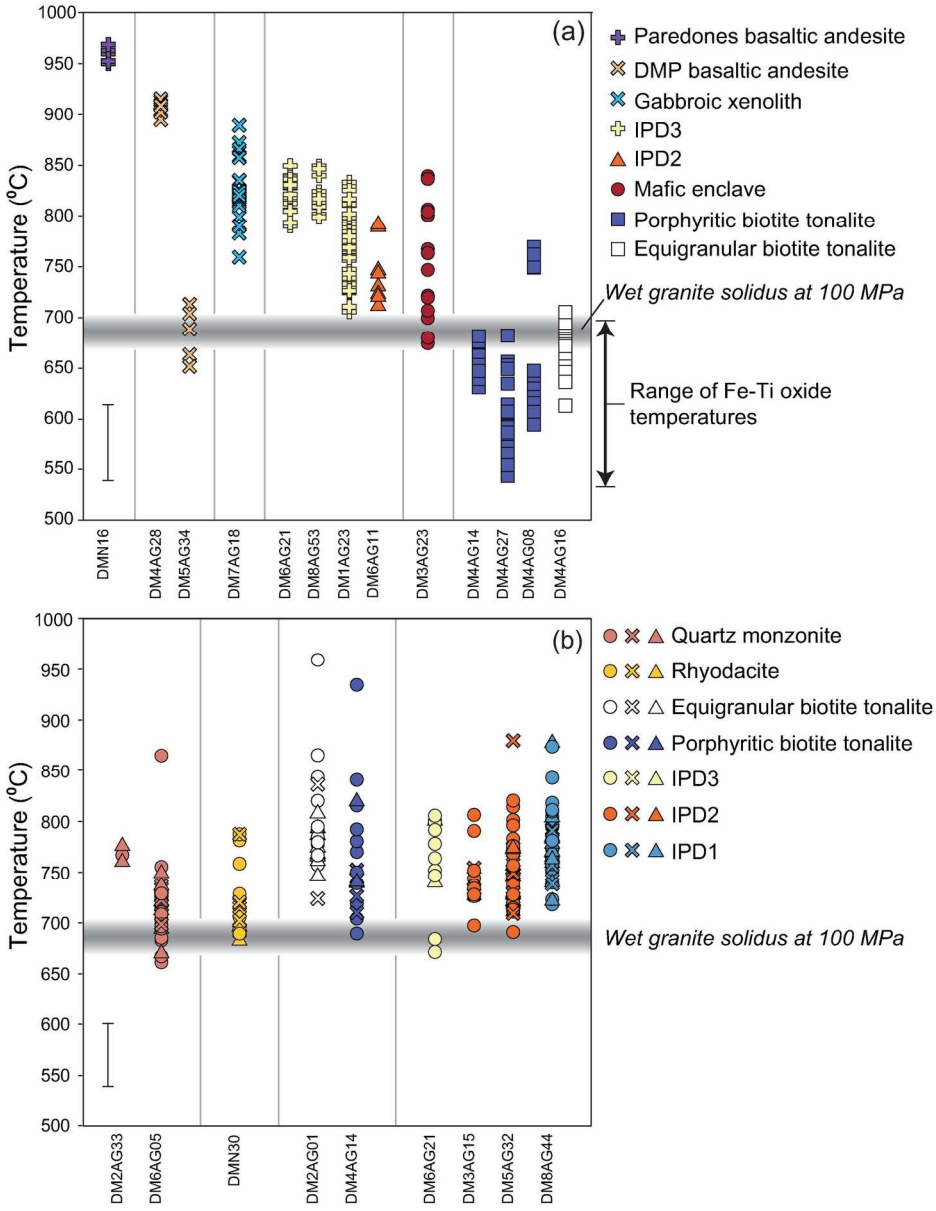

Figure 14. (a) Calculated hornblende-plagioclase temperatures for the DMIC based on Holland & Blundy (1994). Granite solidus (680°-700°C) for H2O-saturated haplogranite system from Johannes & Holtz (2012). Temperature range for magnetite-ilmenite pairs from samples DM3AG38 (IPD2), DM6AG21 (IPD3), and DM4AG27 (porphyritic biotite tonalite) based on the thermometer of Andersen & Lindsley (1985). (b) Calculated temperatures based on the Ti-in-zircon thermometer of Ferry & Watson, (2007) using values of aTiO2=0.7 and aSiO2=1.0. Circles indicate cores temperatures; rim temperatures are represented by crosses, and interior whole grain (for grains too small for separate core and rim measurements) temperatures are triangles. Symbols as in Fig. 2.

156x203mm (300 x 300 DPI)

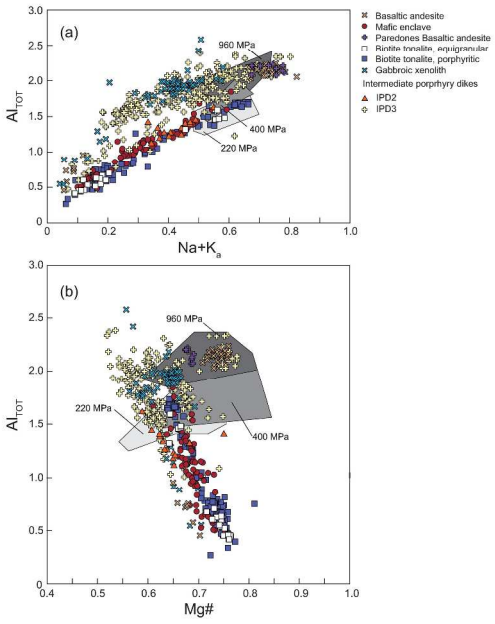

Figure 15. (a) AlTOT versus (Na+K)A graph for the amphibole-bearing DMIC units. Gray fields show amphibole compositions for Pinatubo experimental amphiboles, with corresponding calculated pressures of crystallization (Prouteau & Scaillet, 2003; Scaillet & Evans, 1999) (b) AlTOT versus Mg-number (Mg/Mg+Fetot) graph of DMIC amphiboles showing two subgroups (1) high-AlTOT, high Mg-number subgroup, and (2) a high Mg-number, low Al-total to low Mg-number, high AlTOT trending subgroup.

279x361mm (300 x 300 DPI)

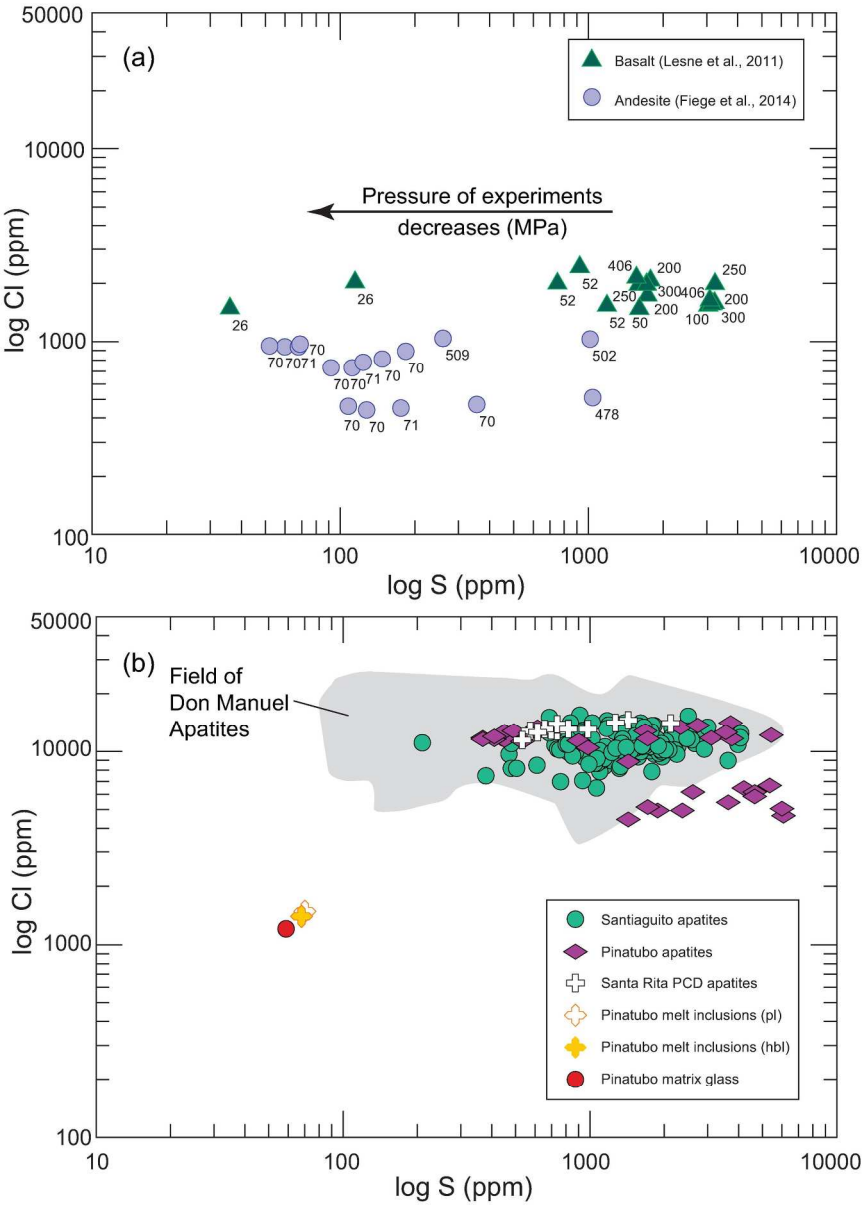

Figure 16. Volatile degassing trends. (a) Volatiles dissolved in quenched glasses from isothermal experiments by Lesne et al. (2011) based on Stromboli basalt starting composition and by Fiege et al., (2014) on andesite starting composition as a function of pressure. For Lesne et al., (2011) experiments were run at 1150ºC at NNO +1.6 to +2.4 with pressures ranging from 406 to 26 MPa; for Fiege et al., (2014) experiments were run at 1030ºC at ~QFM+0.8 to ~QFM+4.2 and 500 to 70 MPa. Pressures for each experimental run are labeled in MPa. (b) Cl and S contents in apatites showing a fractionation pattern from Santiaguito and Pinatubo volcanoes and from the Santa Rita porphyry copper deposit and melt inclusions from Pinatubo (Audétat et al., 2004; Scott et al., 2015; Van Hoose et al., 2013). The gray field represents the range of compositions from the Don Manuel apatites in this study.

190x265mm (300 x 300 DPI)

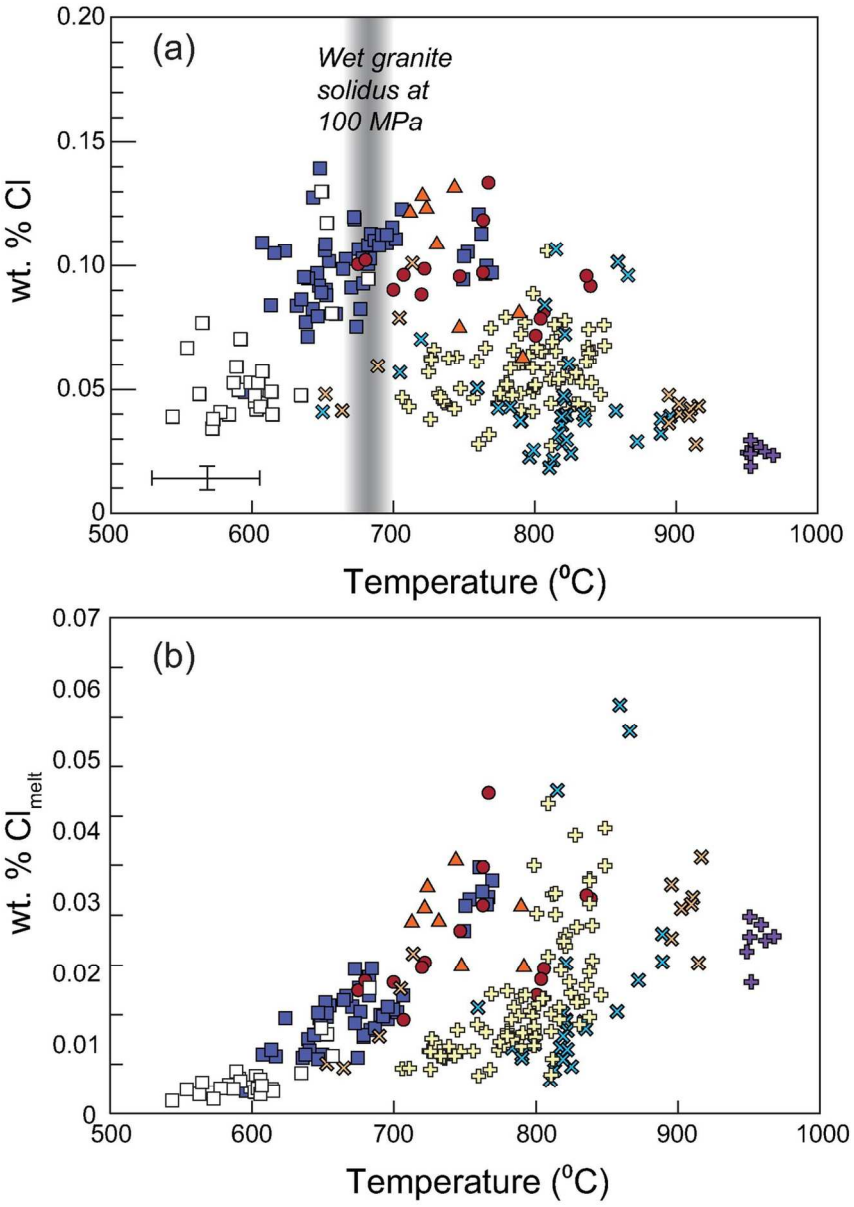

Figure 17. (a) Cl content in amphibole versus hornblende-plagioclase temperatures for the amphibole-bearing units of the DMIC. (b) Clmelt concentrations coexisting with amphibole using the Cl/OH exchange coefficient (KdCl-OH) of Sato et al. (2005). Symbols as in Fig. 2.

111x158mm (300 x 300 DPI)

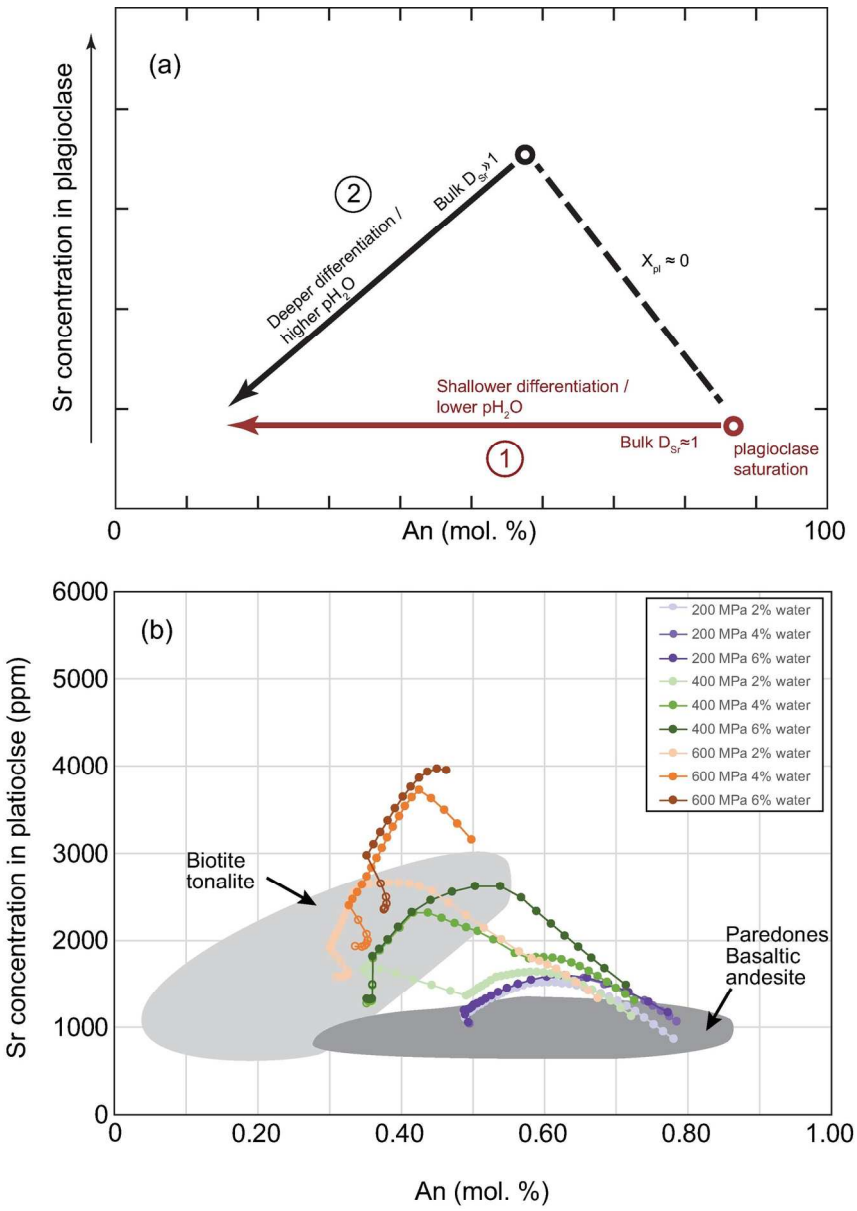

Figure 18. (a) Plagioclase Sr as a function of anorthite trends observed in the DMIC. Trend 1 reflects early crystallization of plagioclase while Trend 2 suggests plagioclase is suppressed initially, likely due to high H2O content. Slope of the dashed black line representing little to no plagioclase crystallizing would vary depending on the extent to which calcium-bearing phases (amphibole, clinopyroxene) crystallize prior to plagioclase saturation. (b) Results of rhyolite-MELTS-based modeling of Sr concentrations in plagioclase based on wt. % H2O for different pressures using 500 ppm Sr as the initial magma content and partitioning coefficients from (Blundy & Wood, 1991). Unfilled circles indicate when sanidine is present for which Sr partitioning was not modeled. DMIC basaltic andesite (DM5AG34) was used as the magma composition. Gray fields represent the fields for the Sr content in the biotite tonalite and Paredones basaltic andesite. Note the stronger effect of crystallization pressure than initial H2O content on the resulting Sr-An trends.

158x196mm (300 x 300 DPI)

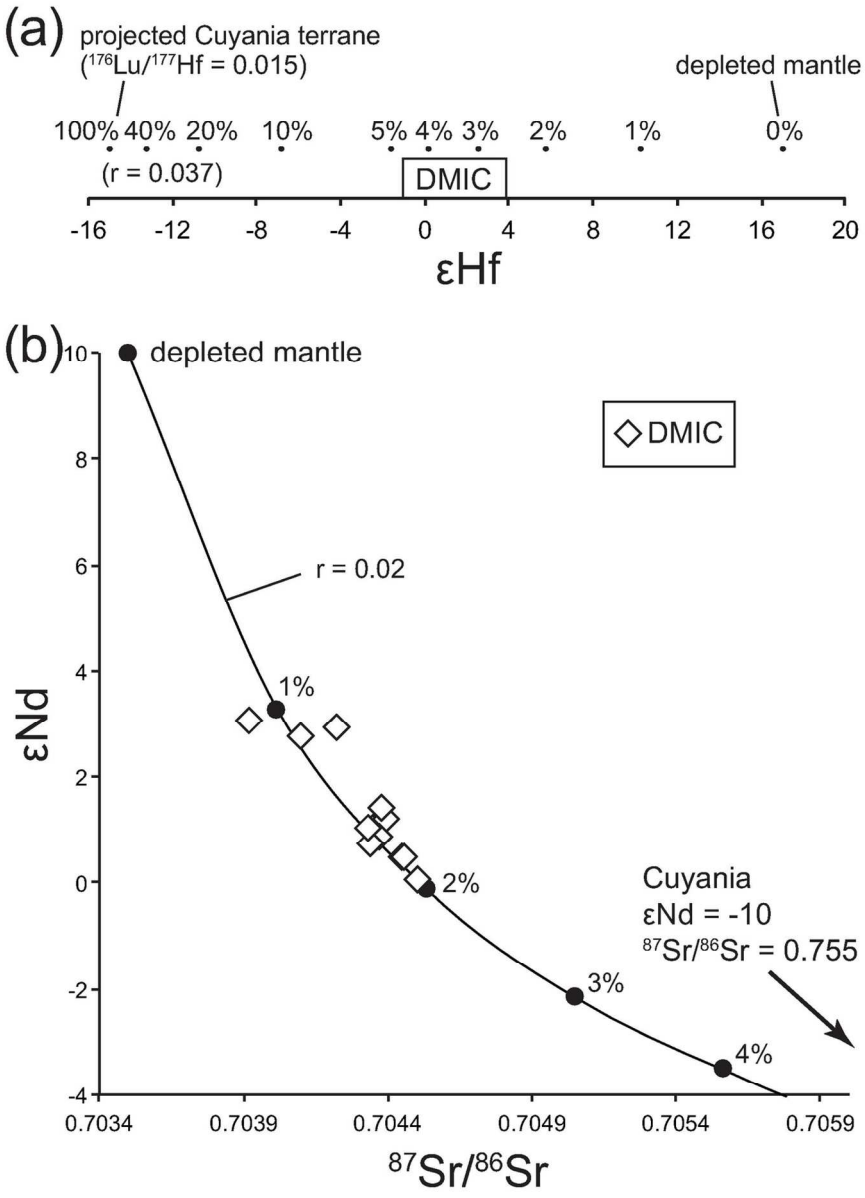

Figure 19. (a) One dimensional εHf plot of the DMIC showing hypothetical mixing proportions of depleted mantle and projected Cuyania terrane (assuming 176Lu/177Hf ratio of 0.015) with r = 0.037. R is calculated as the ratio between the ratio of the elemental concentration of Nd, Sr, and Hf between the end members (Deckart et al., 2010; Kay et al., 2005; Stern et al., 2011b; Jones et al., 2015; Muñoz et al., 2013; Pepper et al., 2016). The DMIC Hf data corresponds to ~3-4% mixing of Cuyania terrane. (b) εNd versus 87Sr/86Sr of the DMIC with a bivariate mixing line between depleted mantle and projected Cuyania terrane (r = 0.02). The DMIC Hf data corresponds to ~1-2% mixing of Cuyania terrane.

113x157mm (300 x 300 DPI)

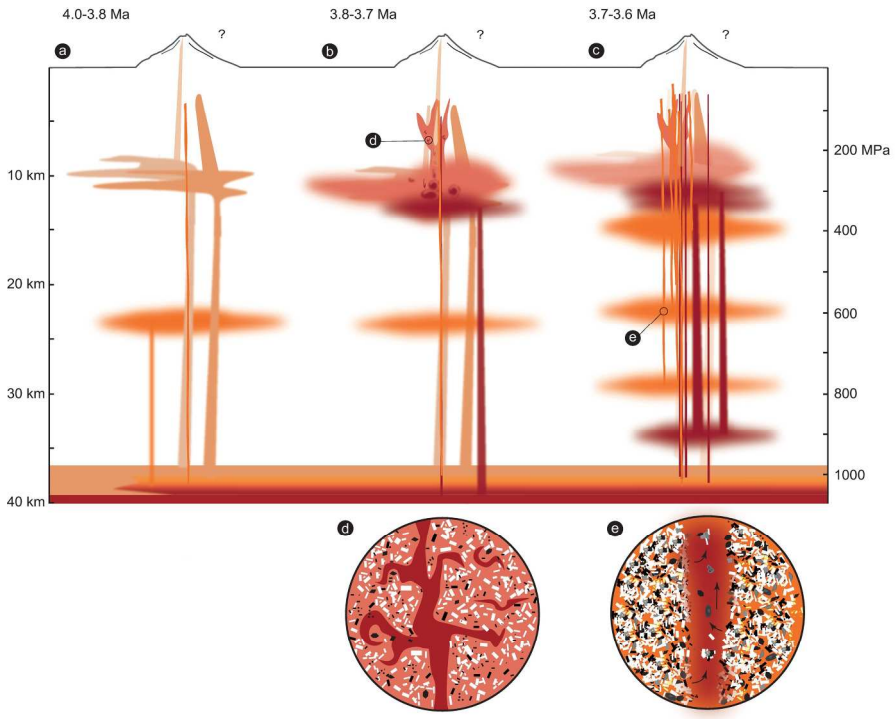

Figure 20. Petrogenetic model for the DMIC. (a) Emplacement of the quartz monzonite followed by rhyolite from an upper crustal magma reservoir. (b) Emplacement of the equigranular and porphyritic biotite tonalite from an upper crustal magma reservoir. Also during this time period pulses of mafic magma mingle with the biotite tonalite, and basaltic andesite dikes cut the biotite tonalite. (c) Injection of IPD magma batches sourced from various crustal magma reservoirs fed by residual melt from the deep crustal hot zone and hybridized by igneous mixing during ascent. Additional basaltic andesite dikes periodically ascend and cut the biotite tonalite and IPDs. Mineralization is most closely associated with the emplacement of the IPDs, although fluid exsolution and brine accumulation is likely protracted. Mafic magma associated with the magma mixing observed in the IPDs and with late basaltic andesite dikes may have sourced the sulfur required for mineralization. (d) Magma mingling end member of igneous mixing observed in the biotite tonalite. (e) Igneous mixing observed in the IPDs including mixing of magmas with various crystal cargo and entrainment of glomerocrysts and antecrysts.

218x161mm (300 x 300 DPI)

Table 1: Summary of the petrography and geochronology of the Don Manuel Igneous Complex, Chile

Rock Type	Location	Texture	Mineralogy	Alteration	Age
Quartz monzonite	Don Manuel Principal drill core; dikes	Equigranular to Porphyritic	50-60% Pl; 20-30% Af; 20-25% Qtz; 5% Bt; >2% Hb; *Accessory:* Ap, Anh, Mag, Rt, Zrn;	Moderate silicification locally;	4.058 ± 0.015 Ma[1,3] 3.975 ± 0.058 Ma[1,3]
Rhyolite	Paredones; stock; outcrop	Porphyritic	50-60% Microcrystalline Gm; *Phenocrysts:* 30-40% Pl; 10% Qtz; 5% Bt; *Matrix/Accessory:* Pl, Qtz, Af, Bt, Ap, Ttn, Zrn;	Moderate silicification locally; Py	3.879 ± 0.018 Ma[1,3]
Biotite tonalite	Don Manuel Principal drill core; stock	Equigranular	50-60% Pl; 25-30% Qtz; 5% Af; 7-10% Bt; 0-5% Hb; *Accessory:* Ap, Anh, Mag, Ilm, Ttn, Zrn;	HT Bt disseminated and pseudomorphs after Hb	3.829 ± 0.010 Ma[1,3]
Biotite tonalite (porphyritic phase)	Don Manuel Principal drill core; dikes	Porphyritic	55% GM; *Phenocrysts:* 50% Pl; 10% Hb; 7% Bt; 30% Qtz; 3% Af; *Matrix/Accessory:* Pl, Qtz, Af, Bt, Ap, Anh, Mag, Ilm, Ttn, Zrn;	HT Bt disseminated and pseudomorphs after Hb; Act after Hb	3.733 ± 0.010 Ma[1,3]
Intermediate porphyry dike suite (IPD)	Don Manuel Principal drill core; dikes				
Type 1		Porphyritic	40-65% Microcrystalline Gm; *Phenocrysts:* 25-40% Pl; 8-15% Bt; 1-15% Qtz; *Matrix/Accessory:* Qtz, Ap, Anh, Mag; Ilm; Ttn, Zrn;	HT Bt disseminated and pseudomorphs after Hb; locally Ttn and/or mag replace mafics; Act±Chl after Hb	3.733 ± 0.048 Ma[1,3]
Type 2		Porphyritic	60-70% Microcrystalline Gm; *Phenocrysts:* 20-25% Pl; 5-8% Hb; 2% Bt; *Matrix/Accessory:* Qtz, Ap, Anh, Mag, Ilm, Ttn, Zrn	HT Bt disseminated and pseudomorphs after Hb; locally Ttn and/or mag replace mafics; Act±Chl after Hb	3.657 ± 0.031 Ma[1,3] 3.656 ± 0.029 Ma[1,3]
Type 3		Porphyritic	55-65% Microcrystalline Gm; *Phenocrysts:* 20-30% Pl 8-15% Hb; 2% Mag/Ilm; *Matrix/Accessory:* Qtz, Ap, Anh, Mag, Ilm, Ttn, Zrn	HT Bt disseminated and pseudomorphs after Hb; locally Ttn and/or mag replace mafics; Act±Chl after Hb	3.912 ± 0.057 Ma[1,3]
Mafic enclaves	Don Manuel Principal drill core; hosted by rhyodacite, biotite tonalite, and IPD;	Equigranular	65-89% Gm; *Phenocrysts:* 52-55%Pl; 8-12% Bt; 2-23% Hb; *Matrix/Accessory:* Qtz; Ap, Mag, Ilm;	HT Bt after Hb	
Cpx basaltic andesite dikes	Paredones; dikes; outcrop	Porphyritic	40% Gm; *Phenocrysts:* 85% Pl; 10% Cpx; 3% Mag; 2% Hb; *Matrix/Accessory:* Pl, Cpx, Mag, Ilm;	Chl, Act, Epi, Cal	
Basaltic andesite dikes	Don Manuel Principal drill core; occurs as dikes	Equigranular to Porphyritic	55-70% Microcrystalline Gm; *Phenocrysts:* 65-77% Pl; 16-20%Hb; *Matrix/Accessory:* Pl, Mag; Ilm; Ap;	HT Bt after Hb ; Chl, Act, Epi, Cal	3.85 ± 0.19 Ma[2,3] 3.36 ± 0.09 Ma[2,3] 3.24 ± 0.06 Ma[2,3] 2.96 ± 0.11 Ma[2,3] 2.88 ± 0.06 Ma[2,3]
Gabbroic Cumulate xenolith	Don Manuel Principal drill core; hosted by basaltic andesite	Equigranular	55% Pl, 45% Hb; *Accessory:* Ap, Mag, Ilm;	Act after Hb	

Notes: Afs=alkali-feldspar; Act=actinolite; Anh=anhydrite; Ap=apatite; Bt=biotite; Cal=calcite; Chl=chlorite; Cpx=clinopyroxene; Epi=epidote; Gm=groundmass; Hb=hornblende; HT=Hydrothermal; Ilm=ilmenite; Mag=magnetite; Pl=plagioclase; Py=pyrite; Qtz=quartz; Rt = rutile; Ttn=titanite; Zrn=zircon;

*where present

[1] CA-ID-TIMS U-Pb Zircon

[2] ^{40}Ar-^{39}Ar Whole rock

[3] Gilmer et al. (2017)

Table 2. Isotopic compositions of the Don Manuel Igneous Complex, Chile

Sample	Lithology	$^{87}Sr/^{86}Sr$	2σ	$^{143}Nd/^{144}Nd$	2σ	εNd	$^{206}Pb/^{204}Pb$	2σ	$^{207}Pb/^{204}Pb$	2σ	$^{208}Pb/^{204}Pb$	2σ
DM6AG21	IPD3	0.704347	5	0.512691	6	1.04	18.6631	0.0008	15.6228	0.0007	38.5932	0.0020
DM2AG01	Equigranular Biotite Tonalite	0.704361	4	0.512684	4	0.90	18.6501	0.0011	15.6168	0.0010	38.5682	0.0024
DM8AG44	IPD1	0.704397	5	0.512700	3	1.21	18.6576	0.0012	15.6236	0.0010	38.5696	0.0025
DM2AG33	Quartz monzonite	0.704505	5	0.512641	2	0.06	18.6503	0.0008	15.6176	0.0008	38.5634	0.0021
DM6AG05	Quartz monzonite	0.704368	5	0.512683	4	0.88	18.6504	0.0010	15.6197	0.0009	38.5719	0.0025
DM4AG14	Porphyritic Biotite Tonalite	0.704451	4	0.512662	4	0.48	18.6506	0.0006	15.6237	0.0006	38.5875	0.0015
DM7AG26	DMP Basaltic andesite	0.704335	5	0.512676	3	0.75	18.6263	0.0011	15.6176	0.0010	38.5532	0.0028
DM5AG07	DMP Basaltic andesite	0.704221	5	0.512788	3	2.93	18.6307	0.0011	15.6262	0.0010	38.5740	0.0028
DM3AG14	IPD2	0.704458	5	0.512663	4	0.48	18.6270	0.0015	15.6235	0.0013	38.5740	0.0032
DM5AG32	IPD2	0.704329	4	0.512691	3	1.04	18.6229	0.0007	15.6222	0.0006	38.5689	0.0014
DM5AG34	DMP Basaltic andesite	0.703915	5	0.512796	3	3.08	18.6117	0.0011	15.6180	0.0010	38.5382	0.0026
DMN16	Paredones Basaltic andesite	0.704096	5	0.512781	4	2.78	18.5796	0.0028	15.6026	0.0025	38.4631	0.0060
DMN30	Paredones Rhyolite	0.704374	5	0.512711	4	1.42	18.5692	0.0012	15.6086	0.0011	38.4721	0.0031

Table 3: Hf isotope data for the DMIC zircon samples.

Sample	$^{176}Hf/^{177}Hf$	1s (abs)	$^{176}Lu/^{177}Hf$	1s (abs)	$^{206}Pb/^{238}U$ age (Ma)	2s	εHf(t)	2s	TDM(2s)
DM2AG01 z1	0.282832	0.000005	0.000616	0.000006	3.83	0.01	1.8	0.4	842
DM2AG01 z2	0.282859	0.000014	0.000571	0.000006	3.83	0.01	2.7	1.0	788
DM2AG01 z5	0.282814	0.000006	0.000814	0.000008	3.85	0.08	1.1	0.5	878
DM2AG01 z6	0.282852	0.000004	0.000614	0.000006	3.83	0.01	2.5	0.3	802
DM2AG01 z8	0.282816	0.000003	0.000824	0.000008	3.83	0.05	1.2	0.2	874
DM2AG01 z10	0.282846	0.000004	0.001137	0.000011	3.81	0.03	2.3	0.3	814
DM4AG14 z1	0.282791	0.000005	0.001038	0.000010	3.67	0.24	0.3	0.4	924
DM4AG14 z2	0.282827	0.000003	0.000761	0.000008	3.72	0.06	1.6	0.2	852
DM4AG14 z3	0.282861	0.000002	0.001252	0.000013	3.72	0.02	2.8	0.2	784
DM4AG14 10-6	0.282816	0.000005	0.001002	0.000010	3.73	0.12	1.2	0.4	874
DM2AG33 z4	0.282856	0.000017	0.001608	0.000020	8.70	0.05	2.7	1.2	794
DM2AG33 z6	0.282853	0.000008	0.001064	0.000011	3.92	0.23	2.5	0.6	800
DM2AG33 z9	0.282773	0.000007	0.001275	0.000013	4.01	0.09	-0.3	0.5	959
DM2AG33 z10	0.282773	0.000010	0.000794	0.000008	4.00	0.21	-0.3	0.7	959
DMN30 z1	0.282808	0.000008	0.000567	0.000006	8.44	0.15	1.0	0.6	890
DMN30 z2	0.282811	0.000010	0.001715	0.000017	3.88	0.05	1.0	0.7	884
DMN30 z3	0.282849	0.000007	0.001473	0.000015	3.88	0.03	2.4	0.5	808
DMN30 z4	0.282790	0.000016	0.000892	0.000009	3.82	0.42	0.3	1.2	926
DM5AG32 z1	0.282801	0.000010	0.000794	0.000008	4.00	1.25	0.7	0.7	904
DM5AG32 z2	0.282862	0.000010	0.001470	0.000015	3.66	0.07	2.8	0.7	782
DM5AG32 z3	0.282819	0.000003	0.000884	0.000009	3.44	0.26	1.3	0.2	868
DM5AG32 z4	0.282824	0.000007	0.000681	0.000007	3.84	0.09	1.5	0.5	858
DM5AG32 z8	0.282832	0.000003	0.000869	0.000009	3.70	0.08	1.8	0.2	842
DM8AG44 z2	0.282836	0.000005	0.000692	0.000007	3.77	0.13	1.9	0.4	834
DM8AG44 z3	0.282847	0.000007	0.001289	0.000013	3.60	0.13	2.3	0.5	812
DM8AG44 z4	0.282832	0.000004	0.000652	0.000007	7.59	0.32	1.8	0.3	842

Table 4: Plagioclase characteristics in the Intermediate Porphyry Dikes of the Don Manuel Igneous Complex, Chile

Group	Characteristics	Occurrence
1	Reversely zoned. Cores are broad, largely unaltered An_{38-23}; Rims are broad, often sieve-textured with sharp transitions to >An_{50}; Inner rim compositions are very consistent, outer rims are normally zoned. Often contain inclusions of magnetite and apatite in the rim.	IPD Type 1, 2, 3
2	Oscillatory zoned, sometimes with high amplitude and high frequency changes in An content. Cores are largely unaltered An_{44-21}; Rims are narrow, inner rims may show an increase in An, but outer rims are normally zoned An_{51-32}; Mineral inclusions occur throughout, including apatite, magnetite and anhydrite (in two phenocrysts).	IPD Type 1, 2
3	Patchy zoning, zones commonly have rounded corners. Grains maybe fractured or broken. Cores show significant resorption An_{65-48}; Rims are mostly narrow, inner rims may show and increase in An, but outer rims are normally zoned An_{49-32}; Mineral inclusions occur throughout and include apatite, magnetite, amphibole, and biotite.	IPD Type 1, 2, 3
4	Largely unzoned, euhedral grains with cores of An_{58-51} and very narrow rims showing consistent An content An_{50-37}; Mineral inclusions are less common that in the other plagioclase types.	IPD Type 2, 3, and mafic enclave
5	Patchy zoning, zones commonly have very rounded corners. Grains are often within glomerocrysts. Cores have very high An content An_{87-66} and may show significant resorption; Rims are broad and show either normal or high frequency oscillatory zoning, An_{50-28}; Mineral inclusions occur throughout, including large apatites, magnetite and biotite.	IPD Type 2, 3, and mafic enclave

Table 5: Representative biotite compositions from the Don Manuel Igneous Complex, Chile

Sample	DM5AG13	DM5AG13	DM1AG31	DM1AG31	DM1AG23	DM1AG23	DM4AG08	DM4AG14
Biotite type	Primary biotite	Secondary biotite	Primary biotite	Secondary biotite	Primary biotite	Secondary biotite	Primary biotite	Primary biotite
Unit	IPD1	IPD1	IPD2	IPD2	IPD3	IPD3	Biotite tonalite	Biotite tonalite
Major and minor elements (wt %)								
SiO_2	37.80	38.21	37.82	39.72	37.74	38.46	38.32	37.70
TiO_2	3.08	1.74	2.38	2.74	2.21	1.99	4.09	3.79
Al_2O_3	15.41	20.19	15.38	14.33	14.52	14.94	12.72	13.45
FeO	11.99	bdl	14.81	14.27	16.36	16.19	15.94	16.98
MnO	0.07	0.07	0.04	0.06	0.22	0.20	0.22	0.09
MgO	16.11	24.86	14.47	15.63	14.24	14.30	14.12	13.57
CaO	bdl	bdl	bdl	0.01	0.02	0.00	0.00	0.00
Na_2O	0.07	0.14	0.02	0.04	0.04	0.03	0.09	0.05
K_2O	9.32	8.42	9.46	8.88	8.83	9.12	9.39	9.49
Cr2O3	0.03	0.09	0.09	0.17	0.01	0.01	bdl	0.02
F	bdl	bdl	bdl	bdl	bdl	bdl	bdl	bdl
Cl	0.14	0.13	0.13	0.11	0.21	0.14	0.20	0.22
H_2O*	3.99	4.26	3.96	4.06	3.90	3.98	3.93	3.91
Total	98.01	98.09	98.57	100.02	98.31	99.36	99.02	99.26
Formula per 22 O + 4(OH,F,Cl)								
Si	5.63	5.34	5.68	5.82	5.72	5.75	5.78	5.70
^{iv}Al	2.37	2.66	2.32	2.18	2.28	2.25	2.22	2.30
Sum_{iv}	8.00	8.00	8	8	8	8	8.00	8.00
Ti	0.35	0.18	0.27	0.30	0.25	0.22	0.46	0.43
^{vi}Al	0.34	0.66	0.40	0.30	0.31	0.38	0.04	0.10
Cr	0.00	0.01	0.01	0.02	0.00	0.00	0.00	0.00
Fe	1.49	0.00	1.86	1.75	2.07	2.02	2.01	2.15
Mg	3.58	5.18	3.24	3.41	3.21	3.19	3.17	3.06
Mn	0.01	0.01	0.01	0.01	0.03	0.03	0.03	0.01
Sum_{vi}	5.77	6.04	5.78	5.79	5.87	5.84	5.71	5.75
Ca	0.00	0.00	0.00	0.00	0.00	0.00	0.00	0.00
Na	0.02	0.04	0.01	0.01	0.01	0.01	0.03	0.02
K	1.77	1.50	1.81	1.66	1.71	1.74	1.81	1.83
Sum_{xii}	1.79	1.54	1.82	1.67	1.72	1.75	1.83	1.85
Sum cation	15.56	15.58	15.60	15.46	15.59	15.59	15.54	15.59
xMg	0.71	1.00	0.64	0.66	0.61	0.61	0.61	0.59

Table 6: Representative compositions of clinopyroxene from the Paredones basaltic andesite

Sample	DMN16	DMN16	DMN16	DMN16
Analysis location	Phenocryst core	Phenocryst rim	Groundmass	Groundmass
SiO_2	51.6366	50.3668	52.1113	50.4436
TiO_2	0.5195	0.7098	0.5218	0.6971
Al_2O_3	2.8518	3.5885	1.8345	3.7154
Cr_2O_3	bdl	bdl	bdl	bdl
FeO	8.6589	9.0943	10.7681	9.927
MnO	0.2661	0.2838	0.4511	0.3317
MgO	15.3168	14.4847	16.5517	14.2872
CaO	20.2578	20.4337	16.9443	19.932
Na_2O	0.3934	0.3074	0.2206	0.4226
Total	99.9016	99.269	99.4166	99.7587
xMg	0.75	0.73	0.72	0.71

Table 7: Representative amphibole compositions from the Don Manuel Igneous Complex, Chile

Sample	DM6AG11	DM6AG11	DM6AG21	DM6AG21	DM1AG23	DM8AG53	DM3AG23	DM3AG23	DM7AG18
Analysis location	Rim	Core	Core	Rim	Rim	Rim	Core	Rim	Core
Host	IPD2	IPD2	IPD3	IPD3	IPD3	IPD3	Mafic Enclave	Mafic Enclave	Gabbroic xenolith
Major and minor elements (wt %)									
SiO_2	46.95	48.03	43.27	44.64	43.17	43.86	48.17	46.16	40.72
TiO_2	1.18	1.67	2.31	2.04	1.79	1.42	1.27	1.87	1.69
Al_2O_3	7.69	8.43	12.55	10.36	11.44	10.41	6.84	8.96	13.80
Cr_2O_3	bdl	bdl	0.54	bdl	bdl	bdl	0.02	0.00	bdl
MnO	0.34	0.19	0.09	0.34	0.77	0.42	0.32	0.23	0.48
FeO	13.83	9.77	8.63	12.61	15.72	16.65	12.33	11.93	14.87
MgO	14.09	16.61	15.86	14.36	11.27	11.36	15.20	14.65	11.15
CaO	11.52	11.52	11.11	10.64	11.16	11.46	11.17	11.22	11.53
Na_2O	1.67	1.39	2.62	1.99	1.68	1.76	1.39	1.86	2.02
K_2O	0.44	0.48	0.43	0.41	0.39	0.42	0.40	0.40	0.45
F	bdl	bdl	bdl	bdl	bdl	bdl	bdl	bdl	bdl
Cl	0.08	0.06	0.02	0.07	0.06	0.08	0.09	0.05	0.04
Total	97.80	98.13	97.44	97.45	97.46	97.84	97.21	97.31	96.76
Ideal site assignments									
Si	6.85	6.82	6.24	6.51	6.39	6.49	6.99	6.73	6.07
^{iv}Al	1.15	1.18	1.76	1.49	1.61	1.51	1.01	1.27	1.93
^{vi}Al	0.17	0.23	0.38	0.29	0.38	0.31	0.16	0.27	0.49
Ti	0.13	0.18	0.25	0.22	0.20	0.16	0.14	0.21	0.19
Cr	0.00	0.00	0.06	0.00	0.00	0.00	0.00	0.00	0.00
Fe^{3+}	0.38	0.39	0.27	0.37	0.52	0.50	0.41	0.23	0.56
Fe^{2+}	1.31	0.77	0.78	1.17	1.42	1.56	1.09	1.22	1.30
Mg	3.07	3.52	3.41	3.12	2.49	2.51	3.29	3.18	2.48
Mn	0.04	0.02	0.01	0.04	0.10	0.05	0.04	0.03	0.06
Ca	1.80	1.75	1.72	1.66	1.77	1.82	1.74	1.75	1.84
Na	0.47	0.38	0.73	0.56	0.48	0.50	0.39	0.53	0.58
K	0.08	0.09	0.08	0.08	0.07	0.08	0.07	0.07	0.09
F	0.00	0.00	0.00	0.00	0.00	0.00	0.00	0.00	0.00
Cl	0.02	0.01	0.00	0.02	0.02	0.02	0.02	0.01	0.01
OH*	1.98	1.99	2.00	1.98	1.98	1.98	1.98	1.99	1.99
Na_b	0.11	0.14	0.13	0.13	0.12	0.10	0.15	0.12	0.09
$(Na+K)_a$	0.45	0.33	0.68	0.51	0.43	0.49	0.32	0.48	0.59
xMg	0.89	0.90	0.93	0.90	0.83	0.83	0.89	0.93	0.82
Al_{TOT}	1.32	1.41	2.13	1.78	2.00	1.82	1.17	1.54	2.42

Table 7 Representative amphibole compositions from the Don Manuel Igneous Complex, Chile

Sample	DM7AG18	DM4AG28	DM4AG28	DMN16	DMN16	DM4AG16	DM4AG08	DM4AG27	DM4AG14
Analysis location	Rim	Rim	Core	Rim	Core	Rim	Rim	Core	Rim
Host	Gabbroic xenolith	DMP Basaltic Andesite	DMP Basaltic Andesite	Paredones Basaltic Andesite	Paredones Basaltic Andesite	Bioitite Tonalite	Bioitite Tonalite	Biotite Tonalite	Bioitite Tonalite
Major and minor elements (wt %)									
SiO_2	43.91	41.85	42.31	41.69	41.65	51.43	50.74	45.54	50.84
TiO_2	1.94	2.65	2.85	3.05	3.21	0.72	1.05	2.26	0.71
Al_2O_3	10.11	12.83	12.58	12.83	12.93	4.27	4.48	8.54	4.59
Cr_2O_3	bdl	0.14	0.07	ND	ND	bdl	bdl	bdl	0.03
MnO	0.42	0.11	0.10	0.17	0.19	0.30	11.45	0.20	11.21
FeO	15.16	9.19	10.00	11.81	11.99	10.57	16.45	12.74	16.57
MgO	12.29	15.59	15.07	14.13	14.09	17.14	11.50	14.15	11.71
CaO	11.03	11.67	11.54	11.31	11.40	11.84	0.49	11.07	0.31
Na_2O	1.59	2.57	2.57	2.67	2.75	0.68	1.05	2.09	0.85
K_2O	0.50	0.42	0.42	0.41	0.43	0.32	0.41	0.71	0.33
F	bdl	bdl	bdl	bdl	bdl	bdl	bdl	bdl	0.01
Cl	0.10	0.04	0.04	0.02	0.02	0.11	0.13	0.13	0.11
Total	97.06	97.06	97.57	98.09	98.67	97.36	97.75	97.43	97.27
Ideal site assignments									
Si	6.50	6.08	6.14	6.06	6.03	7.35	7.61	6.69	7.64
^{iv}Al	1.50	1.92	1.86	1.94	1.97	0.65	0.39	1.31	0.36
^{vi}Al	0.26	0.28	0.29	0.26	0.24	0.07	0.40	0.17	0.45
Ti	0.22	0.29	0.31	0.33	0.35	0.08	0.12	0.25	0.08
Cr	0.00	0.02	0.01	0.00	0.00	0.00	0.00	0.00	0.00
Fe^{3+}	0.53	0.44	0.36	0.44	0.42	0.37	0.00	0.20	0.00
Fe^{2+}	1.35	0.67	0.86	1.00	1.04	0.89	2.06	1.37	2.08
Mg	2.71	3.38	3.26	3.06	3.04	3.65	2.57	3.10	2.62
Mn	0.05	0.01	0.01	0.02	0.02	0.04	1.46	0.03	1.43
Ca	1.75	1.82	1.80	1.76	1.77	1.81	0.08	1.74	0.05
Na	0.46	0.73	0.72	0.75	0.77	0.19	0.31	0.60	0.25
K	0.09	0.08	0.08	0.08	0.08	0.06	0.08	0.13	0.06
F	0.00	0.00	0.00	0.00	0.00	0.00	0.00	0.00	0.00
Cl	0.03	0.01	0.01	0.01	0.01	0.03	0.03	0.03	0.03
OH*	1.97	1.99	1.99	2.00	1.99	1.97	1.97	1.97	1.97
Na_b	0.13	0.10	0.11	0.13	0.12	0.09	0.31	0.15	0.25
$(Na+K)_a$	0.42	0.71	0.69	0.70	0.73	0.15	0.08	0.58	0.06
xMg	0.84	0.88	0.90	0.88	0.88	0.91	1.00	0.94	1.00
Al_{TOT}	1.76	2.20	2.15	2.20	2.21	0.72	0.79	1.48	0.81

Table 8. Representative apatite compositions from the Don Manuel Igneous Complex, Chile

Sample	DM4AG27	DM4AG27	DM4AG27	DM5AG13	DM5AG13	DM5AG13	DM5AG36	DM5AG36	DM5AG07
Analysis location	Pl incl.	Bt incl.	MP	Bt incl.	Pl incl.	MP	MP	MP	MP
Host	Biotite Tonalite	Biotite Tonalite	Biotite Tonalite	IPD1	IPD1	IPD1	DMP Basaltic Andesite	DMP Basaltic Andesite	DMP Basaltic Andesite
SiO_2	0.25	0.16	0.16	0.14	0.11	0.13	0.12	0.11	0.13
La_2O_3	0.14	0.18	bdl	0.09	bdl	bdl	bdl	bdl	bdl
Ce_2O_3	0.26	0.42	0.21	0.18	0.16	0.24	0.10	0.19	0.10
Nd_2O_3	bdl	0.21	0.13	0.14	0.10	0.12	bdl	bdl	bdl
Y_2O_3	bdl	0.09	0.05	bdl	bdl	0.07	0.06	0.07	bdl
FeO	bdl	0.33	0.18	0.28	0.13	0.27	0.18	0.13	0.33
MnO	0.06	0.05	0.04	0.15	0.17	0.08	0.19	0.20	0.17
CaO	53.64	53.52	54.01	54.44	53.78	54.13	53.83	54.09	54.36
Na_2O	0.18	0.29	bdl	0.12	0.11	0.14	bdl	bdl	bdl
P_2O_5	40.44	40.49	41.08	42.06	40.99	41.04	40.63	40.56	40.40
SO_3	0.47	0.35	0.07	0.23	0.21	0.23	0.13	0.05	0.02
Cl	1.23	1.05	0.93	1.66	1.64	1.22	1.74	1.91	1.22
F	1.65	1.63	1.76	1.53	1.51	1.63	1.27	1.07	1.62
Total	98.31	98.77	98.63	101.03	98.91	99.30	98.24	98.37	98.35
O=F,Cl	0.97	0.92	0.95	1.02	1.01	0.96	0.93	0.88	0.96
Total	97.34	97.85	97.68	100.01	97.91	98.33	97.31	97.49	97.39

bdl = below detection limit

Pl = plagioclase; Bt = biotite; Am = amphibole; incl. = inclusion; MP = microphenocryst;

Table 8. Representative apatite compositions from the Don Manuel Igneous Complex, Chile

Sample	DM5AG07	DM6AG21	DM6AG21	DM1AG23	DMN30	DM6AG05	DM6AG05	DM6AG11	DM6AG11
Analysis location	MP	MP	MP	Am incl.	Pl incl.	MP	MP	MP	MP
Host	DMP Basaltic Andesite	IPD3	IPD3	IPD3	Rhyolite	Quartz Monzonite	Quartz Monzonite	IPD2	IPD2
SiO_2	0.12	0.10	0.08	0.18	bdl	bdl	bdl	0.12	bdl
La_2O_3	bdl	bdl	0.11	bdl	0.10	0.11	bdl	bdl	0.09
Ce2O3	0.16	0.24	0.25	bdl	0.26	0.24	0.12	0.06	0.19
Nd_2O_3	0.09	0.12	bdl	bdl	0.22	0.11	0.06	0.07	0.09
Y_2O_3	0.08	bdl	bdl	0.17	bdl	bdl	bdl	bdl	bdl
FeO	0.23	0.19	0.17	0.49	0.86	0.22	0.16	0.08	0.19
MnO	0.22	0.13	0.12	0.20	1.60	0.38	0.36	0.02	0.06
CaO	53.69	54.58	54.29	53.80	52.62	53.25	54.17	54.37	54.01
Na_2O	0.10	0.16	0.09	bdl	0.23	0.14	0.12	bdl	0.18
P_2O_5	40.58	40.12	41.57	40.65	42.01	41.74	41.84	41.22	41.67
SO_3	0.12	0.31	0.23	0.27	0.32	0.12	0.15	0.08	0.43
Cl	1.83	1.12	1.09	1.53	1.13	0.99	0.98	0.71	1.03
F	1.10	1.80	1.61	1.40	2.69	2.47	2.72	2.38	1.97
Total	98.33	98.87	99.61	98.69	99.07	98.70	100.02	98.76	99.35
O=F,Cl	0.88	1.01	0.92	0.94	1.39	1.26	1.37	1.16	1.06
Total	97.46	97.86	98.69	97.75	97.68	97.44	98.65	97.60	98.29

bdl = below detection limit

Pl = plagioclase; Bt = biotite; Am = amphibole; incl. = inclusion; MP = microphenocryst;

Table 9. Hornblende-plagioclase temperatures for DMIC units.

Sample	Unit	Temperature Range (˚C)*	Mean Temperature and SD (˚C)
DMN16	Paredones basaltic andesite	950-969	957 ± 6
DM4AG28	Basaltic Andesite (DMP)	894-916	905 ± 8
DM5AG34	Basaltic Andesite (DMP)	652-713	684 ± 26
DM7AG18	Gabbroic cumulate	759-889	815 ± 70
DM6AG11	IPD2	712-791	745 ± 30
DM1AG23	IPD3	706-773	773 ± 33
DM6AG21	IPD3	790-849	824 ± 17
DM8AG53	IPD3	799-849	821 ± 17
DM3AG23	Mafic Enclave (host = IPD)	675-839	755 ± 54
DM4AG08	Porphyritic Biotite Tonalite	595-769	696 ± 71
DM4AG14	Porphyritic Biotite Tonalite	631-682	658 ± 17
DM4AG27	Porphyritic Biotite Tonalite	544-683	601 ± 32
DM4AG16	Equigranular Biotite Tonalite	613-706	670 ± 24

*Based on the thermometer of Holland & Blundy (1994).